

UC Berkeley

UC Berkeley Electronic Theses and Dissertations

Title

Development of Self-Consolidating Hybrid Fiber Reinforced Concrete and Assessment of Its Durability Performance

Permalink

<https://escholarship.org/uc/item/5bx2m6p9>

Author

Jen, Gabriel

Publication Date

2014

Peer reviewed|Thesis/dissertation

Development of Self-Consolidating Hybrid Fiber Reinforced Concrete and Assessment of Its
Durability Performance

by

Gabriel Gregory Tock Jen

A dissertation submitted in partial satisfaction of the

requirements for the degree of

Doctor of Philosophy

in

Engineering – Civil and Environmental Engineering

in the

Graduate Division

of the

University of California, Berkeley

Committee in charge:

Professor Claudia P. Ostertag, Chair

Professor Paulo J. M. Monteiro

Professor Thomas M. Devine

Fall 2014

Development of Self-Consolidating Hybrid Fiber Reinforced Concrete and Assessment of Its
Durability Performance

Copyright © 2014

by

Gabriel Gregory Tock Jen

All rights reserved

Abstract

Development of Self-Consolidating Hybrid Fiber Reinforced Concrete and Assessment of Its Durability Performance

by

Gabriel Gregory Tock Jen

Doctor of Philosophy in Engineering – Civil and Environmental Engineering

University of California, Berkeley

Professor Claudia P. Ostertag, Chair

Conventional concrete used for construction has neither the inherent ductility nor durability to meet the requirements of modern infrastructure construction. With ageing highway and bridge infrastructure requiring a significant expenditure of capital, it is prudent to explore utilization of so-called high performance materials that have the potential to outperform and outlast their conventional counterparts. This research program is built around the concept of creating a sustainable material that exceeds the performance of conventional concrete through a characteristic enhanced cracking resistance achieved by the introduction of discrete fiber reinforcement combined with an optimized level of workability.

In an effort to meet the existing demand for high performance materials suitable for modern construction practice, self-consolidating features have been developed for a preexisting high performance hybrid fiber reinforced concrete. A parametric study was employed to maximize the fresh state performance benefits of chemical and supplementary cementitious material additives in conjunction with optimization of the fiber reinforcement to meet the flow criteria of self-consolidating type concrete. The resulting composite, Self-Consolidating Hybrid Fiber Reinforced Concrete (SC-HyFRC), is tested under compression, tension and flexure loading independently and in combination with conventional steel reinforcement to illustrate the mechanical performance gains that can be achieved with such composites. The performance enhancements gained in each manner of loading are then combined in the material's application to a structural element that must be designed to undergo a substantial inelastic (cracked) response.

The intrinsic durability of the SC-HyFRC material is tested against two environmental deterioration mechanisms which plague modern concrete. Due to the enhanced crack resistance present in SC-HyFRC, chloride-induced steel reinforcement corrosion is mitigated during both the initiation and the propagation phases. This mitigation is qualitatively and quantifiably measured by suppression of observable cracking and direct electrochemical measurements of the reinforcing steel surface. Similarly, the cracking resistance feature of SC-HyFRC and similar fiber reinforced cementitious composites is judged for mitigation capacity of alkali-silica reaction. The magnitude of internal cracking accompanying the swelling-induced expansion is measured by relative changes in structurally relevant concrete mechanical properties, compressive strength and elastic modulus, with fiber reinforced restraint of expansion observed

to correlate well with mechanical property retention. As reinforcement corrosion and alkali-silica reaction are but two of many deterioration mechanisms that induce damage by way of internal expansion, the positive outcomes of SC-HyFRC testing are expected to be transferable to concrete durability in a holistic sense.

The potential benefit of constructing critical infrastructure elements with such high performance materials is a two-fold gain in overall structural life cycle assessment, being better equipped to deal with multiple facets of loading placed on modern structures. This and similar research of SC-HyFRC and other such materials will hopefully validate the upfront costs necessary to build with materials that can generate outsized long term fiscal savings.

In memory of R.

Table of Contents

1	Introduction	1
1.1	Organization of the Dissertation	5
2	SC-HyFRC Development and Properties	7
2.1	Introduction	7
2.2	Background	8
2.3	Materials and Test Methods	10
2.4	Parametric Development	13
2.4.1	Admixture Dosage	14
2.4.2	Binder Content	14
2.4.3	Aggregate Content	15
2.4.4	Fiber Content	15
2.4.5	Self-Consolidating Hybrid Fiber Reinforced Concrete	18
2.5	Composite Performance	20
2.5.1	Internal Confinement	20
2.5.2	Flexural Enhancement	24
2.5.3	Tension Stiffening	25
2.6	Extension to Bridge Column Testing	29
2.7	Conclusions	31
3	Corrosion Damage Resistance	33
3.1	Introduction	33
3.2	Background	35
3.3	Test Methods	38
3.3.1	Electrochemical Test Methods	38
3.3.2	Corrosion Damage Testing Methods	42
3.4	Materials	42
3.5	Corrosion Testing Results	44
3.5.1	Corrosion Initiation Testing Results	44
3.5.2	Corrosion Propagation Testing Results	55
3.6	Corrosion Testing Discussion	59
3.6.1	Corrosion Initiation Testing Discussion	59
3.6.2	Corrosion Propagation Testing Discussion	64
3.7	Conclusions	68
4	Alkali-Silica Reaction Damage Resistance	69

4.1	Introduction	69
4.2	Background	70
4.3	Test Methods	72
4.3.1	ASR Expansion Testing Methods	72
4.3.2	ASR Mechanical Property Testing Methods	74
4.4	Materials	74
4.4.1	Reactive Aggregate Materials	74
4.4.2	Cementitious Materials	78
4.5	Test Procedures	78
4.5.1	AMBT Testing Procedure	78
4.5.2	CPT Testing Procedure	80
4.6	Results	83
4.6.1	AMBT Results	83
4.6.2	CPT Results	89
4.7	Discussion	95
4.7.1	AMBT Discussion	95
4.7.2	CPT Discussion	98
4.8	Conclusions	101
5	Concluding Remarks	103
	References	106
	Appendix A	112
	Appendix B	113
	Appendix C	121

List of Figures

Figure 2-1 On-Site Mixers and Capacities at UC Berkeley Concrete Laboratory	11
Figure 2-2 Reinforcing Layouts for Passing Ability Assessment, mm	12
Figure 2-3 4-Point Bending Response with and without 0.2 Volume Percent 60 mm Steel Fiber	17
Figure 2-4 Concrete “Flow” Characteristics at Subsequent Stages of Mixture Development, with Decreasing Segregation Tendency Shown from Left to Right	17
Figure 2-5 Slump Flow Behavior of SC-HyFRC; a) Influence of Parameters, b) Slump Flow Test	18
Figure 2-6 Mechanical Properties of SC-HyFRC; a) Compression, b) Direct Tension, c) 4-Point Bending	19
Figure 2-7 a) Confinement Cylinder Specimens with Variable Spiral Spacing, mm, b) Testing Setup with Compressometer in Place	21
Figure 2-8 Damage Progression of 0.5 Percent Transversely Reinforced Concrete (top row) and SC-HyFRC (bottom row); at a) Peak Load, b) 3 Percent Strain, c) 5 Percent Strain	22
Figure 2-9 Comparison of Confinement Effects for SCC and SC-HyFRC Type Mixes; a) Compression Response, b) Residual Capacity Comparison	23
Figure 2-10 Comparison of Transverse Reinforcement Strain at 4 Discrete Points Along the Mid Height of 0.5 Percent Transversely Reinforced, a) SCC and b) SC-HyFRC, Cylinders	24
Figure 2-11 Composite Flexural Response of Reinforced SC-HyFRC Beams	25
Figure 2-12 Tension Stiffening Specimens with Distributed Strain Gages, mm	26
Figure 2-13 Tension Stiffening Response of SC-HyFRC Material; a) Initial Cracking Response, b) Yield and Strain Hardening Response, with Points Marked for Further Strain Distribution Analysis	27
Figure 2-14 Strain Localization Effects as Measured by Strain Gages in Tension Composite of SC-HyFRC	27
Figure 2-15 Strain Localization Effects as Measured by Strain Gages in Tension Samples	28
Figure 2-16 SC-HyFRC Column Detail, mm	30
Figure 2-17 Column Base Damage at; a) 3.6 Percent Drift, b) 6.0 percent drift	31
Figure 3-1 Schematic of Steel Corrosion Sequence in Concrete (after Tuutti 1982)	34
Figure 3-2 Modified Crack Resistant Damage Schematic of Corrosion Sequence	34
Figure 3-3 Typical Galvanic Corrosion Test Performance	39
Figure 3-4 Typical Corrosion Potential Test Performance	41
Figure 3-5 Typical Polarization Resistance Test Performance	41
Figure 3-6 Typical Tafel Scan Test Performance	41
Figure 3-7 NT Build 492 Rapid Testing of Chloride Migration	44
Figure 3-8 Reinforced Concrete Beam 4-Point Bending Test Dimensions, mm (inches)	45
Figure 3-9 Cyclic Load Response of Reinforced Concrete Beams Prior to Corrosion Initiation	46
Figure 3-10 Reinforced Concrete Beam Electrochemical Test Setup, mm (inches)	47
Figure 3-11 Corrosion Current Density of SCC Beams (i_{corr} – microcell, i_g – galvanic)	48
Figure 3-12 Corrosion Current Density of SC-HyFRC Beams (i_{corr} – microcell, i_g – galvanic)	49
Figure 3-13 Observations of Splitting Crack Damage in Various SCC Beams	50
Figure 3-14 Prior to Corrosion (a,c) and Final (b,d) Tensile Face Comparison of Preloaded SCC (a,b) and SC-HyFRC (c,d) Beam Samples, mm	52

Figure 3-15 Residual Flexural Capacity Testing of Corroded SC-HyFRC Beams Relative to Original 28-Day Flexural Response of SCC (dashed blue) and SC-HyFRC (solid black) Beams	52
Figure 3-16 Corrosion Current Density of Flexure-Induced Precracked SC-HyFRC Beam	53
Figure 3-17 Surface Imaging of the Cracked SC-HyFRC Beam Prior to and After Corrosion Damage, mm	54
Figure 3-18 Residual Flexural Capacity of Corroded Cracked SC-HyFRC Beam Relative to Original and Corrosion-Damaged Unloaded/Preloaded SC-HyFRC Beams	55
Figure 3-19 Lollipop Sample Dimensions, mm (inches)	56
Figure 3-20 Lollipop Sample Electrochemical Test Setup	57
Figure 3-21 Conventional Corrosion Propagation Test Response of SCC and SC-HyFRC Mixes	57
Figure 3-22 Accelerated Corrosion Propagation Test Response of SCC and SC-HyFRC Mixes	58
Figure 3-23 Color Indicator Stained Cores of Concrete; a) AgCl Depth in Unloaded SC-HyFRC Beams, b) AgCl depth in Preloaded SC-HyFRC Beams, c) Carbonation Depths (Consistent in all SCC and SC-HyFRC Beams), Approximate Depths of Reinforcing Bars Shown for Reference	60
Figure 3-24 ASTM C1152 Chloride Concentration Profile of SCC and SC-HyFRC Beam Cores, with ACI 222 (2001) Limit of 0.2 Percent and Reinforcing Bar Locations Shown for Reference	61
Figure 3-25 Reinforcing Bar Surfaces of Preloaded a) SCC and b) SC-HyFRC #3 Reinforcing Bars Following Acid Cleaning, mm	63
Figure 3-26 Crack Development in Conventional Corrosion Propagation Testing at 130 Weeks	64
Figure 3-27 Crack Development in Accelerated Corrosion Propagation Testing, 1 Day of Current	64
Figure 3-28 Crack Development in Accelerated Corrosion Propagation Testing, 2 Days of Current	65
Figure 3-29 Proposed Mechanism of Corrosion Control through Fiber Crack Control of the Propagation Phase (after Blunt 2008)	66
Figure 4-1 Fine Aggregate Gradation with ASTM C33 Limits Shown as Dashed Lines	76
Figure 4-2 Photomicrographs of #30 Aggregate Particles, Plane Polarized (top row) and Cross Polarized Light (bottom row)	77
Figure 4-3 Mortar Bar Test Specimen Dimensions, mm (inches)	79
Figure 4-4 Influence of Fine to Coarse Aggregate Content Ratio and Curing Temperature on the Load Deflection Behavior of Hybrid Fiber Reinforced Concrete	81
Figure 4-5 Concrete Prism Test Specimen Dimensions, mm (inches)	82
Figure 4-6 ASTM C1260 Expansion Plots of Wright Aggregate (gradations conforming to standard, F.M.-2.9 and as-received, F.M.-2.6)	84
Figure 4-7 ASTM C1260 Expansion Plots of Spratt Aggregate (gradation conforming to standard), with 2 and 4 Day H ₂ O Curing Steps	85
Figure 4-8 ASTM C1260 Expansion Plots of Vulcan Aggregate (gradation conforming to as-received)	85
Figure 4-9 ASTM C1260 Expansion Plots of Wright Aggregate, High Volume Fly Ash	86
Figure 4-10 Flexural Response of Wright Aggregate ASR Mortar Bars	87
Figure 4-11 Flexural Response of Wright Aggregate ASR Mortar Bars, 0.2 Percent PVA Microfiber Reinforcement	87
Figure 4-12 Flexural Response of Wright Aggregate ASR Mortar Bars, 1.0 Percent PVA Microfiber Reinforcement	87

Figure 4-13 Flexural Response of Wright Aggregate, High Volume Fly Ash ASR Mortar Bars (from Hay 2014)	88
Figure 4-14 Flexural Response of Wright Aggregate, High Volume Fly Ash ASR Mortar Bars, 0.2 Percent PVA Microfiber Reinforcement (from Hay 2014)	89
Figure 4-15 ASTM C1293 Expansion Plot of HyFRC Containing Wright Fine Aggregate	90
Figure 4-16 ASTM C1293 Expansion Plot of FRC Containing Wright Fine Aggregate	91
Figure 4-17 ASR Distress Inconsistencies Between Expansion Prisms (left) and Flexural Test Prisms (right) Having Wright Fine Aggregate, mm	91
Figure 4-18 Load Deflection Response of ASR Damage FRC Containing Wright Fine Aggregate	92
Figure 4-19 ASTM C1293 Expansion Plot of SC-HyFRC Containing Wright Fine Aggregate	93
Figure 4-20 ASTM C1293 Expansion Plot of FRC Containing Spratt Coarse Aggregate	94
Figure 4-21 Internal Microstructure of; a) Wright Mortar, b) Wright Microfiber Reinforced Mortar, c) Vulcan Mortar, d) Vulcan Microfiber Reinforced Mortar. Spots for Later EDX Analysis Highlighted	96
Figure 4-22 Internal Microstructure of Spratt Mortar (a,b) and Spratt Microfiber Reinforced Mortar (c,d), At 25X Magnification (a,c) and 100X Magnification (b,d)	98
Figure 4-23 Comparison of a) Compression Strength and b) Elastic Modulus Development as a Function of ASR Expansion Level (with Multon et al. (2005) Results for Reference), Hollow Markers Representing 6 Month Data and Full Markers representing 1 Year Data	101
Figure 5-1 Projected Influence of Crack Resistance on the Service Life Expectancy as Related to Durability Mechanisms (top), Projected Influence of Earthquake Events Upon the Service Life Expectancy as Related to Durability Mechanisms (bottom)	104

List of Tables

Table 1-1 Comparison of Reaction Product Formation Necessary for Crack Development and Growth in Hardening and Non-Hardening Composites	4
Table 2-1 Summary of Previous Selected Work on Combined SCC/FRC	9
Table 2-2 Fiber Properties	10
Table 2-3 SCC Parameters of HyFRC	13
Table 2-4 Concrete Mix Compositions (kg/m ³)	18
Table 2-5 Drift Ratio Cycling Targets of SC-HyFRC Column	30
Table 3-1 Rebar Mill Certificates; Alloying Composition (%) and Strength (MPa)	42
Table 3-2 Fly Ash Influence upon Strength of Concrete Corrosion Mixes (MPa)	43
Table 3-3 Concrete Mix Chloride Non-Steady-State Migration Coefficients ($\times 10^{-12}$ m ² /s)	44
Table 3-4 Cracking Behavior of Cyclically Loaded Reinforced Beam Samples	46
Table 3-5 Final Corrosion Measurements of SCC and SC-HyFRC Corrosion Beams	50
Table 3-6 Final Electrochemical Measurements of Flexure-Induced Cracked SC-HyFRC Beam	54
Table 3-7 Reinforcing Bar Mass Loss of SCC and SC-HyFRC Beams, g	63
Table 3-8 Reinforcing Bar Mass Loss of SCC and SC-HyFRC Conventional Propagation Cylinders, g	66
Table 3-9 Reinforcing Bar Mass Loss of SCC and SC-HyFRC Accelerated Propagation Cylinders, g	66
Table 4-1 ASR Associated Minerals (ranked from most to least deleterious, Thomas et al. 2013)	69
Table 4-2 Petrographic Classification of Reactive Aggregates	75
Table 4-3 Aggregate Properties Determined by ASTM C127/128 and Fineness Modulus	75
Table 4-4 Aggregate Mass Percent Reactive by Particle Size	77
Table 4-5 Reactive Mass (Percent of Total Mass) Distribution by Particle Size in Natural Gradation	77
Table 4-6 Chemical Composition of Cementitious Components	78
Table 4-7 AMBT Test Parameter Grid ¹	80
Table 4-8 Alkali and Wright Aggregate Component Content in Fine Aggregate CPT Tests (kg/yd ³)	82
Table 4-9 CPT Test Parameter Grid ¹	83
Table 4-10 Spratt Aggregate Mortar Cube Strength Evolution, (MPa)	84
Table 4-11 Reactivity Ranking of Reference Mortars by Aggregate Type/Fineness Modulus	86
Table 4-12 Mechanical Properties of ASR Damaged HyFRC Containing Wright Fine Aggregate (Percent Change from 28 Day Result)	90
Table 4-13 Mechanical Properties of ASR Damaged FRC Containing Wright Fine Aggregate (Percent Change from 28 Day Result)	92
Table 4-14 Mechanical Properties of ASR Damaged SC-HyFRC Containing Wright Fine Aggregate (Percent Change from 28 Day Result)	93
Table 4-15 Mechanical Properties of ASR Damaged FRC Containing Spratt Coarse Aggregate (Percent Change from 28 Day Result)	94
Table 4-16 Sodium, Silica, Calcium Molar Ratio from EDX Spot Analysis of Crack Deposits	96
Table 4-17 Calcium, Silica, Sodium Content from EDX Spot Analysis of Fiber Interfacial Product	98

Acknowledgements

To my advisor, Professor Claudia P. Ostertag, I am forever grateful for giving me the opportunity to pursue an advanced degree. Through the myriad of projects I have been involved in, I hope that the results herein and others not included may prove helpful in our eventual goal of bringing fiber reinforced concrete to the fore of the construction industry.

To my dissertation committee members, Professors Paulo Monteiro and Thomas Devine, I am thankful for the insights and constructive advice you were able to offer me in shaping the direction and presentation of my manuscript.

To my parents and sisters who supported me immeasurably through the process I am extremely grateful.

To Dr. Lev Stepanov who was my concrete mentor and provided me with the tools to do as much concrete mixing as I could handle, I can honestly say that my work product would be a shadow of itself without your help.

To Dr. Joshua Blunt, Dr. William Trono, Dr. Seyoon Yoon, Mr. Rotana Hay, Mr. Wilson Nguyen and my other fellow Civil Engineering-Materials students from the first floor, past and present, who provided me with many quality discussions and important insights into things unknown to me, I can only hope that I was a fraction as helpful to you as you have been to me.

To Mr. Greg Rulifson, Ms. Ekaterina Kostyukova and Mr. Ryan Sanders who went above and beyond the expectations I had of undergraduate research assistants I would like to thank each of you and acknowledge the critical contributions you have made to the material of Chapters 2, 3 and 4 respectively.

To Dr. Catherine Whyte and Dr. Tracy Becker, my study group, with whom I spent countless nights finishing homework assignments and trying to learn how to maximize my crib sheet space for final exams I would like to thank you for your help and the motivation you provided me to finish, even if it did take me the longest.

To Ms. Coralie Chan, Mr. Daniel Spickard and all of the friends who stuck by me during the long graduate school process and provided encouragement and support I would like to say thank you.

This work was supported in part by Federal Highway Administration Grant #DTFH61-09-R-00017 and material contributions by the Ontario Ministry of Transportation.

1 Introduction

To meet the demands of the global construction appetite, utilization of concrete as a building material is at record levels. Estimates of 2013 place concrete production at 19 billion tons with an estimated 3.7 billion tons of cement consumed and with much of the balance constituted of aggregates (van Oss 2013). Though its usage on a mass per capita basis is higher than any other construction material, concrete production of this scale is not without its own set of financial and environmental ramifications. On the financial side, the cost of large scale infrastructure projects has ballooned and made structural life expectancy a key mark in offsetting the capital expenditures embodied in architectural form. With such high upfront costs, existing transportation budgets do not have the capacity to provide regular replacement, meaning concrete structures must meet their intended service lifespan. The environmental cost of large scale concrete production is likewise taxing on the environment with cement production commonly thought to account for between 5 and 8 percent of global CO₂ production. Less commonly discussed but equally impactful, the rate of consumption of aggregates for concrete production has diminished the inventory of quarries supplying suitable, high quality aggregates. This limitation has been expressed as a financial burden on the concrete industry as aggregate local availability has decreased and required costly transportation from more distant locales. At the crossing of these financial and environmental issues, durability and sustainability have become a new metric upon which concrete is judged. Together they describe a desire for an enhanced concrete product that combats financial and environmental expenditures with a longevity increase, reducing the need for additional concrete consumption in current and future years.

In a setting isolated from the environment or loading the longevity of concrete is near infinite, yet by its mere functionality concrete infrastructure must be exposed to the environment and to loading. As part of their service capacities, concrete elements are designed to carry load through uniaxial compression, bending and shear with uniaxial tension being universally recognized as a material weakness and avoided. However, as structural loading can be quite diverse (dead load, live load, wind load, seismic load, etc.) concrete structures invariably have to deal with some form of tension loading. In meeting this load demand, modern construction owes much to the development of reinforced concrete in the nineteenth century when iron reinforcement was first utilized to fabricate a composite material having gained tensile capacity. At the structural scale, embedded reinforcement (now principally composed of steel) allows concrete to withstand a more diverse distribution of loads while providing a degree of ductility not typically associated with the intrinsic quasi-brittle nature of concrete.

At this point a discussion of the implied meaning and usage of the terms ductile and durable is warranted. For the entirety of this research program, “ductility” is a descriptor used synonymously with displacement capacity without succumbing to load capacity failure. Ductility is vital for so-called performance based design in which the life-safety quality of the structure is paramount and collapse prevention is a primary metric. Therefore, it is important to realize that a ductile structure is not necessarily a sustainable structure in the sense that prevention of collapse can still lead to demolition and replacement. Comparatively, “durability” is a descriptor used synonymously with damage resistance primarily with environmental attack implications. Durability is vital for structure longevity in the sense that it describes the intrinsic resistance of the structure to resist deterioration caused by the environment into which it is placed. In this

sense, there is a strong correlation between durability and sustainability in so far as a durable structure will survive without needed replacement for its prescribed lifespan.

In this context, conventional reinforcement comprised of low carbon steel reinforcing bars, ties, and hoops provide ductility to concrete but have only limited influence on increasing the durability of concrete. This difference is brought about because ductility is gauged on the macro level while the deterioration due to environmental exposure occurs on the micro level. Steel reinforcing bars having diameters ranging from approximately 1 to 4 cm and being spaced often no closer than 5 cm are ill suited to constrain reaction sites that exist on a scale of fractions of a millimeter and potentially all throughout the gap between adjacent reinforcing bars. Furthermore, though undoubtedly imparting a positive benefit to structural concrete, the embedded steel reinforcing bars are themselves the cause of the most financially impactful form of concrete deterioration, namely corrosion. The resulting incompatibility between needing reinforcement for ductility but having to deal with additional durability issues has required the concrete construction industry to spend hundreds of millions of dollars on an annual basis to conduct safety inspections and preform repairs on deteriorated components (Koch et al. 2001).

Into this void, the field of fiber reinforcement provides a unifying transition capable of addressing both ductility and durability issues simultaneously. With respect to ductility, the displacement capacity of conventional reinforced concrete is achieved due to the ability of steel to carry load across regions of cracked concrete. Fiber reinforcement provides the engineer with a composite material that can be tailored to meet the same criteria of providing a load transfer path across a cracked cementitious matrix. Though of dramatically different sizes, steel reinforcing bars and commercially available fibers both contribute load carrying capacity through a similar mechanism of interfacial bond. To achieve utilization of either steel reinforcing bars or fibers, an adequate length must be embedded on either side of a crack over which; 1) load is transferred from the intact composite on one side of the crack into the crack bridge by shear stress along the embedded bar/fiber interface, and 2) after passing the crack, the load is redistributed into the intact composite by a mirrored shear stress action. An indirect effect of the difference in size scale is the more homogenized distribution of this crack resistance in fiber reinforced concrete versus the concentrated region of crack resistance of steel reinforcing bars in conventional reinforced concrete. This distribution factor proves beneficial in practice because fibers can be found in close proximity to cracks formed at any section of concrete, effectively providing restriction at the microscale and limiting the “run” length available to cracks before they encounter a reinforcing obstacle.

Tangentially, it is important to note that the conclusions of this research program are not directed towards the total replacement of conventional steel reinforcement by fiber reinforcement as has been supported by various other researchers. Rather, it is the synergistic benefits that fibers and conventional reinforcement can impart that are deemed to provide the material most suitable to meet the demands of modern construction. Principally, literature which delves into the interfacial bond behavior between fiber reinforcement concrete surrounding steel reinforcing bars has identified a significant strengthening behavior because of the aforementioned restriction of microcracks generated by differential displacements across the interface. Very little has been done to establish how this bond behavior, identified under very low levels of displacement capacity, might be expected to withstand significant levels of deformation up to and beyond the yield strain of the reinforcing bar. Such scenarios are critical to developing an engineering understanding of how such a material might preform under critical levels of loading. Similarly, the behavior of high performance fiber reinforced cementitious composites are perceived to

respond better to extreme compression loading because of the ability of fibers to control shear crack development along the planes of principal loading but very little literature addresses the response of fiber reinforcement in conjunction with conventional transverse reinforcement. Isolating a quantitative improvement imparted by the introduction of fiber reinforcement may allow for relaxation of the seismic provisions which require extremely high reinforcing ratios to occur within seismic joints and aid in overall construction. With regard to these issues of ductility enhancement, the volumetric quantity of total reinforcement is not significantly changed but rather the introduction of fiber reinforcement allows for delocalization of reinforcement from conventional discrete points of steel bars to more distributed and uniform elemental response. Such a level of distribution also promises to be an effective crack deterrent at low levels of load under which the strain imparted on conventional steel reinforcing bars is unable to elicit a strong response due to element geometry (as occurs with bending) or weak bond formation.

It is this factor of distribution that also allows fiber reinforcement to be an effective deterrent to environmental deterioration and provide durability enhancement to concrete. Environmental deterioration occurs on a multitude of scales including ice formation within the pore structure of concrete, to rust formation on the surface of a reinforcing bar. Consequently, because of the variability in reaction site, a holistic durability enhancement must be present at a similar level of dispersion as all potential reaction sites. While this cannot be realized by steel reinforcing bars it is roughly achievable with engineered fiber reinforced composites. Yet, even once fibers are placed in proximity to the reaction sites, in order to be effective they still need to mitigate some form of induced cracking.

To understand the role of cracking in environmental deterioration it is necessary to address a commonality shared by many such environmental attacks. Whether considering microscale deterioration associated with freezing and thawing of internal moisture, salt crystallization within super saturated pores, alkali-silica gel swelling or the more macroscale deterioration of the aforementioned corrosion of reinforcing steel, each process is characterized by an expansive pressure being formed at a site surrounded by cementitious matrix/concrete. Picturing these reaction sites as isolated spheres surrounded by concrete, it is apparent that expansion of the sphere forces the surrounding concrete to strain in tension along a circumferential path. With a limited tensile capacity the concrete is forced to relieve pressure by cracking radially. Under continued environmental attack it is to be expected that the overall expansion of our supposed spheres would continue driving the radial cracks further outward. The crack network, created by this sphere and the many other spheres dispersed throughout the concrete around it, is responsible for generating large changes in the permeability of the concrete. Returning to the variety of expansive type environmental attacks being addressed, it can also be noted that water plays a common role in each, either as a reactant or as a carrier of a reactant in solution such that increasing the mobility of water to move through the concrete would be expected to drive the reaction faster and accumulate expansion more rapidly. It stands to reason that controlling the growth and networking of cracks can then be expected to limit the permeability increase suffered by concrete. Thusly, crack resistance is directly tied with reducing deterioration, both as a direct effect of expansion constraint but also indirectly by limiting the potential of continued expansion acceleration, and resultantly increases durability.

On a macro scale the ability of fiber reinforced cementitious composites to mitigate cracking is highly dependent upon properties of the fibers utilized. Fiber materials, volume percentage and geometry are all factors which will strongly influence the ability of a fiber reinforced composite to provide crack propagation resistance, being a measure of an increasing input energy

requirement necessary to grow a given crack and evidenced as deflection and strain hardening performance. The choice of fiber material controls the development of a shear stress bond between a given material and its surrounding of cement hydration products and the elastic stiffness of the fiber itself. Such properties are directly responsible for the level of closure stress that a given fiber can develop across a crack when providing localized crack growth resistance. In a cumulative sense, greater fiber contents incorporated into a composite provide a greater number of these localized restrictions which generate macroscale crack propagation resistance. Finally, at a given fiber content, fiber geometry, as comparing micro and macro fibers where differentiation is based on effective fiber size (length, diameter), is responsible for determining both the effective spacing between fibers and the crack displacement capacity. Utilization of microfibers is more likely to ensure the incorporation of a greater number of fibers in resisting a crack as it grows with each contributing to the resistance of further propagation. In contrast, utilization of macrofibers offers restraint of cracks having reached a larger displacement, attributed to the greater embedment length existing on either side of the crack allowing for consistent load transfer through the fiber. Further geometrical considerations regarding fiber shape can also play a role in providing closure stresses not solely dependent on the shear stress capacity of the interfacial bond but also owing to mechanical anchorage requiring the plastic deformation of the fiber material as in the case of hooked-end fibers, crimped fibers or twisted fibers.

Those composites that exhibit deflection hardening and strain hardening behavior are suggested to be best equipped to increase durability under threat of expansion-induced deterioration. In such composites, cracking initiation at a reaction site will in a short span intercept fibers that impart enough tensile capacity to stem further propagation. Under continued reaction/expansion the crack may propagate until again intercepting more fibers raising the cumulative crack restraint to stop further propagation. At each progressive stage the hardening effect requires more and more expansion pressure prior to further crack growth. This level of restraint differs from a non-hardening composite in which, due to fiber properties, successive growth steps after the initial restraint require less additional input energy. In such a scenario, cracking would still be restricted relative to a non-fiber reinforced element but the quantity of reaction products (i.e. ice, alkali silica gel, rust, etc.) necessary to propagate a crack far enough to connect with adjacent cracks or to the concrete surface would be far lower than necessary for an equivalent hardening material (Table 1-1).

Table 1-1 Comparison of Reaction Product Formation Necessary for Crack Development and Growth in Hardening and Non-Hardening Composites

	Hardening Composite	Non-Hardening Composite
Reaction Product (RP) for Initial Crack Development	$RP = RP_{\text{cracking}}$	$RP = RP_{\text{cracking}}$
Reaction Product (RP) for Subsequent Crack Growth	$RP \geq RP_{\text{cracking}}$	$RP < RP_{\text{cracking}}$

Gauging the effectiveness of a given selection of fibers to achieve this constraint of environmental deterioration can be addressed by a variety of processes. For the purposes of the research described herein successful mitigation is judged on the basis of; 1) crack suppression, 2) measurement of in-situ reaction rates relative to a reference sample either as a cumulative effect of reaction as in the case of alkali-silica reaction concrete expansion or direct reaction

measurement as in the case of steel corrosion, and 3) retention of concrete mechanical properties relevant to performing its function as a load bearing construction material.

Utilizing fiber reinforcement to provide mitigation to potentially deleterious processes occurring in concrete is not a heretofore unpopulated research topic. Rather, multiple researchers, with references in their appropriate chapters, having addressed such issues with highly specialized blends of fiber reinforced cementitious composites have produced encouraging results suggesting that the field of research holds promise for actual construction industry adoption. One of the reasons for which adoption has largely not occurred is that some of the previously studied composites are too highly specialized for the field of academic research and are not accessible to a typical construction project. This disconnect between academic research and actual construction with respect to fiber reinforcement has been manifested as very high fiber contents and significant issues with respect to concrete workability. High fiber content presents financial obstacles in that fiber reinforcement as an additive often requires a significant upfront cost to implement on top of conventional construction expenses with the magnitude of the cost directly tied to the fiber content. With respect to concrete workability, even without high fiber contents, the addition of fibers inherently reduces the workability of composite making it more difficult to place and ensure adequate compaction (and thereby adequate fiber dispersion) within reinforcing cages and formwork. To overcome these obstacles this research program has focused on generating significant crack resistance (deflection hardening behavior) under a limitation of 1.5 percent maximum total fiber volume, while simultaneously augmenting the workability of such mixes by marrying fiber reinforced concrete with concepts from the field of self-consolidating concrete.

1.1 Organization of the Dissertation

The experimental work conducted and described herein is presented in three distinct chapters.

The first chapter is devoted to the process of developing the Self-Consolidating Hybrid Fiber Reinforced Concrete material to meet the necessary criteria proposed for achieving a holistic durability enhancement. The material properties acting independently and in composite action with conventional steel reinforcement are described to highlight the enhanced performance characteristics achievable with hybrid fiber reinforcement with a closing discussion of the utilization of the material at the structural scale.

The second chapter is focused on the corrosion performance of Self-Consolidating Hybrid Fiber Reinforced Concrete composite elements. Specifically addressing the manner in which crack resistant properties modify the nature of steel reinforcement corrosion at both the initiation and the propagation phases of chloride induced corrosion.

The third chapter discusses the application of fiber reinforcement to mitigate the deterioration caused by alkali silica reaction. Both microfibers and hybrid micro/macrofiber suites are assessed for the constraint of the expansion brought about by alkali-silica gel formation with durability enhancement quantified by superior retention of relevant concrete mechanical properties.

Concluding remarks are offered in closing to tie together the issues of hybrid fiber reinforcement performance enhancement observed under the variety of loading scenarios addressed. Thoughts on both the status of current understanding of fiber controlled durability testing and the outlook for application to the intended market of the construction industry are offered.

After reading the description offered of the overall experimental process and discussion of results, the potential reader should gain an understanding of the intrinsic performance benefits that Self-Consolidating Hybrid Fiber Reinforced Concrete has over a reference Self-Consolidating Concrete mix for both mechanical performance (ductility) and durability enhancement. The reader will understand the reasoning for fiber geometry limitations in relation to material development and understand how hybridization of fiber type at low volume additions can produce outsized gains in performance due to the synergistic effects of micro and macrofibers. The reader will be able to identify the features of cover concrete that lend themselves to protection from corrosion of embedded steel reinforcement and understand the role of cracking and crack resistance during the propagation of corrosion damage. The reader will be able to identify a correlation between alkali-silica reaction induced expansion and a loss of intrinsic material stiffness and understand the role of fiber reinforcement in limiting this loss by confining the propagation of deterioration within the cement matrix surrounding the reactive aggregate particles. It is the author's hope that the evidence presented through experimentation leaves the reader with a general sense of the potential of Self-Consolidating Hybrid Fiber Reinforced Concrete to meeting the demands of modern age infrastructure.

2 SC-HyFRC Development and Properties

2.1 Introduction

In an effort to meet ever increasing demands in all facets of concrete construction and service life, technological aspects of concrete as a material have undergone a slow but definitive evolution through the addition of performance enhancing admixtures over the past few decades. Largely such additive measures are evolved to meet a specific deficiency within the realm of conventional concrete whether it is an inherent high labor demand during construction or a material characteristic such as brittleness. Two such technologies used to deal with the specific deficiencies listed above are Self-Consolidating Concrete (SCC) and Hybrid Fiber Reinforced Concrete (Hybrid FRC) respectively.

Self-consolidating concrete research was developed in Japan in the 1980s in order to combat the high labor demands necessary for concrete construction with the first published fundamental study of the material concept attributed to Ozawa, Maekawa, Kunishima and Okamura (1989). Specifically, the critical step of concrete placement and compaction was deemed to require a skilled labor force for which there was unmet demand in Japan at the time. As compaction is a necessary step in producing a concrete of any quality, the early research was focused on achieving compaction without the use of conventional vibration techniques by incorporating high fluidity into the concrete without sacrificing strength or introducing additional defects. Achieving a sufficiently flowable nature was suggested to require three deviations from conventional concrete mix proportioning; 1) a limitation on the aggregate content, specifically the coarse aggregate, 2) increasing mix viscosity by keeping water to binder ratios low, and 3) utilization of high-range water reducing admixture (Okamura and Ouchi 1999). Under such mix design guidelines, gravity directed flow was achieved by having a viscous cement paste carrying isolated coarse aggregate particles in suspension during placement. General interest in the topic of self-consolidating concrete spread to the US in the 1990s with multiple publications appearing in the American Concrete Institute Materials periodical. By the mid to late 1990s, advancements in chemical admixtures provided more efficient water reducing admixtures (superplasticizers) and viscosity modifying agents to supplement the influence of water to binder ratio (Nagataki and Fujiwara 1995). Additionally, the use of supplementary cementitious materials were incorporated to achieve the necessary high binder content without issues brought about by such high levels of portland cement (Khayat 1999, Bouzoubaa and Lachemi 2001). Such advances have translated into reductions in labor costs and construction site noise pollution and ensuring filling of densely congested reinforced elements which have contributed to the large scale adoption by the construction industry.

Fibers have long been understood to provide a beneficial level of crack resistance to the quasi brittle matrix of concrete with usage of steel fibers specifically dating back to the 1960s. Since then, fiber reinforced concrete, with both steel and other fiber material types, has been greatly expanded upon with respect to issues of fiber geometry and appropriate dosages. Early investigations into hybridization of fiber material types can be attributed to Walton and Majumdar (1975) with polypropylene and glass microfibers but soon after specialization of function led to primarily a single fiber type/geometry being studied independent of all others. By doing so, it was not until the 1990s that the synergistic effects of fiber hybridization were rediscovered. Hybridization, meaning the utilization of more than one fiber type in a given concrete mixture, is encompassing of mixing fibers of similar scale but different materials as done by Mobasher and Li (1996) with alumina and polypropylene or mixing fibers of the same material but at different scales as first done by Rossi (1997) with multiscale steel fiber

reinforcement. Combining both levels of hybridization, material and geometry, Lawler et al. (2002) tested steel macrofiber/polyvinyl alcohol microfiber blends which exhibited flexural behavior in excess of the sum of their individual components (steel or polyvinyl alcohol independently). Such synergy was attributed to the dual phase action of controlling microcracking and macrocracking for which each individual fiber was better suited. At the material level, it was further observed that polyvinyl alcohol microfibers produced a better stabilization of cracking leading to an overall load capacity increase than comparable steel microfibers when either was employed in combination with macrofibers. Geometrical variations within hybrid fiber mixes continued in polypropylene (microfiber), steel/polypropylene (macrofiber) research conducted by Banthia and Gupta (2004) with important considerations made to the effect of fiber hybridizing on the workability and entrapped air content of fresh concrete. In the work directly preceding this study, Blunt and Ostertag (2009) adapted hybridization to performance based criteria in the development of a three fiber, steel/polyvinyl alcohol Hybrid Fiber Reinforced Concrete (HyFRC) suitable for structural concrete. The blend of fibers in HyFRC shows strong synergistic tendencies with the 1.5 volume percent composite performance exceeding the response of any individual fiber at an equivalent 1.5 volume percent. The cracking resistance of HyFRC likewise demonstrated superior performance to individual fiber matrices with multiscale crack resistance available to restrict crack propagation under all stages of flexural loading. Consequently, HyFRC is characterized as deflection hardening which is observed experimentally as a hardening regime beyond the load at which cracking initiates under either flexural or tensile loading. In comparing the various steps of hybrid fiber reinforced concrete evolution, one of the greatest gains of constantly addressing and optimizing for the issues of fiber type/material has been the ability to produce the desired composite behavior at increasingly lower overall volumes of fiber reinforcement. With the workability of fiber reinforced concrete being one of the primary drawbacks to adaptation to conventional construction methods, such criteria will be necessary for producing a workable concrete that does not require a high degree of specialization in order to be utilized in the concrete industry.

2.2 Background

Combining these two fields of self-consolidation and fiber reinforcement is then a natural step to generating an overall improved composite having fewer deficiencies both during construction and as a matured material. The research opportunity at the nexus of these fields was undertaken within a short time after establishment of self-consolidating concrete with a specific focus on the behavior of steel fiber reinforced concrete under flow conditions (Kurita and Nomura 1998, Grunewald and Walraven 2001). Quickly, it was realized that the introduction of fibers at meaningful percentages imparted significant changes in flow characteristics. Utilizing one volume percent of steel macrofibers, Kurita and Nomura (1998) achieved flow by increasing binder material content to 500 kg/m^3 and the ratio of fine and coarse aggregate to 1.7:1, in essence taking some of the mix proportioning requirements of self-consolidating concrete further. Using low calcium fly ash at portland cement replacement levels between 0 and 20 percent was also noted to provide an elongated period of flow retention attributed to its slow acting pozzolanic reaction not contributing to the initial stiffening of the composite. Grunewald and Walraven (2001), utilizing a likewise elevated binder content of 590 kg/m^3 but a more traditional fine to coarse aggregate ratio of 0.8:1, investigated steel macrofibers ranging between 0.5 and 1.5 volume percent. Of significant interest, the behavior of differently sized steel macrofibers (30 to 60 mm in length) was compared and identified as a critical parameter in limiting the maximum fiber content due to clustering and blockages of fibers when designing

mixes which retained acceptable flow properties. This strong correlation between fiber length and maximum allowable fiber content, being only 0.5 volume percent for 60 mm length steel fiber, emphasized the importance of achieving a maximal fiber response at a limited fiber content since 0.5 volume percent is insufficient to achieving deflection hardening type behavior. Similarly, work conducted specifically targeting the application of self-consolidating behavior to concrete having 1.5 to 2 volume percent steel macrofiber reinforcement (Laio et al. 2006) encountered problems with reaching a desired level of flow absent the use of some level of external vibration. At these higher levels of fiber content the necessary reduction in coarse aggregate content to achieving unobstructed flow approaches a fine to coarse ratio of 2:1 in addition to an elevated binder content of 650 kg/m³.

With significant progress made on the utilization of steel fiber reinforcement within a self-consolidating concrete matrix the logical next step is the incorporation of fiber hybrids. Focusing specifically on research having been conducted on hybrid blends of macro and microfibers, the work of Akcay and Tasdemir (2012), Sahmaran et al. (2005) and Nehdi and Ladanchuk (2004) provide an interesting cross section to evaluate the current state of development and understanding. Akcay and Tasdemir (2012) were able to successfully incorporate up to 1.5 volume percent of steel fibers being 67 percent microfiber and 33 percent macrofibers with minimal loss in flow properties having utilized a binder content of 700 kg/m³. However, the resulting composite failed to meet the performance criteria of a deflection hardening material, being unable to stabilize crack growth prior to reaching a peak capacity. Sahmaran et al. (2005), limiting the total fiber volume to 0.75 percent with different combinations of steel micro and macrofibers, achieved flow behavior with a binder content of 570 kg/m³ and a fine to coarse aggregate ratio of 1.7:1. Possibly due to the low fiber percentages within their investigation, specific tendencies for correlation between flow diameter loss and micro versus macrofiber could not be extracted. Nehdi and Ladanchuk (2004), being one of the first to look at hybrid material fiber reinforcement in self-consolidating composites, successfully utilized 0.25 volume percent of polypropylene microfibers with 0.75 percent steel macrofibers in concrete having a binder content of 550 kg/m³ and equivalent amounts of fine and coarse aggregate. Of significant interest are the observations made of the workability problems encountered with the inclusion of the microfibers, requiring a 16 percent increase in high-range water-reducing admixture versus equivalent macrofiber only mixes to compensate. Even with one percent total fiber volume, the resulting composites performed very poorly, with no hardening and abrupt softening exhibited during flexural testing.

Many of the aforementioned research into the area of self-consolidating fiber reinforced concrete have furthered the original work of Okamura in pursuing flow characteristics through the same parameters employed to conceptually develop self-consolidating concrete. Focusing specifically on the binder content and fine to coarse aggregate ratio as parameters, Table 2-1 highlights the range of values that have been utilized to reach a state of flowable concrete at different fiber contents.

Table 2-1 Summary of Previous Selected Work on Combined SCC/FRC

Author	Binder Content, kg/m ³	Fine to Coarse Agg. Ratio	Macrofiber Content, %	Microfiber Content, %	Flowable Concrete ¹	Hardening Behavior
Nagataki (1995) ²	500	1.0	-	-	Yes	-

Kurita (1998)	500	1.7	1	-	Yes	n.a.
Grunewald (2001)	590	0.8	0.5 – 1.5	-	Yes, for $V_f < 0.5$	n.a.
Laio (2006)	650	2.0	1.5 - 2	-	Marginal	Yes
Akçay (2012)	700	n.a.	0.5	1.0	Yes	No
Sahmaran (2005)	570	1.7	0 - 0.75	0.75 - 0	Yes	n.a.
Nehdi (2004)	550	1.0	0.75	0.25 ³	Yes	No

¹Defined as non-segregating flow having diameter greater than 600 mm in the slump flow test

²Nagataki parameters indicative of early SCC proportioning

³Only non-steel fiber material (polypropylene)

It is apparent that while combining self-consolidating and fiber reinforced concrete methodologies is doable, the challenge of achieving a high performance material meeting the performance criteria of deflection hardening remains. Utilization of a total fiber volume of 1.5 percent as required for producing the deflection hardening characteristics of the HyFRC developed by Blunt and Ostertag (2009) will mandate further optimization of the concrete mix proportions to obtain a flowable, anti-segregating composite.

2.3 Materials and Test Methods

For the developmental stage of incorporating self-consolidating behavior in HyFRC, cementitious materials consisted of commercially available Quickcrete portland cement conforming to ASTM C150 Type I/II and fly ash conforming to ASTM C618 Class F. The aggregates, coarse and fine, were both locally sourced pea gravel with a maximum size aggregate of 9 mm from Madison, CA and sand with a measured fineness modulus of 3.2 from Pleasanton, CA respectively.

Chemical admixtures were provided by BASF Admixtures, namely Glenium 3030NS polycarboxylate superplasticizer and Rheomac VMA 358, an organic viscosity modifying admixture (VMA). In order to maximize the benefits of technological gains in admixture engineering, mixes were re-proportioned as product releases were introduced by BASF. This included the usage of Glenium 7500 and Rheomac VMA 362, being both a generation newer than Glenium 3030NS and Rheomac VMA 358. In practice, it was noted that the new products were able to deliver the same performance of their predecessor at lower dosages allowing for further refinement of the overall mixture.

Fiber reinforcement was provided by two types of Dramix steel macrofibers produced by Bakaert and Kuralon polyvinyl alcohol (PVA) microfibers produced by Nycon, with material and geometry properties described in Table 2-2. The available suite of fibers was identical to the ones utilized in the original HyFRC mixture by Blunt and Ostertag (2009).

Table 2-2 Fiber Properties

Fiber	Material	Length (mm)	Aspect Ratio (L/D)	Tensile Strength	Elastic Modulus
-------	----------	-------------	--------------------	------------------	-----------------

				(MPa)	(GPa)
RC-80/60-BN	Steel	60	80	1050	200
ZP 305	Steel	30	55	1100	200
RECS 15	PVA	8	200	1600	43

For composite property testing, in which the influence of SC-HyFRC upon internal confinement and tension stiffening was investigated, Grade 60 steel reinforcing bars and Grade 40 steel wire were used to fabricate the relevant reinforcing ratios of cylindrical and prismatic specimens.

All concrete mixing was performed in the concrete laboratory at the University of California, Berkeley using vertical axis pan mixers. The available inventory of mixers (Figure 2-1) allows for scale up production as necessary to meet volume demands.

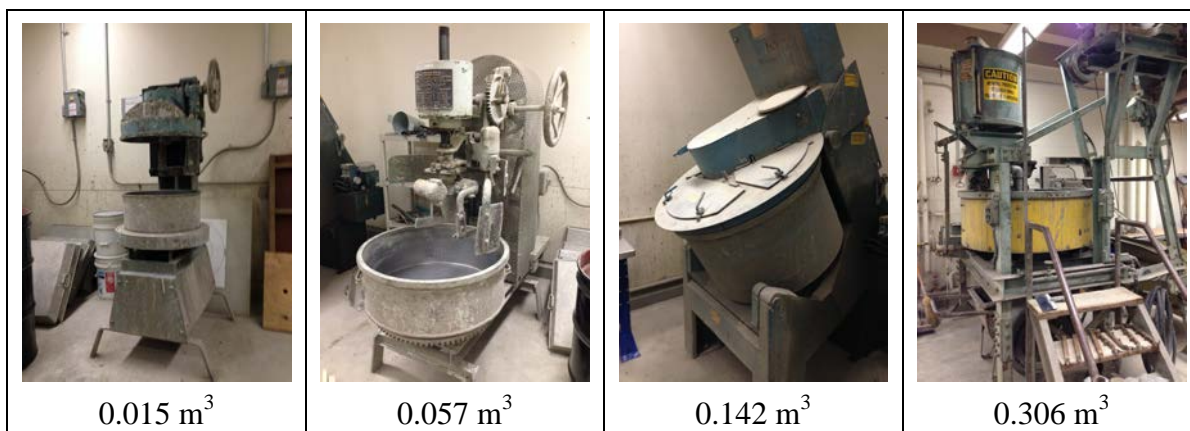


Figure 2-1 On-Site Mixers and Capacities at UC Berkeley Concrete Laboratory

Actual batch mix volumes ranged from 0.008 cubic meters for trial mix batches up to 0.300 cubic meters for casting single lifts of scaled bridge column specimens. The mixing process consistently involved; 1) mixing all binder components with all fine aggregate until blended, 2) adding all coarse aggregate with continued mixing for between 30 and 60 seconds, 3) adding three quarters of the liquid component, consisting of the water with pre-added chemical admixtures (superplasticizer and VMA) with mixing continued until the mixture is homogenous, 4) adding all of the PVA microfibers by “sprinkling” them into the pan quickly followed by the remaining liquids component, 5) upon no longer being able to easily distinguish PVA fibers, all steel fibers were slowly poured into the pan while mixing to avoid clumping in one location. For many mixtures, a small percentage (10 percent) of the chemical dosages was held back and added based on a subjective determination of the propensity for fibers to clump with an additional amount held as extra if needed. In general, it was noted that the largest batches required less relative chemical admixture dosage than the small batches but an insufficient number of large batches were run to provide an exact quantification.

Characterization of the flow properties of mixes was made based on the results of the slump flow test. Each slump flow test was carried out by filling a standard upright slump cone without compaction and measuring the horizontal spread of the concrete in orthogonal directions when the cone was lifted as prescribed in ASTM C1611 (2014). The slump flow test also allowed for determination of segregation tendencies of each mix by visual inspection of the spread behavior. If fine and coarse aggregates were not present in the outermost edge, the mix was determined to

have undergone “concrete segregation”. The flow behavior of fibers within concrete was analyzed by measuring the presence and concentration of fibers within the outermost 50 mm ring of spread and by inspection for “fiber clumping” behavior within the initial slump cone diameter leading to an interlocked fiber mound structure at the center of the concrete spread. Failing either of these visual measurements resulted in labeling of that trial mix as suffering “fiber segregation”.

During later stages of development, as mixture flow consistency reached an optimized condition, the passing ability of promising trial mixes was measured through reinforcement obstructions in a manner similar to ASTM C1621 (2009). Reinforcement cages designed to mimic the reinforcing ratios and clear spacing encountered in laboratory testing specimens and structures were used to gauge the interaction between macrofiber reinforcement and limited clear spacing of adjacent obstructions. The two cage geometries were constructed to represent the hinging base section of circular reinforced columns (Figure 2-2a) and tight transverse tie reinforcement of rectangular reinforced concrete beams (Figure 2-2b), with both structure types having the potential to gain significant improvements from fiber reinforced concrete ductility enhancement.

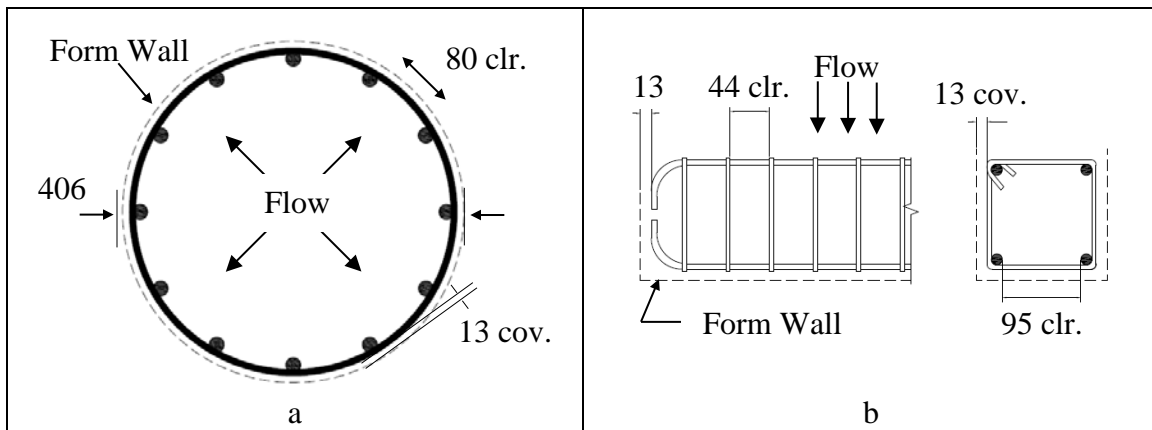


Figure 2-2 Reinforcing Layouts for Passing Ability Assessment, mm

Reinforcement cage orientation allowed for analysis of the difference in passing ability when the direction of flow through the obstruction was either perpendicular (Figure 2-2a) or aligned (Figure 2-2b) with gravity. The clear spacing between adjacent obstructions should also be highlighted, being 80 mm for the circular cage and 44 mm for the rectangular cage. With a strong correlation between fiber length, clear spacing and maximal fiber inclusion having been established by Grunewald and Walraven (2001), incorporating 60 mm length RC-80/60-BN fibers given the testing conditions poses significant challenges.

Material properties of the hardened composite were measured by compression testing (ASTM C39 2014) and 4-point bending tests (ASTM C1609 2012). Compression testing was conducted on cylinder samples having dimensions of either 102 mm diameter by 203 mm height or 152 mm diameter by 305 mm height with load recorded by a load cell placed in line with the hydraulic piston of the 1330 kN SaTEC compression machine and axial deflection of the middle half of the cylinder height measured by an aluminum compressometer having linear variable displacement transducers (LVDTs) affixed to opposing faces. Flexural testing was performed on 152 mm by 152 mm by 610 mm beam samples tested in 4-point bending with a span length of 455 mm. Testing was conducted on a 534 kN Universal Testing Machine with midspan

displacement measured as the average of LVDTs located on opposite beam faces and affixed to a bending yoke. Measurements of load and displacement were recorded at a frequency of 1 Hz to capture any instability caused by sudden cracking.

2.4 Parametric Development

As the principal goal of this project was to add self-consolidating features to the HyFRC mixture of Blunt (2009) without losing the characteristic deflection hardening behavior, an assessment of the original mix with specific attention to the parameters of binder content and fine to coarse aggregate ratio as had been addressed by the researchers in Table 2-1 was warranted. Such a comparison is provided in Table 2-3 with the range of values of SC-FRCs established in Table 2-1 presented for comparison.

Table 2-3 SCC Parameters of HyFRC

	Binder Content, kg/m ³	Fine to Coarse Agg. Ratio	Macrofiber Content, %	Microfiber Content, %	Flowable Concrete	Hardening Behavior
Table 2-1	500-700	0.8-2.0	0.5 – 2.0	0-1.0	Yes	No
HyFRC	423	1.1	1.3	0.2	No	Yes
SCC ¹	530	2.0	-	-	Yes	No

¹Using 400 mL/100 kg binder of Glenium 3030NS and Rheomac VMA 358

From this simplified comparison, it is readily apparent that an increase in binder content will be required in addition to a likely increase in the ratio of fine and coarse aggregates. Specific to the fiber contents of HyFRC, only the mixes of Grunewald and Walraven (2001) and Laio et al. (2006) hold comparable contents (>1 percent), while only Nehdi and Ladanchuk (2004) had a similar polymer microfiber but specifically noted the requirement of higher superplasticizer dosages. Before incorporating fiber reinforcement a reference self-consolidating concrete mixture (“SCC” of Table 2-3) was fabricated with the available materials outlined in the previous section in order to validate the concept with the mixing equipment and processes utilized. The reference SCC mixture was characterized by a binder content of 530 kg/m³ comprised of 75 percent portland cement and 25 percent Class F fly ash in an effort to offset cost and carbon footprint considerations and a fine to coarse aggregate ratio of 2.0 in anticipation of encountering the same difficulties as experienced by Laio et al. (2006). Such a mixture utilizing the average recommended dosages of superplasticizer and VMA produced non-segregating flow having a diameter of 700 mm, sufficiently meeting the criteria of self-consolidating concrete.

Subsequently, a parametric study was undertaken to optimize the flow behavior of the mixture without sacrificing deflection hardening as exhibited in the flexural test. A secondary objective judged the composites on the basis of reaching a compressive strength of 35 MPa by 28 days having only an initial 7 days of wet curing, deemed necessary to meet performance based criteria of high performance fiber reinforced concrete. At the same time, high strengths brought about by substantially lowered water to binder ratios were avoided due to the corresponding increase in the critical fiber volume needed to stabilize matrix cracking and the fiber content already being a limiting factor in SCC type mix development. The primary parameters under investigation during the parametric study were; 1) admixture dosages, 2) binder content, 3) aggregate content/ratio and 4) fiber content/distribution. Trial mixing commenced with

production of 0.008 m³ batches targeting isolated changes in one or more parameters with an iterative process employed to direct future batches toward an optimal state. For each parameter, experimental results are discussed with thoughts on the relative interaction between different parameters offered. Visual indications of the progress made by this method are provided after the discussion in Figure 2-4 with segregation being increasingly limited in images going left to right. Also important to note is the fiber clumping behavior being progressively lessened with optimization of the aggregate and binder contents.

2.4.1 Admixture Dosage

Having already established that the average recommended dosages of chemical admixtures (400 mL/100 kg binder for superplasticizer and VMA) could produce self-consolidating concrete, the inclusion of the HyFRC fiber suite was tested to determine mix stability and flow loss. The effect of fibers (1.3 percent macro, 0.2 percent micro) in combination with mid-level chemical admixture dosages was observed to cause a significant loss in fluidity and non-consolidating behavior with the slump flow test appearing more similar to a standard slump cone test of conventional concrete. Conversely, using the minimum and maximum recommended dosages of superplasticizer (195 and 1170 mL/100 kg binder) and VMA (130 and 650 mL/100 kg binder) resulted in a non-flowing and a segregated mix in which the cement paste and fibers failed to move together respectively. This type of segregation is caused by an insufficient viscosity of paste having been developed. In the context of a fixed binder content, this issue of paste viscosity was addressed by working in ranges of VMA dosage exceeding the manufactures recommendation and simultaneously reducing the superplasticizer dosage to a level significantly lower than the maximum allowable dosage. The opposing directions of chemical admixture dosage change is attributed to a greater viscosity being needed to carry fibers than aggregate particles due to their higher propensity to bundle and clump upon contact contrasted with the incorporation of 25 percent replacement of portland cement by Class F fly ash in itself imparting some level of flow enhancement based on the spherical nature of fly ash particles and requiring less water for surface coating during the mixing process. For continuity during the trial batch process, when not directly testing changes in chemical admixture dosages, superplasticizer and VMA were scaled with changes in binder content to allow for measurement of paste content changes absent specific changes in paste viscosity. Throughout the trial batch mixing process it was generally observed that high dosages of superplasticizer produced unrecoverable segregation, while high dosages of VMA resulted in incorporation of a high content of air, being visible as bubbles rising to the surface when the mixture was static. Both issues were greatly assisted by the introduction of the newer Glenium and Rheomac products which exhibited superior performance and kept entrapped air contents below 4 percent as measured by a concrete air meter. Included in Appendix A is a grid outlining a selection of the ranges of dosages investigated with regions marked for having insufficient properties independent of any changes in binder, aggregate or fiber content. Under the initial admixtures, the best flow performance was associated with dosages of 660 and 2200 mL/100 kg binder for superplasticizer and VMA respectively. With the improved segregation resistance of the new admixtures, the superplasticizer dosage could be increased to 880 mL/kg binder allowing for greater flow while remaining a cohesive material.

2.4.2 Binder Content

In order to meet the compressive strength objective, the impact of a 25 percent Class F fly ash replacement of portland cement at various water to binder ratios between 0.54 (the water to

cement ratio of HyFRC) and 0.40 was investigated. Due to the slower rate of composite strength gain occurring in the pozzolanic reaction of fly ash versus portland cement hydration, the optimum value was determined to be 0.45. Using this water to binder ratio resulted in 28 day compressive strengths consistently being measured as 38 ± 2 MPa using the prescribed curing procedure.

Binder content as a percentage of overall volume was addressed by assessing the relative change in performance with increasing binder contents as discussed by the authors of Table 2-1. With cement paste being the fluid like element within fresh concrete, an increase of the cement paste volume fraction was expected to result in increased flow diameters. However, when increasing the total binder content as high as 620 kg/m^3 , no measureable differences in flow diameter were recorded under constant chemical admixture dosage ratios, suggesting that aggregate/fiber spacing within the cement suspension was not the limiting factor in flow behavior. Moreover, at higher binder contents a noticeable increase in concrete segregation susceptibility was observed. Upon reaching 620 kg/m^3 of binder the volumes of paste (binder plus water) and aggregate in the composite were equivalent, with further extension deemed undesirable due to cost considerations. Having been best able to control the segregation tendencies of the cement paste along with reaching equivalent flow properties, 530 kg/m^3 of binder was determined to provide an optimal response to the performance criteria.

2.4.3 Aggregate Content

Having already adopted a high fine to coarse aggregate ratio in anticipating problems with coarse aggregate to fiber interactions, a further decrease of coarse aggregate content was addressed. By increasing the ratio from 2.0 to 2.5, flow behavior showed general improvements without any additional threat of segregation. Holding all other mixture components constant, the substitution of part of the coarse aggregate with additional fine aggregate produced flow diameter changes of 200 mm. Additionally, the increased content of fine aggregate significantly altered the trend for a residual mound of material to remain within the original cone diameter by reducing the highest point of the slump test from 125 to 40 mm. Concerns regarding the high content of fine aggregate and the associated high specific surface area requiring a higher water/paste content for lubrication were addressed by the already elevated binder content and the high dosages of chemical admixtures that would not have been present in conventional concrete. While it is quite likely that further extension of the parameter, and the creation of a self-consolidating hybrid fiber reinforced mortar, may have resulted in continued improvements in overall flow properties, additional investigations were not undertaken due to having reached the desired performance.

2.4.4 Fiber Content

The original HyFRC, developed by performance based design concepts, included 1.5 total volume percent of the three types of fibers listed in Table 2-2 with the RC-80/60-BN accounting for 0.8 volume percent, the ZP305 accounting for 0.5 volume percent and the RECS15 the remaining 0.2 volume percent. As previously mentioned, the results of Grunewald and Walraven (2001) specifically highlight the challenges of incorporating long fibers in a self-consolidating concrete mix. Such problems are brought about by the interlocking and clumping nature of such fibers and are exacerbated by the hooked end geometry. Such behavior was consistently observed in the trial batch mixing process, with no parameter changes in paste or aggregate able to disperse a mix having 0.8 volume percent RC-80/60-BN regardless of the content of the other fiber types. In order to determine the maximum allowable large fiber content, it was decided to

start at zero inclusion with the other fiber contents held steady and increase the 60 mm fiber content in steps of 0.1 volume percent until fiber flowability was affected. Under such conditions the maximum allowable total fiber content was determined to be 1.0 percent (0.3, 0.5, 0.2 volume percent for RC-80/60-BN, ZP305 and RECS15 respectively). Similar testing concluded that the maximum 60 mm fiber content was 0.2 volume percent in the presence of 0.8 and 1.1 volume percent of ZP305 fibers and 0.2 volume percent of RECS15 producing hybrid blends having 1.2 and 1.5 volume percent total fiber contents. At RC-80/60-BN fiber contents below the cap (0, 0.1 and 0.2 percent), the flow characteristics were defined by slump flow diameters of 600, 550 and 520 mm respectively having consistent 0.2 volume percent RECS15 and 1.5 volume percent total fiber (1.3, 1.2, 1.1 volume percent ZP305).

Subsequent testing for the propensity of RC-80/60-BN fibers to bridge the space between adjacent reinforcing bars in custom designed reinforcement cage mock-ups (Figure 2-2) revealed that even at a reduced volumetric ratio of 0.2 percent, interlocking blockages reduced overall flowability and did not meet the criteria required of self-consolidation. With adjacent reinforcing bar blockages placed at a clear distance of 44 mm (versus a fiber length of 60 mm) the reinforcement cage mock-ups required manual manipulation to achieve compaction. Similar problems were also encountered with the passing ability of 60 mm steel fibers when encountering obstructions spaced 80 mm apart. Furthermore, the presence of a formwork “wall” barrier in the vicinity of bar obstructions highlighted the difficulty which longer steel fibers encountered regarding adjusting their directionality as the flow direction of the matrix reoriented perpendicularly in order to provide maximum filling ability in the form. Such placement difficulty presented a unique problem of not being able to maintain a homogenous distribution of fibers within the section most susceptible to cracking, the cover layer of concrete. ZP305 steel fibers having lengths of 30 mm suffered far less from blockages under the clear spacing limitation of 44 mm and moved freely between bars spaced at 80 mm in the circular j-ring and the 94 mm distance between adjacent longitudinal bars of the rectangular form. Based on the limited set of information, it is hypothesized that clear spacing limits of 1.5 times the maximum fiber length should be employed to reduce problems associated with fiber passing ability.

A final decision of whether to proceed with 0.2 volume percent of the RC-80/60-BN fiber was made by comparing the flexural response of mixes having 0.2/1.3/0.0 and 0.2/1.1/0.2 volume percent of RECS15/ZP305/RC-80/60-BN fibers respectively to determine the influence of a low percentage of large fibers on deflection hardening behavior. Beam samples having dimensions of 152 mm by 152 mm by 610 mm were fabricated with the usual curing procedure and loaded in 4-point bending with a span length of 455 mm. As is apparent from Figure 2-3, a determination was made that low concentrations of the 60 mm steel fiber were inconsequential to the overall response within the deformation range of interest and could be discarded in favor of improved flow characteristics. Promisingly, the performance of the hybrid fiber blend of 1.3 volume percent ZP305 and 0.2 volume percent RECS15 (“1.5% total w/o 60 mm SF” in Figure 2-3) showed the expected deflection hardening behavior with a shallow softening behavior brought about by the loss of the long fiber. The fact that the mixture with 0.2 volume percent of 60 mm steel fiber underperformed at larger displacement is likely indicative of not reaching an even dispersion of steel fibers in the sample.

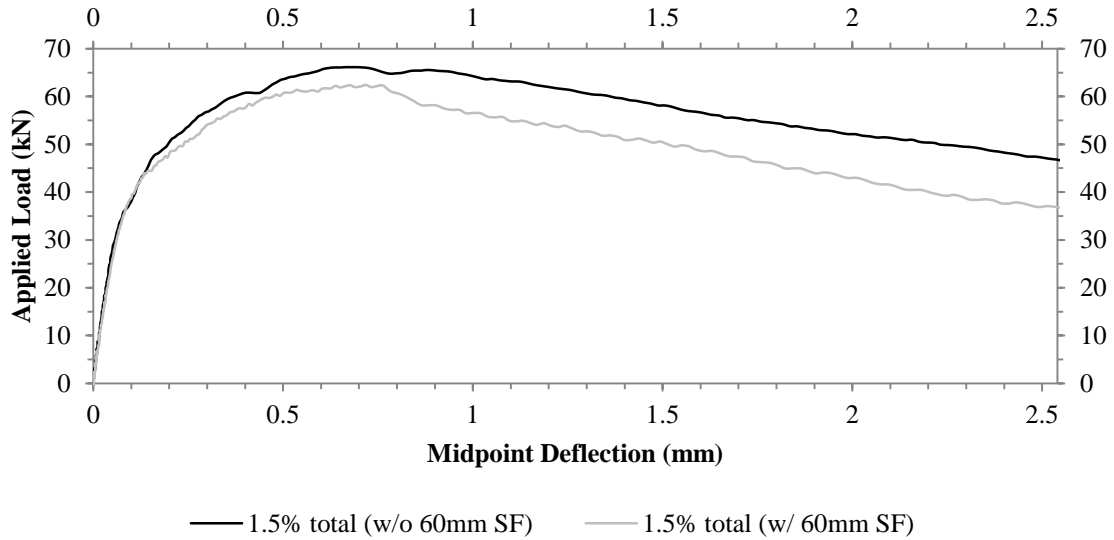


Figure 2-3 4-Point Bending Response with and without 0.2 Volume Percent 60 mm Steel Fiber

As discussed by Nehdi and Ladanchuck (2004) incorporation of polymer microfibers within a self-consolidating concrete matrix was observed to have a significant influence on reducing the ability of the composite to meet flowability criteria. In the mixes of this program, PVA microfiber addition was observed to have a much larger impact per unit fiber volume on flow properties than steel fibers. To quantify this difference, trial mix testing was conducted to isolate the slump flow changes experienced when increasing the PVA fiber volume from 0 to 0.2 and from 0.2 to 0.3 percent, with resulting flow diameters decreasing by 200 and 100 mm respectively. The results reveal that the RECS15 PVA fiber is responsible for reducing slump flow on the order of 100 mm for every 0.1 percent increment in volume within the range of material proportions studied. However due to 1) their necessary inclusion for generating stable crack propagation behavior in addition to 2) the fact that PVA microfibers themselves did not suffer from the passing ability problems that their steel macrofiber counterparts experienced under logical obstruction spacing, their impact was tolerated and counterbalanced by refinement of the other parameters to boost flow properties. In a general context, the importance of PVA fiber addition within the concrete matrix to restrict microcracking is critical but due to the problems they impose their use should be minimized as much as possible when workability is a concern.

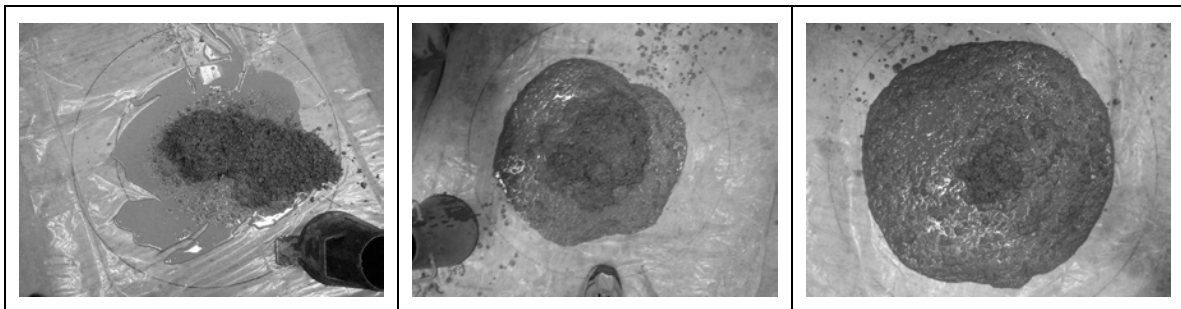


Figure 2-4 Concrete “Flow” Characteristics at Subsequent Stages of Mixture Development, with Decreasing Segregation Tendency Shown from Left to Right

2.4.5 Self-Consolidating Hybrid Fiber Reinforced Concrete

The parametric study identified the contents of chemical admixtures, binder, aggregate and fibers that produced the composite that best met the performance criteria (Figure 2-5). Shown with the original HyFRC mixture as well as the reference SCC mixture in Table 2-4 for comparison, the Self-Consolidating Hybrid Fiber Reinforced Concrete (SC-HyFRC) has fresh state properties defined by a slump flow of 600-650 mm allowing it be placed in unreinforced formwork without any external vibration. For placement in conventionally reinforced elements it is suggested that limited vibration be applied when clear spacing is reduced lower than 45 mm. Without limited vibration in these scenarios, the mixture will consolidate but the resulting fiber dispersion is not uniform.

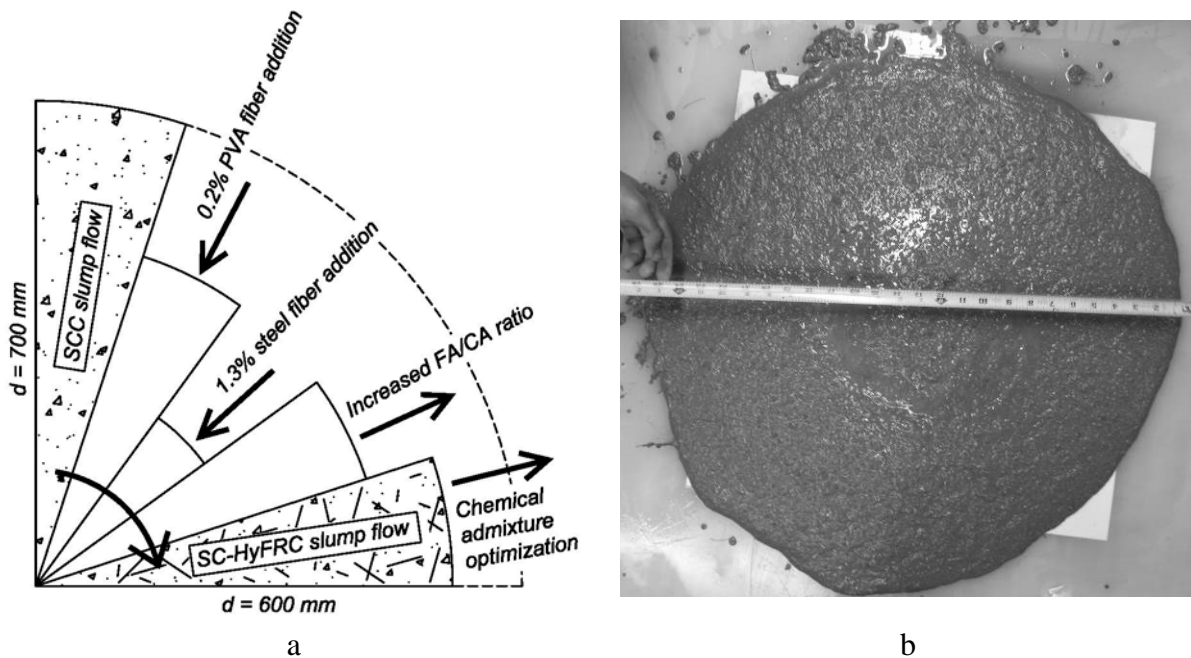


Figure 2-5 Slump Flow Behavior of SC-HyFRC; a) Influence of Parameters, b) Slump Flow Test

Table 2-4 Concrete Mix Compositions (kg/m^3)

	HyFRC	SCC	SC-HyFRC
Cement	423	397	397
Fly Ash	-	131	131
Water	228	237	237
Coarse Agg.	775	497	418
Fine Agg.	853	1006	1044
Glenium 3030NS ^a	-	400	880
Rheomac VMA 362 ^a	-	400	2200
RC-80/60-BN ^b	0.8	-	-
ZP 305 ^b	0.5	-	1.3
RECS 15 ^b	0.2	-	0.2

^a in mL/100 kg binder

^b in volume percent

Material property testing of the SC-HyFRC composite was conducted to characterize the cracking toughness of the included 1.5 volume percent of hybrid fibers. Tests included standard compression tests of 152 mm diameter cylinders, direct tension tests of dog-bone style specimens having a critical cross sectional area of 68.9 cm² and 4-point bending tests of 152 mm square by 610 mm beam elements with samples results presented in Figure 2-6.

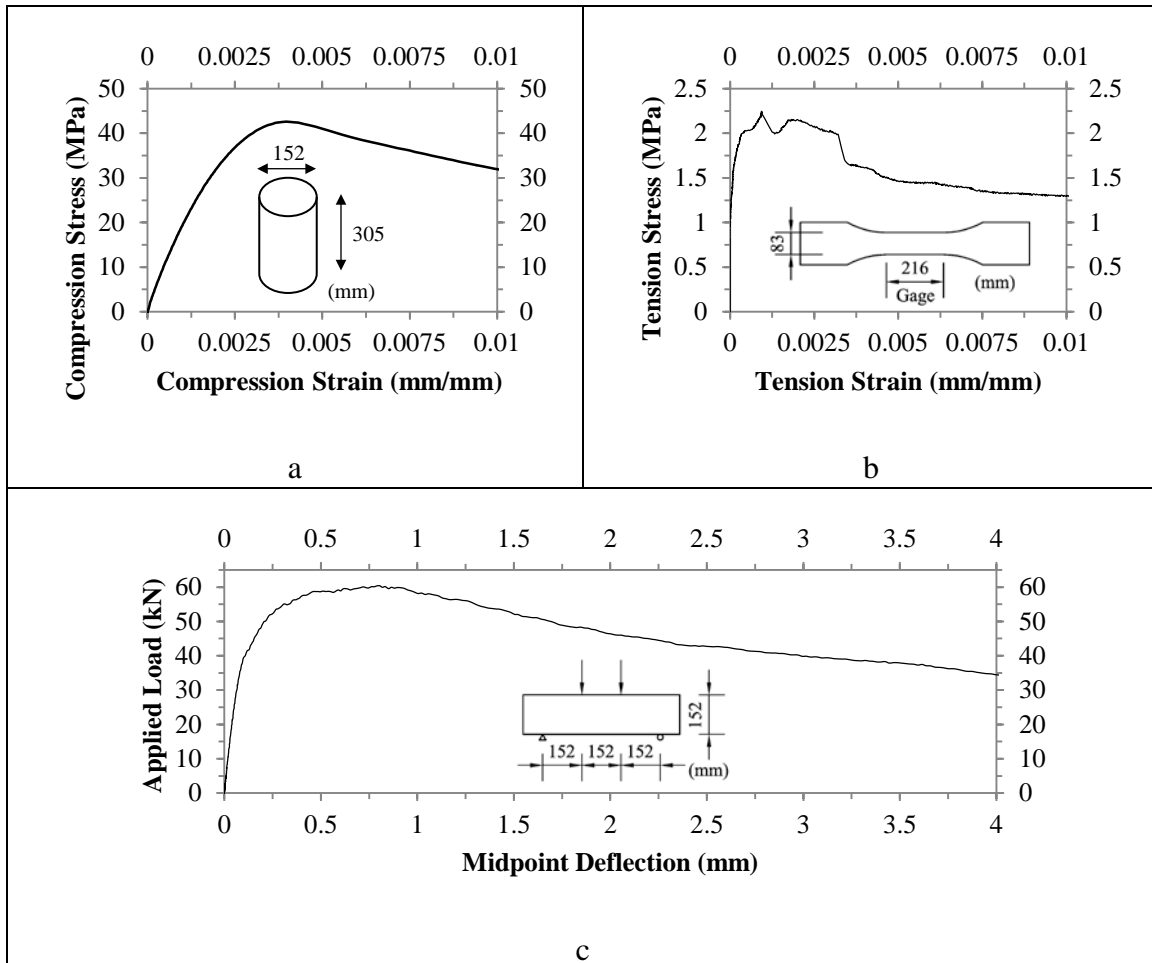


Figure 2-6 Mechanical Properties of SC-HyFRC; a) Compression, b) Direct Tension, c) 4-Point Bending

Evident from the material property testing is that SC-HyFRC has sufficient cracking resistance to provide significant residual capacity beyond the peak load. At one percent strain in compression and tension, this capacity is responsible for carrying 76 and 58 percent of the peak loads allowing for significant ductility that would not be present in a conventional concrete. In the pre-peak regime, the material shows deflection hardening response in flexure (Figure 2-6c) and a delay in strain localization up to 0.3 percent strain in direct tension (Figure 2-6b). While some fiber reinforced cementitious composites report the occurrence of strain hardening up to strains in excess of 2 percent, it must be noted that those tests are largely run on plate samples of limited thickness in which fiber alignment in the direction of loading allows for maximum fiber efficiency. Such is not the case in a larger cross section such as the dog-bone samples here,

where fiber distribution is random and a greater correlation to actual structural element performance can be gained.

2.5 Composite Performance

Having established the SC-HyFRC mixture proportions and material properties, testing of conventionally reinforced composites of the material was performed to characterize the various improvements that cracking resistance was responsible for. These included characterization of the intrinsic confinement properties of fiber reinforcement under compression, investigating composite flexural action in which compression and tension loads are shared by concrete and steel reinforcement, and direct composite tension testing in which plasticity spreading and overall ductility of the steel reinforcement is strongly influenced by composite bond distribution.

2.5.1 Internal Confinement

Testing to identify the internal confinement capabilities of the SCC and SC-HyFRC mixes was conducted on cylindrical samples having a diameter of 152 mm and a height of 305 mm (Figure 2-7a). Each cylinder was reinforced with four evenly spaced #3 steel reinforcing bars ($f_y = 375$ MPa) longitudinally, resulting in a reinforcing ratio of 1.6 percent. Variable confinement was provided by changing the spacing of spiral reinforcement provided by steel wire ($f_y = 275$ MPa) such that the transverse reinforcement ratio varied between 0.3, 0.5, 1.0 and 1.9 percent. Testing was conducted on the 1330 kN SaTEC compression machine with the axial deflection measured by the compressometer pictured in Figure 2-7b and by displacement of the loading plates. The lateral spacing between concrete and the aluminum collars to which the LVDTs were attached, in addition to the LVDT maximum displacement allowed for precision reading to be taken up to a maximum of approximately 2.3 percent axial shortening (Figure 2-9a). This range was shortened if dilation of the concrete produced bearing stress on the aluminum collar or the induced cracking caused the collars to rotate and over-compress one LVDT. Under such conditions the load was stopped and the collar removed with further displacement readings taken based off wire pot measurements of the relative movement of the steel loading plates. Due to the difficulty in decoupling the load taken by the concrete from the load taken by the longitudinal steel beyond the peak load, load values were not normalized by a specific area but are instead presented as composite load.

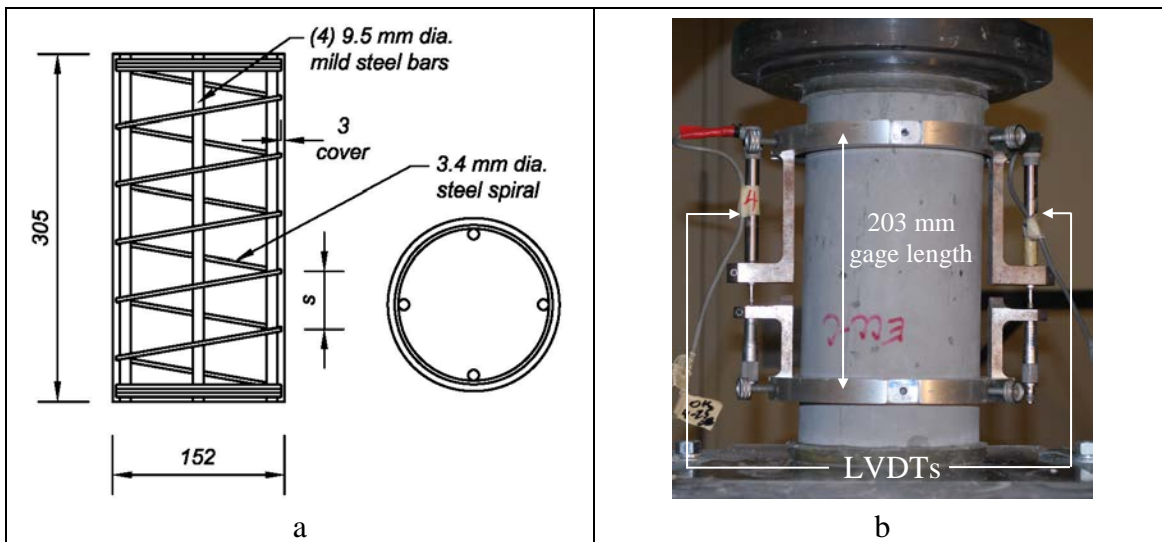
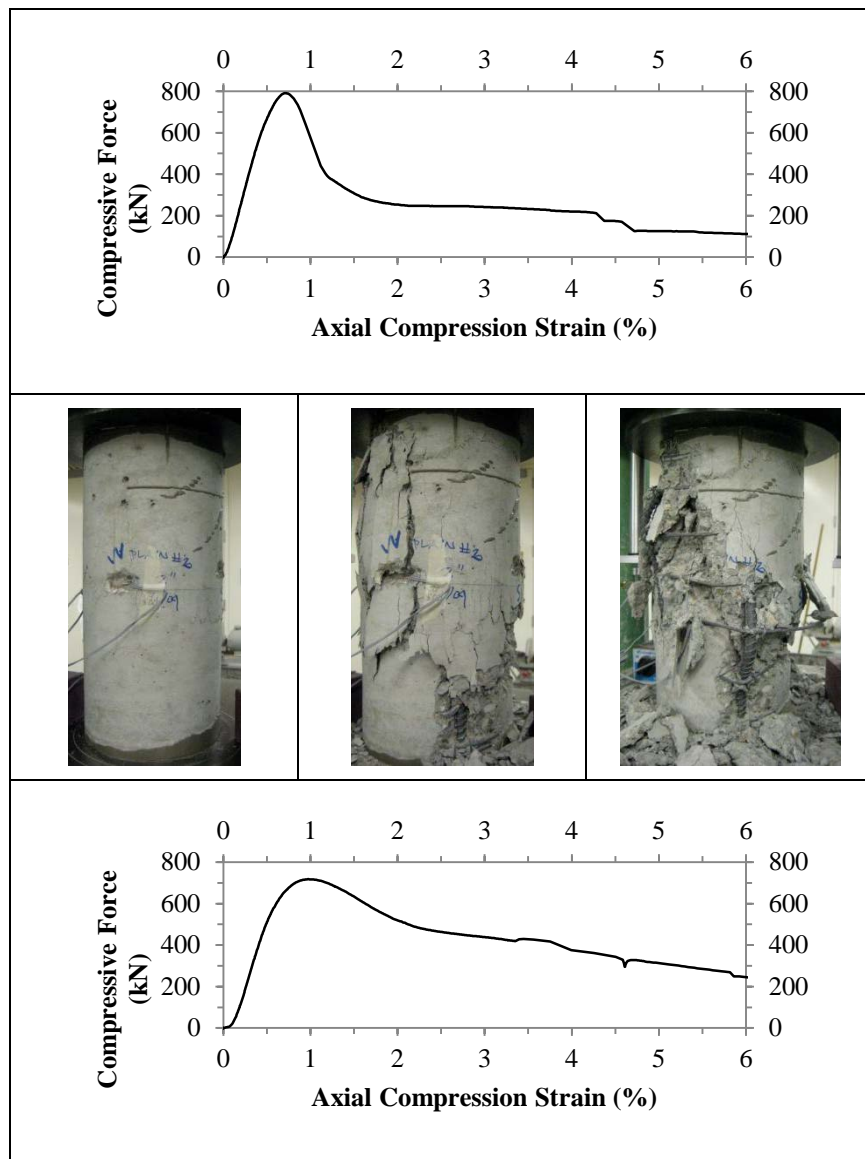


Figure 2-7 a) Confinement Cylinder Specimens with Variable Spiral Spacing, mm, b) Testing Setup with Compressometer in Place

During testing, photographs of the damage progression were taken of the cylinders at specific axial shortening values to compare spalling and lateral dilation of fiber reinforced and non-fiber reinforced concretes. Specifically at a transverse reinforcing ratio of 0.5 percent (Figure 2-8) but broadly representative of reinforcing ratios between 0.3 and 1.0 percent, the SCC specimens were observed to undergo spalling soon after reaching the peak load and spreading to a significant portion of the cylinder surface by an axial strain of 3 percent with concrete crushing initiating by 2 percent and spiral fractures and longitudinal bar buckling occurring by 5 percent strain. Comparatively, the presence of fibers resisted the spalling behavior at 3 percent strain and induced less pressure on the transverse spiral steel, limiting the development of steel fracturing.



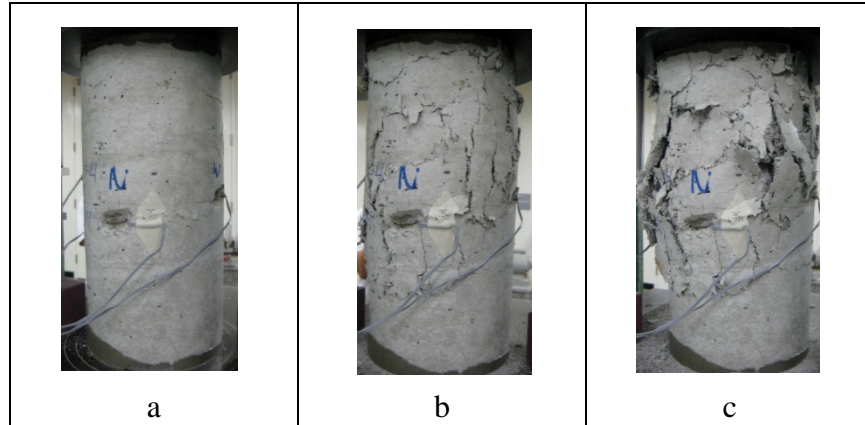
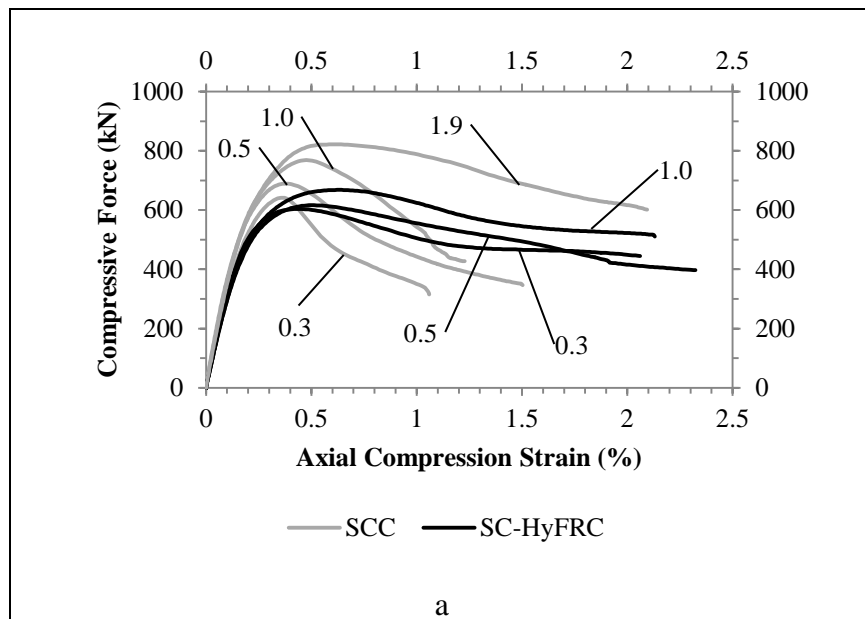


Figure 2-8 Damage Progression of 0.5 Percent Transversely Reinforced Concrete (top row) and SC-HyFRC (bottom row); at a) Peak Load, b) 3 Percent Strain, c) 5 Percent Strain

Comparing the load-strain response of the various reinforcing conditions in Figure 2-9a, it is immediately apparent that the performance of SCC in compression is strongly affected by the presence of transverse confining steel. Under increasing confinement the SCC composite is able to carry greater peak loads and sustain greater residual loads at strain levels beyond the crushing strain of unreinforced concrete. By 1.9 percent transverse reinforcing ratio, the ductility of the composite is greatly enhanced through a combination of confining the concrete core, nominally the area within the spiral diameter, and resisting the buckling of the longitudinal reinforcement. In contrast, the relative influence of spiral reinforcement is less impactful on the SC-HyFRC composite cylinders, with little differentiation noted between 0.3 and 0.5 percent and only a marginal improvement noted at 1 percent transverse reinforcing ratio. With spiral reinforcement being a form of passive confinement, the lack of damage in the SC-HyFRC specimens did not induce significant confining pressures that are responsible for increasing strength capacity. Unlike the SCC composite cylinders, ductile response was observed in all SC-HyFRC specimens regardless of transverse reinforcing ratio.



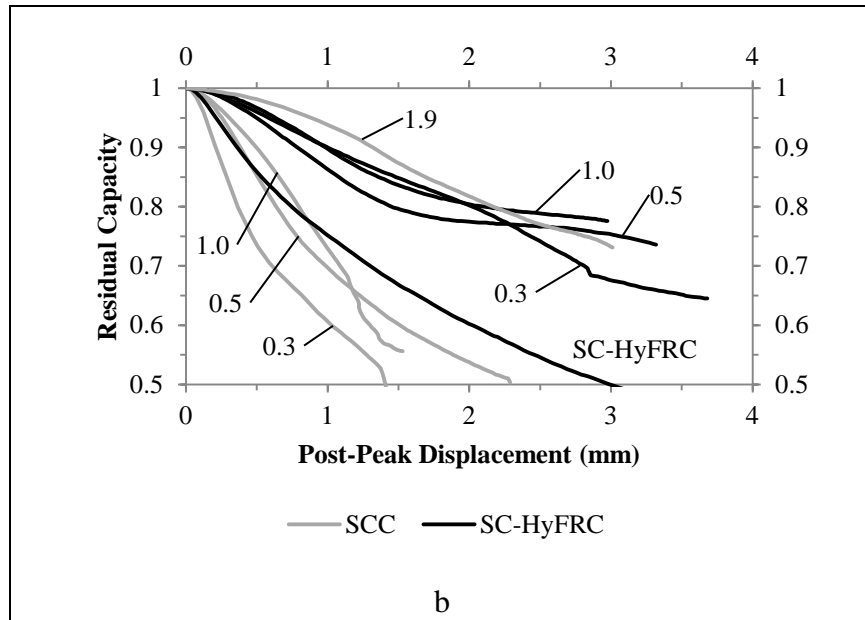


Figure 2-9 Comparison of Confinement Effects for SCC and SC-HyFRC Type Mixes; a) Compression Response, b) Residual Capacity Comparison

Normalization of the softening behavior (post-peak) of each of the specimen types was accomplished by comparing residual capacity, being the load divided by the specimens peak load, with displacement occurring beyond the peak (Figure 2-9b). By adding in the response of unreinforced SC-HyFRC cylinders having the same normalization, it is obvious that the given fiber reinforcement produces ductility on the same order as transverse reinforcing ratios of up to 1.0 in SCC composites. With the addition of any level of additional spiral steel reinforcement, 0.3 to 1.0 percent, the softening behavior of the SC-HyFRC is very similar to the most highly reinforced case of SCC, 1.9 percent.

In correlating the images of Figure 2-8 with the measured responses of Figure 2-9 valuable information can be inferred. Due to the lack of spiral fracturing and high residual strength at low reinforcing ratios exhibited by SC-HyFRC, it is likely that one mechanism of the internal confinement was a reduction in overall cylinder dilation accumulating beyond the peak load. By restraining the dilation of the core and cover through fiber reinforcement, the SC-HyFRC material imparts less bearing on the spiral reinforcement allowing it to better resist the onset of longitudinal bar buckling. Attempts to measure induced strain on the spiral at 4 discrete locations proved difficult due to the diagonal fracture plane developed in the SCC samples (see Figure 2-8, top right) in which some gages read large spikes in strain while others measured very little. Recorded strains from samples which resisted this strain “spiking” due to more uniform crushing are shown in Figure 2-10, with the transverse strains plotted versus the overall sample compression strain. As expected very little activity is measured in the steel spiral until approaching the peak compression load at which point microcracking induces dilation of the concrete core.

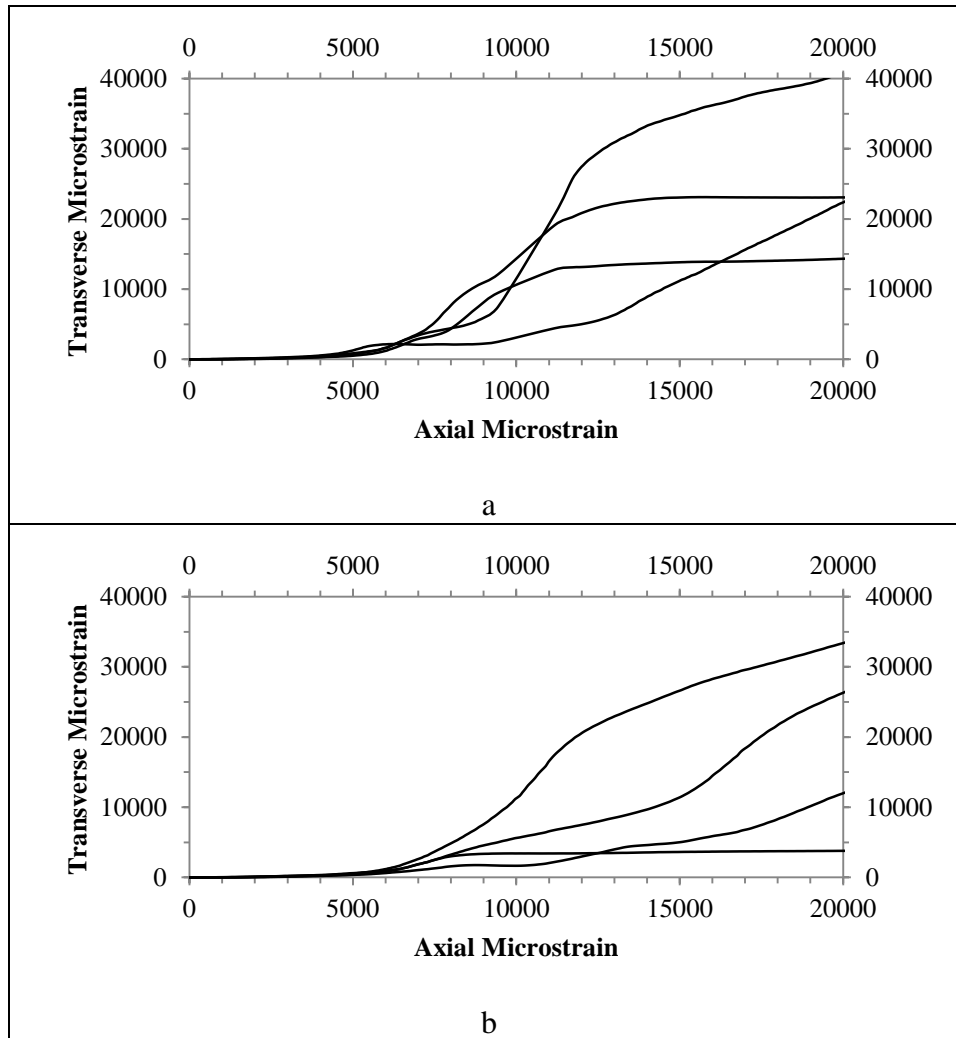


Figure 2-10 Comparison of Transverse Reinforcement Strain at 4 Discrete Points Along the Mid Height of 0.5 Percent Transversely Reinforced, a) SCC and b) SC-HyFRC, Cylinders

Predominantly, the strain gages affixed to the spiral reinforcement of SC-HyFRC samples showed less strain accumulation as would be expected based on the visual observation but it is important to preface such a result by the observation of crushing localization at large axial shortening occurring at a height above the location of the gages. Nevertheless, the overall response of the cylinders indicates that utilization of SC-HyFRC can contribute enough internal confinement to reduce the necessary transverse reinforcing ratio by a factor of 2 for samples of similar geometry, concrete compressive strength and layout while still sustaining an equivalent level of composite ductility.

2.5.2 Flexural Enhancement

Flexural samples fabricated with the reinforcing cages of Figure 2-2b, having been lightly hand vibrated to allow filling of the limited cover thickness with fiber reinforcement were tested in the same testing apparatus as the regular 4-point bending tests but with only a midspan application of load (3-point bending). Due to the significant amount of transverse reinforcement used for obstruction spacers in testing passing ability the beam failure mode was flexure

dominated. Comparative load-deflection curves are presented in Figure 2-11 with the response of a reinforced SCC sample used to gauge the impact of the fiber reinforcement.

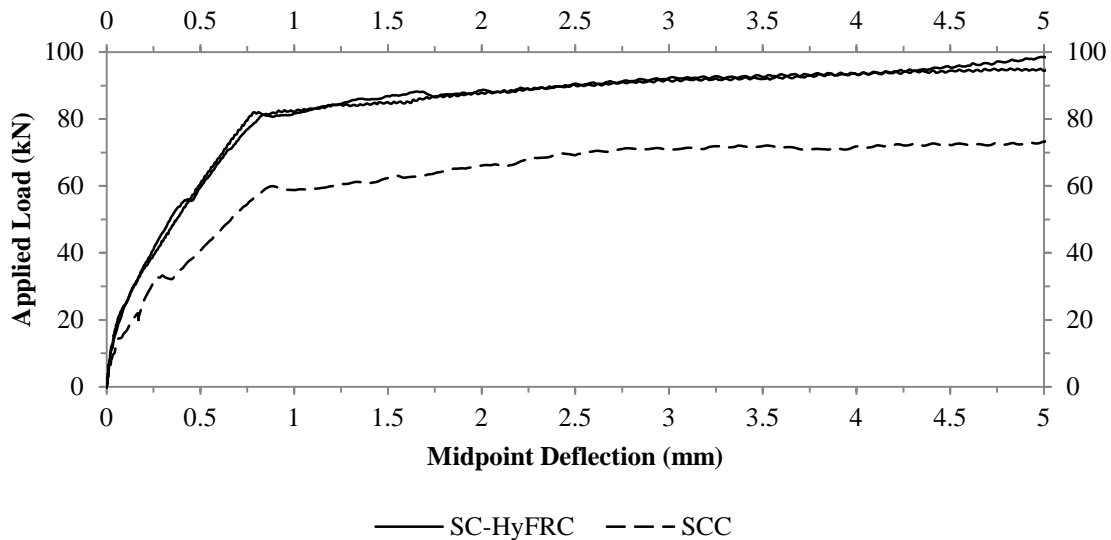


Figure 2-11 Composite Flexural Response of Reinforced SC-HyFRC Beams

As expected, the deflection hardening performance exhibited in Figure 2-6c allowed the SC-HyFRC samples to reach greater loads prior to crack initiation, as interpreted by the sharp non-linearity occurring in the SCC sample at 12 kN but restricted until 22 kN in the SC-HyFRC sample. Flexural stiffness, being the linearized response of the load deflection curve, offered by the cracked SCC sample, 54 kN/mm between 30 and 60 kN, was then dictated by the elastic stiffness of the reinforcing bars in the tension zone. In contrast, the flexural stiffness of the SC-HyFRC sample, being 77 kN/mm between 40 and 80 kN, illustrated the continued contribution of the fiber reinforced concrete in the tension zone. Even after yielding of the reinforcing bars in tension initiated (at midpoint deflections of about 0.85 mm), the relative contribution of the tension zone in fiber reinforced concrete remained and provided a significant strength enhancement to the composite, as indicated by the stable difference in load values existing between the SCC and SC-HyFRC curves at deflections between 1 and 5 mm.

2.5.3 Tension Stiffening

Having seen the tensile zone performance of the SC-HyFRC material in flexure, a more direct analysis of the tension stiffening effect of the material was investigated through direct composite tension testing. Specimens were fabricated in accordance with the designs of Moreno et al. (2014) in which prismatic sections of dimensions 127 mm by 127 mm by 1041 mm were cast around a central #5 reinforcing bar ($f_y = 430$ MPa, 1.2 percent longitudinal reinforcing ratio) mechanically coupled to threaded rods extending from either sample end (Figure 2-12). Localized strains induced in the reinforcing bar were measured by a distribution of strain gages attached along the central section of the bar at 75 mm on center. Composite elongation was measured by an extensometer, ostensibly similar to the compressometer configuration of Figure 2-7b but having a gage length of 813 mm and with the LVDTs configured to measured expansion. The region surrounding the threaded rod-coupler-reinforcing bar connections was

confined by three dimension steel wire cages to limit the damage imposed by stress concentration in the concrete and force specimen failure to occur in the instrumented region.

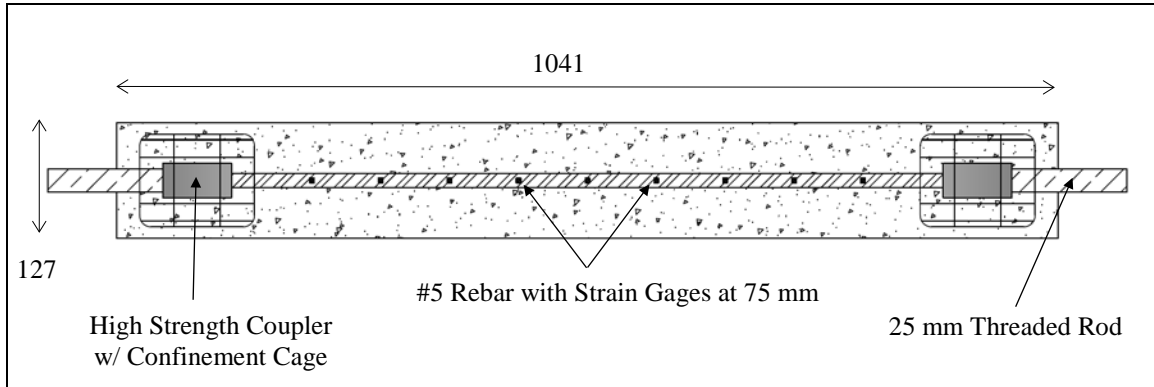


Figure 2-12 Tension Stiffening Specimens with Distributed Strain Gages, mm

Testing was conducted on a 245 kN MTS test frame with a displacement rate of 0.6 mm per minute of specimens fabricated with SC-HyFRC and a reference concrete having a similar compressive strength. The resulting load-composite elongation responses of both concrete materials in addition to the performance of a bare reinforcing bar with no concrete are shown in Figure 2-13. The initial performance of both concrete mixtures prior to cracking is evidence of the so-called tension-stiffening effect in which the elastic modulus of concrete contributes to the composite response being greater than the bare steel. Upon reaching the tensile capacity of the 127 mm square section of concrete, crack development in the reference samples quickly causes the composite performance to be characterized by the steel performance alone. In contrast, after the SC-HyFRC sample cracks at its tensile capacity, the composite response maintains the increased load capacity contributed by the fiber reinforced concrete. The overall difference experienced with respect to composite load and composite stiffness after cracking occur due to the SC-HyFRC material having a high residual strength in tension but lacking a significant hardening range (Figure 2-6b). The composite strength enhancement afforded by SC-HyFRC continues through the reinforcing bar yield strain, 0.23 percent, out past 5 percent specimen elongation. At 2 percent composite elongation the relative contribution of the SC-HyFRC starts to decrease due to the opening of cracks, with ductility then provided by strain hardening of the steel reinforcing bar.

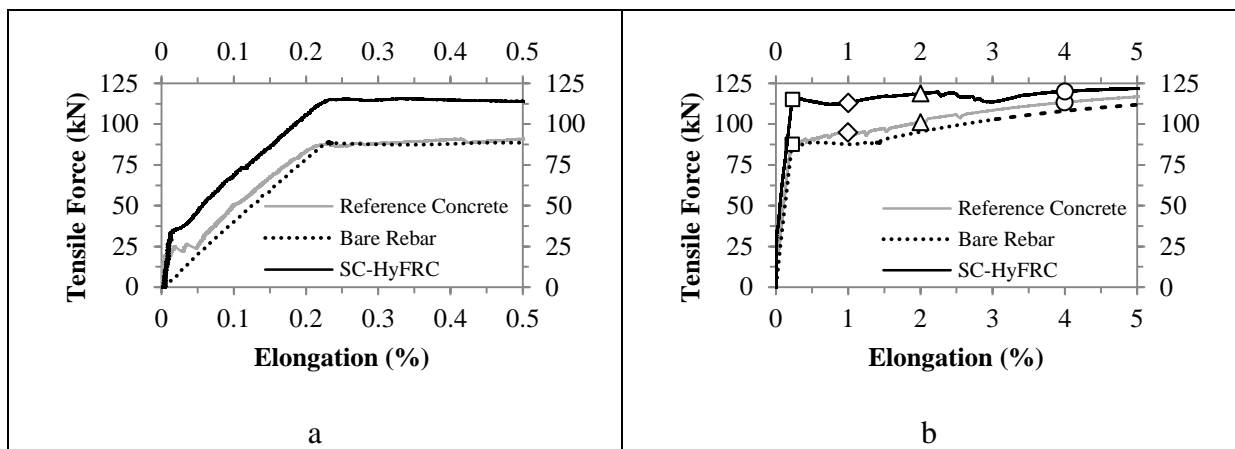


Figure 2-13 Tension Stiffening Response of SC-HyFRC Material; a) Initial Cracking Response, b) Yield and Strain Hardening Response, with Points Marked for Further Strain Distribution Analysis

Comparison of the distributed strain in the steel reinforcing bar is made at composite elongations of 0.23, 1, 2 and 4 percent denoted by markers in Figure 2-13b. Strain gage readings indicate that at the onset of yielding, no localization has occurred in either concrete or SC-HyFRC type samples with the cracking small enough that the fiber reinforcement can provide stable tensile resistance (see Figure 2-6b) generating the higher composite tensile load. At one percent sample elongation (Figure 2-14 and Figure 2-15), the presence of cracking is observed to force localization of strain to develop (gage strain being greater than composite elongation) at a primary location in the SC-HyFRC sample (highlighted by circling in Figure 2-14) and three locations in the concrete sample. At such a point, composite loads are able to increase due to strain hardening of the steel reinforcing bar.

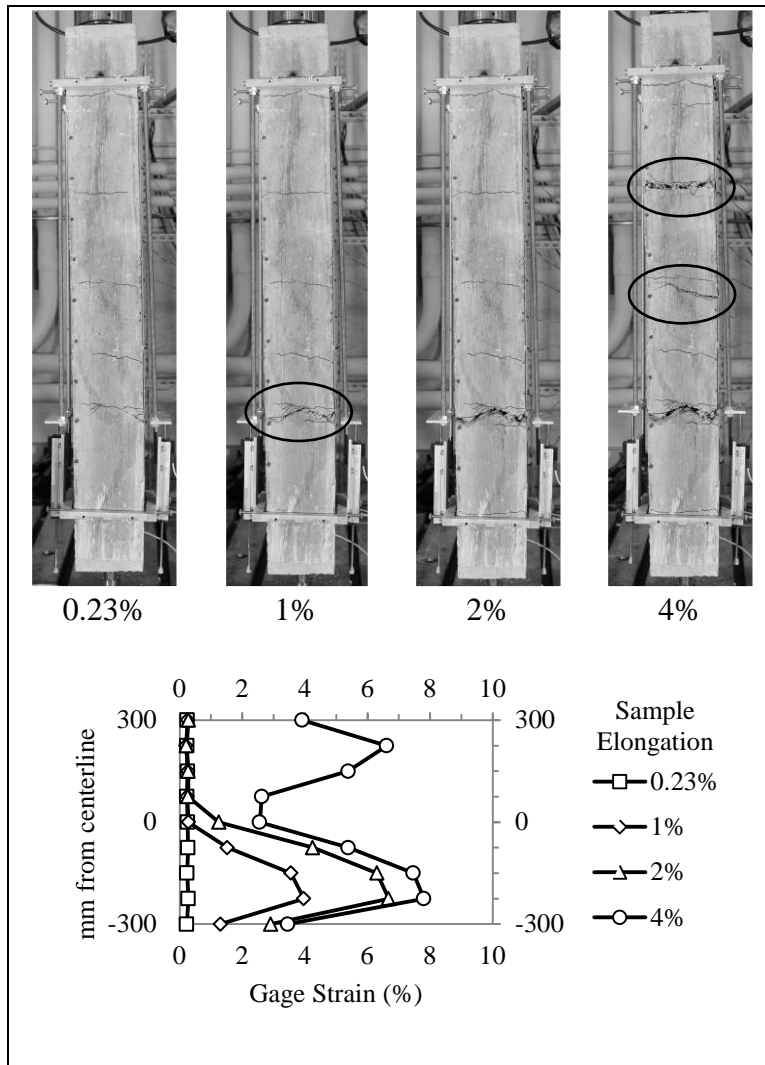


Figure 2-14 Strain Localization Effects as Measured by Strain Gages in Tension Composite of SC-HyFRC

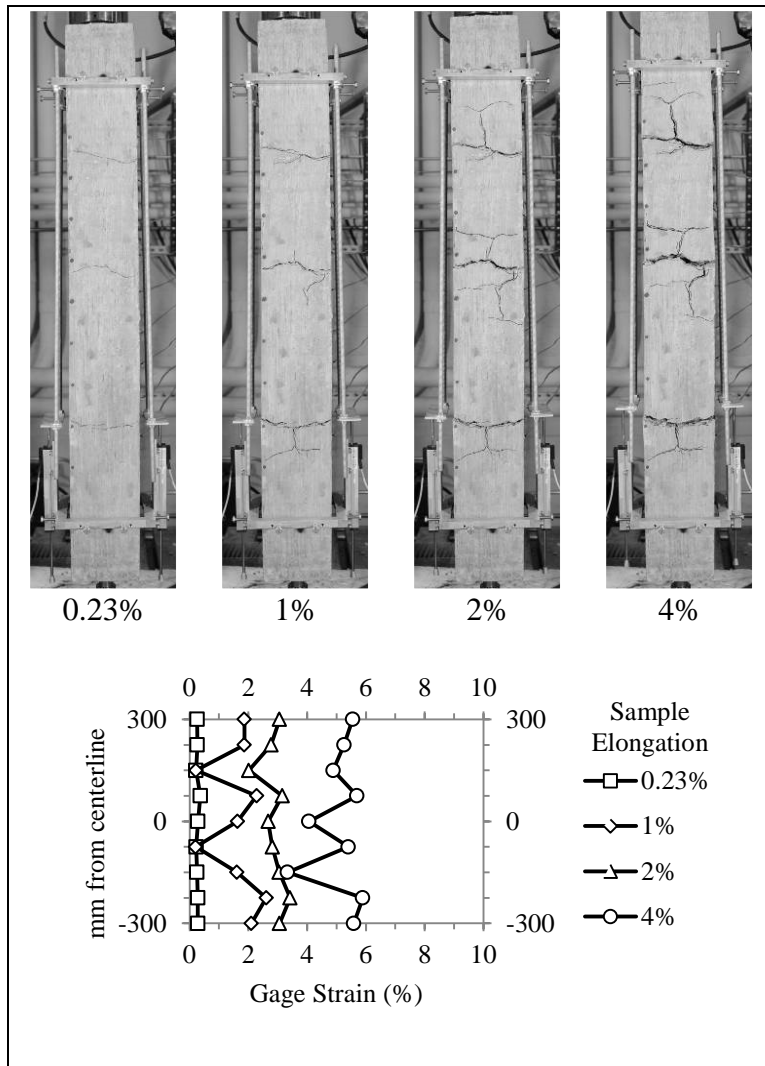


Figure 2-15 Strain Localization Effects as Measured by Strain Gages in Tension Samples

Under increasing displacement to 2 percent elongation, the suppression of splitting crack propagation in SC-HyFRC concrete limits the spreading of plasticity along a greater length of bar and is offset by further strain localization and steel strain hardening at the primary crack. Splitting crack growth is not limited in the concrete specimen, allowing for plasticity spreading and establishment of a more homogenous strain distribution. At high displacements corresponding to 4 percent elongation, the strain hardening in the primary crack of the SC-HyFRC sample forces growth of secondary cracks (highlighted by circling in Figure 2-14) but with a maximum localized strain of 8 percent. Contrastingly, due to the plasticity spreading in the concrete sample, the maximum local strain along the bar never exceeds 6 percent. Because of this delocalization brought about by the debonding action of splitting cracks, the concrete composites were able to reach an elongation of 10.3 percent before fracture of the bar took place. In the SC-HyFRC samples, the heterogeneous distribution of strain caused fracture of the bar at a composite elongation of 6.8 percent.

The results of direct tension testing of composite elements highlight the contribution of fiber reinforcement to overall tensile capacity with the effective increase strongly established up to a

composite elongation of 1 percent. Across the small cracks that occur within this range, the tensile response of the SC-HyFRC material is characterized by stable fiber bridging action crossing the transverse cracking and suppression of the splitting cracks that form in non-fiber reinforced concrete. As a consequence of the crack resistance of the SC-HyFRC material, plasticity is constrained to more localized section of the reinforcing bar, having an ultimate effect of reducing the composite elongation at fracture. Such an effect is not a ductility increase, but rather a ductility decrease and should be accounted for when designing with high performance fiber reinforced cementitious materials.

2.6 Extension to Bridge Column Testing

Taking into account the performance observed of the SC-HyFRC material in composite action, application to a structure which undergoes high levels of compression, flexure and tension is expected to highlight the obtainable performance enhancements of using high performance materials. One such structure type was determined to be bridge columns having a slender profile. Due to their slender nature, the stresses induced during lateral loading concentrate flexure at their rigid foundation connection. During seismic loading, this bending concentration is observed to cause cracking, spalling and crushing of concrete under moderate events, with larger magnitudes being responsible for reinforcement buckling and fracture. Based on the performance of SC-HyFRC during composite testing, it is expected that utilization can improve the lateral resistance of the column and limit the progression of damage until displacements in excess of those controlling the life safety criteria of conventional concrete columns.

Experimental application of SC-HyFRC was made to a column of geometry and reinforcing ratio in line with the prototype column described by Ketchum et al. (2004) being representative of typical California Department of Transportation designed elements. Design modifications consistent with the results of the aforementioned composite testing were made to maximize beneficial fiber contribution. These modifications included; 1) using a transverse reinforcing ratio of half the magnitude described by the prototype due to the intrinsic internal confinement of the material and to allow for larger clear spacing between adjacent spirals for fiber passing ability considerations and 2) debonding of the longitudinal reinforcing bars with rubber mastic tape and grease to spread plasticity over a bar length not constrained by fiber reinforcement suppression of splitting cracks. As a critical factor in bridge integrity during seismic events is the ability to sustain axial loads without suffering from degrading stiffness (P-delta effects), during testing the column integrity was judged on the basis of carrying an axial load equivalent to 10 percent of its capacity without displaying axial softening. Taking these considerations into account, the column reinforcement layout is shown in Figure 2-16, with the SC-HyFRC material being poured into the entire cross section above the foundation block height.

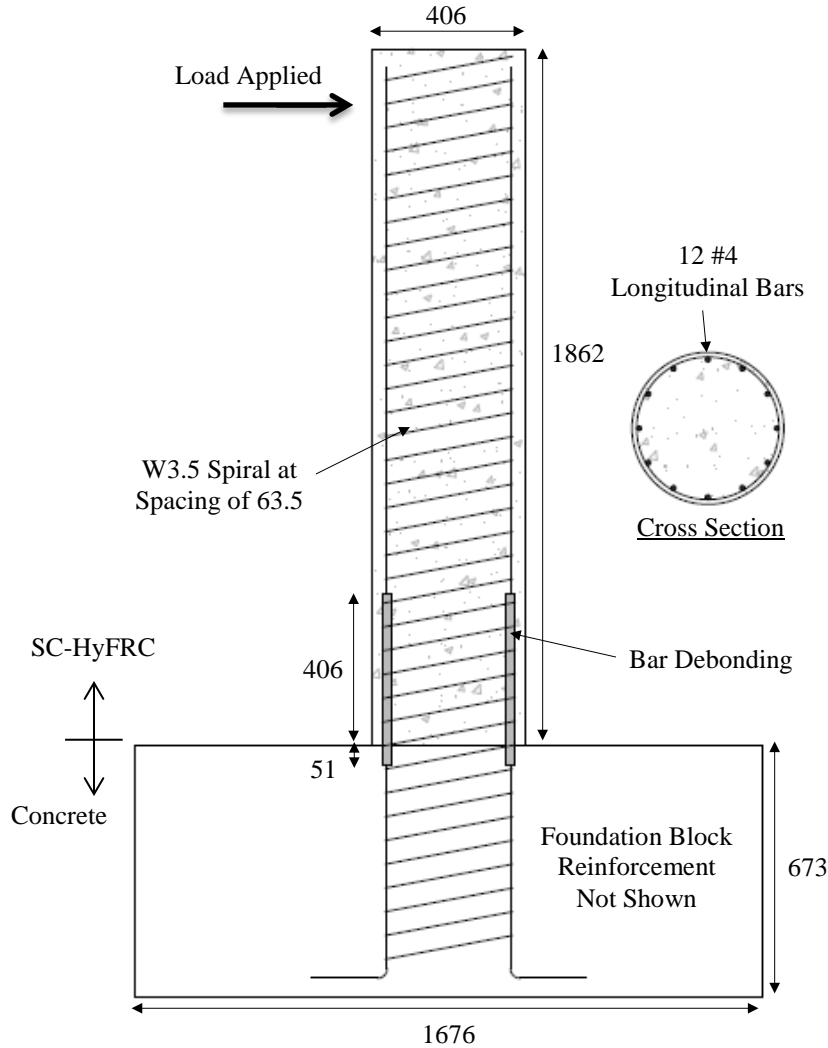


Figure 2-16 SC-HyFRC Column Detail, mm

Table 2-5 Drift Ratio Cycling Targets of SC-HyFRC Column

Low-Moderate Drift Ratio Demands (%)	0.15	0.30	0.45	0.60	1.2	1.8	2.4	3.6
No. of Cycles	3	3	3	3	3	3	3	3
Large Drift Ratio Demands (%)	4.2	4.8	6.0	7.1	8.3	9.5	11.3	
No. of Cycles	1	1	1	1	1	1	1	

Under step wise increasing cycles of lateral displacement to target drift ratios shown in Table 2-5, being the lateral displacement of the column head divided by the column height, the performance of SC-HyFRC matched well with the behavior exhibited under composite testing. Primarily, the spalling resistance noted in the internal confinement testing was similarly observed with the concrete gross area maintained beyond 3.6 percent drift (Figure 2-17a) at which point conventional concrete columns would be expected to have lost their concrete cover. Similarly, the intrinsic internal confinement of the fiber reinforced concrete did not rely on the available transverse reinforcement for confining stress, inducing expansive strains below the yield strain of the steel out to drift ratios of 6.0 percent (Figure 2-17b). While a single reinforcing bar fracture due to a construction defect occurred at a drift ratio of 6.0 percent, all other bars

remained intact until lateral displacements in excess of 8.5 percent drift. Overall integrity of the column was maintained until a drift ratio of 11 percent, a value well exceeding the maximum demands dictated by modern design codes.

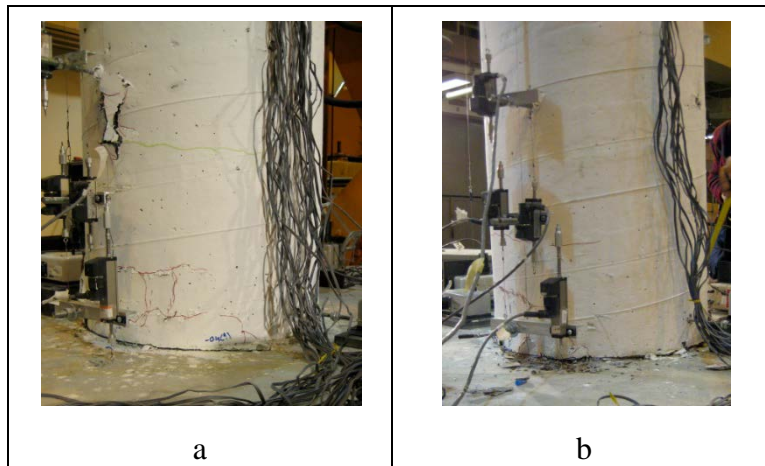


Figure 2-17 Column Base Damage at; a) 3.6 Percent Drift, b) 6.0 percent drift

2.7 Conclusions

Production of a self-consolidating hybrid fiber reinforced concrete has been carried out for the first time in successfully producing a deflection hardening composite. Identification and optimization of the relevant criteria was carried out in a parametric study to integrate the ductility enhancing fiber reinforcement with workability enhancing flow behavior. The finalized composite can be fabricated using conventional construction methods and placed without significant consideration to the labor intensive process of compaction. The only caveat being that highly congested reinforcing cages with tight transverse reinforcement must take into consideration the maximum fiber size for determining fiber passability restrictions. While imposing limits on rebar spacing might normally be problematic for conventional concrete placed under significant loading, experimental testing reveals that SC-HyFRC can generate equivalent element response at reduced transverse reinforcing ratios, attributed to an internal confinement mechanism.

Though crack resistance has been heretofore a desirable component not normally associated with conventional concrete, the experimental testing of tension stiffening has highlighted a scenario in which cracking resistance must be manipulated in order to ensure ductility. The conflicting nature of cracking resistance producing a decrease in ductility is brought about by the conventional level of ductility being associated with a breakdown in composite action. Because the addition of fiber reinforcement can sustain composite behavior between reinforcing steel and concrete in tension to a greater extent, the overall composite behaves much more as a combination of the two individual materials rather than being solely dominated by one. The early fracture process, being only noticeable at significant levels of displacement demand, can be mitigated by controlling the relative ratio of tension contributions of the concrete component with the tension contribution of the steel component. Testing has revealed that at low longitudinal reinforcing ratios the fiber reinforced tension contribution forces more significant localization of strain to occur in the location of primary cracking. By understanding that the reinforcing steel must have sufficient tensile strain hardening to overcome the summation of steel yield load and fiber reinforced concrete capacity, elements can be designed to ensure the

formation of secondary cracking and redistribution of steel plasticity necessary to meet ductility criteria.

The application of SC-HyFRC to a concrete bridge column based on a typical California design illustrates the ductility enhancing and damage resistant behavior of the high performance material. Further investigations into the use of SC-HyFRC and close derivatives, targeting specific regions of the column geometry such as a) the column base traditionally known as the plastic hinge region in which the forces are highest (Trono et al. 2013) or b) the column perimeter in which the induced strains are highest (Nyugen et al. 2014) have been undertaken with likewise similar results regarding the ductility enhancing nature of SC-HyFRC. In doing so the high performance material can be targeted to the region in which it is most impactful and minimize the overall cost impact relative to conventional construction methods.

In all of the cases of mechanical loading that have been under investigation in this chapter, the inclusion of hybrid fiber reinforced concrete in a self-consolidating matrix is shown to produce noticeable reductions in damage versus conventional type concrete mixes owing to the crack resistance of the fiber composite. While this chapter has focused on the parameter of ductility as an evaluation tool, the exhibited damage resistance is also relevant to durability. By limiting the damage associated with mechanical loading it is important to realize that the soundness of concrete can be preserved, thus limiting the detrimental effects upon concrete permeability associated with cracking. A specific scenario of such an interaction will be presented later, in order to tie together the aspects of ductility and durability in a high performance material.

3 Corrosion Damage Resistance

3.1 Introduction

Corrosion, like many durability phenomena in which the soundness of concrete is degraded, can be traced back to the generation of an expansive product. While concrete itself is not directly susceptible to electrochemical corrosion, the reinforcing steel bars required in order to provide tensile strength/resistance necessary to meeting structural ductility demands are. Corrosion of steel in concrete is an electrochemical process whereby iron (Fe) is oxidized from the steel reinforcing bar at the anode location and typically oxygen is reduced at the cathode location. In conventional reinforced concrete, corrosion activity is protected against by the alkaline pore solution ($\text{pH} > 12.5$), maintained due to the availability of alkali ions present in portland cement (Broomfield 2006). Under such conditions the formation of a passivation film on the surface of steel is stabilized, which in turn limits the red-ox reaction to an inconsequential rate.

Two conditions to which concrete can be typically exposed, carbonation and chloride penetration, have been found to be sufficient to depassivate the steel reinforcement and initiate significant corrosion activity. However, both during prolonged exposure to external sources of carbon dioxide or chlorides, the carbonation front/chloride ions still must penetrate the layer of concrete between the surface and the depth of the reinforcing bar, generally known as a cover thickness and acting as the primary protection provided against corrosion by building codes (ACI Committee 222 2001). The length of time from which the carbonation or chloride penetration takes to reach the depth of steel reinforcement is known as the “initiation” time and is most directly influenced by the thickness of the cover layer and the quality of concrete in said cover layer. Under an idealized scenario, this initiation time would be not less than the service life expectancy of the reinforced concrete structure. An inspection of the existing bridge inventory suffering from corrosion damage would illuminate the danger of assuming that cover thickness can suitably fill the role of an acceptable corrosion deterrent. One of the primary reasons for which cover concrete thickness cannot alone be a deterrent is the presumption of sound concrete unexposed to other loading scenarios, such as restrained drying shrinkage, service loading or more extreme cases of loading such as seismic loading. Under such alternative loadings, the cover concrete is often the most highly strained region of the concrete cross section and is therefore the most prone to cracking. Even when the crack openings formed under these scenarios is restricted to the microscale (100 – 200 μm) research has shown that the ingress of water and ions is uninhibited (Wang et al. 1997, Reinhardt and Jooss 2003). It follows that to extend the period of “initiation time”, which is desirable as it is characterized by the occurrence of negligible corrosion activity, an effort must be made to improve the properties of the cover concrete both from the perspective of reducing permeability and by increasing cracking resistance.

At the point in time in which the bar becomes depassivated, the “propagation” phase of corrosion damage begins. The propagation phase is characterized by the corrosion rate and the extent of damage caused by iron-oxide corrosion products. While there is not a single iron-oxide (FeO , Fe_2O_3 , etc.) species that forms in all cases of corrosion, all species that have been identified do exhibit a volumetric increase relative to their original state of iron (Mehta and Monteiro 2013). This proves problematic in the case of reinforced concrete due to the confined environment in which reinforcing bars are placed, such that the expansive pressure brought about during corrosion is often only relievable by cracks forming in the concrete. Through these cracks the rust products are typically transported to the surface of the concrete and provide a color indicator of corrosion activity to an inspector that corrosion damage is ongoing. From a

structural safety standpoint, bar mass loss is perhaps the most critical factor however it is important to acknowledge that the corrosion rate during the propagation phase is still a function of reactant (O_2) availability at the cathode location. Thus the role of cracking with respect to crack opening and the extent to which corrosion induced cracks propagate, both of which directly affect the transport of oxygen through the concrete environment, can be used to extend the time prior to reaching an unacceptable damage state signifying the end of the propagation phase.

As the suggested service life of a reinforced concrete structure with respect to corrosion is defined by Tutti (1982) as the sum of the aforementioned initiation and propagation periods (Figure 3-1), a means of providing a crack resistance mechanism through which both phases can be extended is highly desirable.

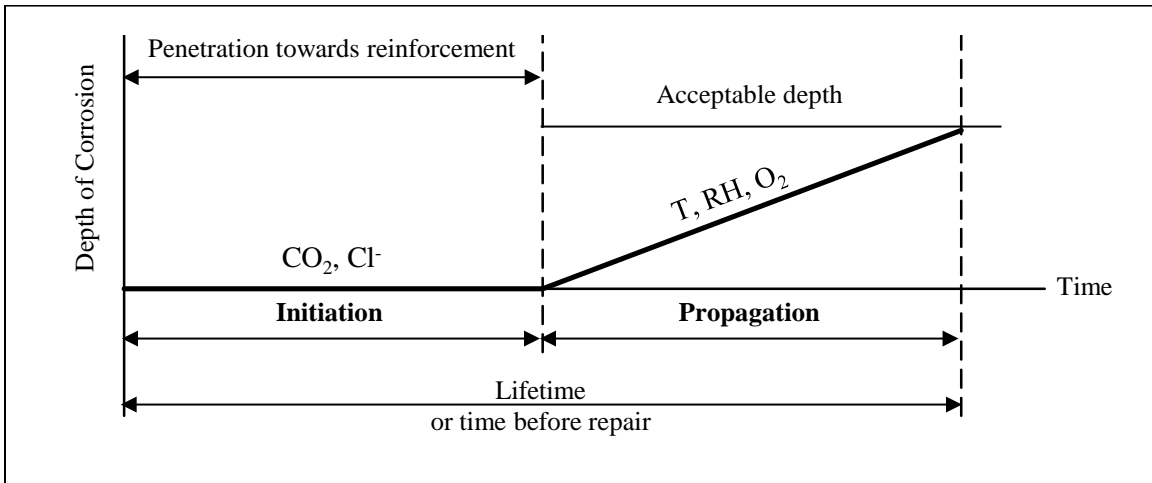


Figure 3-1 Schematic of Steel Corrosion Sequence in Concrete (after Tuutti 1982)

With the addition of crack resistant characteristics in the cover concrete, it can be expected that the initiation duration (defined by CO_2 and Cl^- penetration towards steel reinforcement) may be lengthened by preventing crack formation otherwise caused by drying shrinkage, freeze-thaw damage or other forms of deleterious service loading.

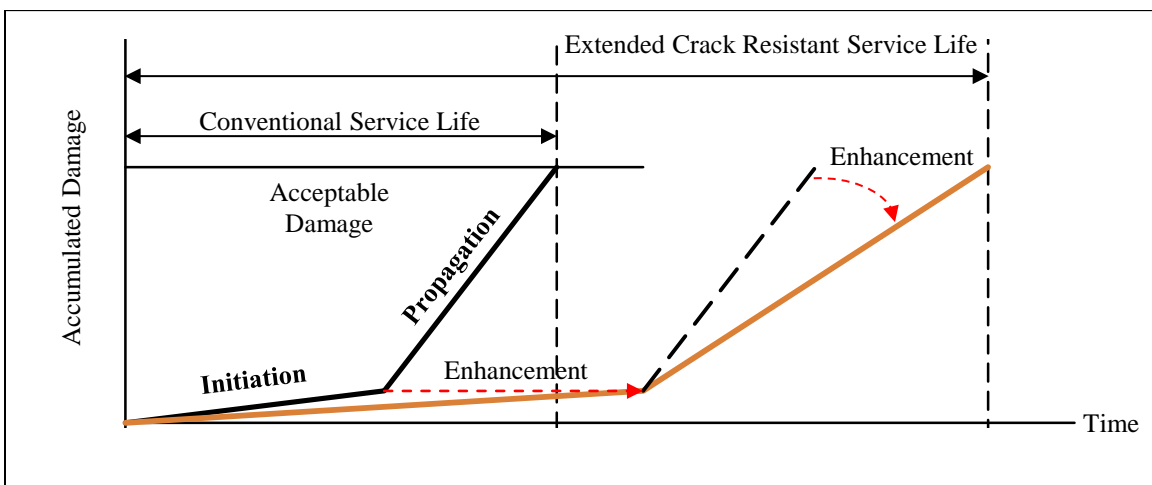


Figure 3-2 Modified Crack Resistant Damage Schematic of Corrosion Sequence

With lifespan displayed as the time to reach a specified damage state in Figure 3-2 rather than corrosion depth as in Tuutti's schematic and also inclusive of other forms of typical concrete exposure such as drying shrinkage and service loading (Samaha and Hover 1992), this extension in the initiation phase is sketched to show that a substantial improvement can be gained through maintenance of a sound layer of cover concrete. The total service life of an element having enhanced crack resistance is further shown to benefit from an increased propagation phase duration, possible because of a correlation between cracking resistance and reduced corrosion rates. Both the initiation and propagation phase duration extensions are dependent upon the local environments into which concrete is placed, but are similarly beholden to the effectiveness of the crack resistance mechanism. In this respect, within the field of fiber reinforcement, those composites capable of producing strain/deflection-hardening response are capable of producing crack restraint which translates to continuous lowering of damage accumulation rates.

The research objective of the projects described herein is to experimentally validate that fiber reinforcement, specifically the self-consolidating hybrid fiber reinforced concrete mix, is capable of meeting the cracking demands posed not only by the micro and macroscale drying shrinkage and service loading placed upon concrete elements but also the corrosion induced internal expansion imposed at the microscale. These results are then compiled to illustrate the potential for service life extension achievable by hybrid fiber reinforcement against the deleterious action of reinforcement corrosion.

3.2 Background

Corrosion damage is the most financially impactful form of environmental deterioration occurring within the existing inventory of reinforced concrete infrastructure, yet the knowledge that corrosion damage is expensive is not a new notion. Past estimates of damage in the nation's reinforced concrete inventory place the fiscal burden at 20 billion dollars in 1992 with the total increasing at a rate of 500 million per year (Cady and Gannon 1993). In a more recent full inventory survey conducted by the U.S. Federal Highway Administration (Koch et al. 2001), 15 percent of all highway bridges (of which 343,000 were reinforced and prestressed concrete bridges out of a total stock of 583,000 total bridges) were found to be suffering from corrosion damage equating to repair and maintenance costs of 8.3 billion dollars annually. This level of deficiency has provided a strong financial incentive to fund reinforced concrete corrosion research geared towards preventive and rehabilitative schemes with the goal of making structures durable enough to meet their designed-for service lifespans.

A great deal of research has been devoted to identifying the role of concrete cracking with respect to overall element response during corrosion attacks. It has been well established that concrete cracking influences not only the permeability of concrete cover to carbon dioxide or chloride ions during the initiation phase but also to determining the magnitude of sustainable corrosion rates occurring during the propagation phase. In the context of the damage schematic presented in Figure 3-2, cracked concrete can be thought to essentially eliminate the initiation phase duration while also steepening the accumulated damage curve of the propagation phase which in totality produces an abbreviated life expectancy (not shown).

In addressing the initiation phase, many researchers (Sahmaran and Yaman 2008, Djerbi et al. 2008, Malherio et al. 2011, Halmen and Trejo 2012) have identified the quality of cover concrete as being critical to the diffusivity of chloride ions and carbon dioxide. Universally, the concrete porosity, dictated by the concrete quality, is observed to have an inverse relationship with the diffusion coefficient of chloride migration. Such a relationship is consistent with well-

made, strong concrete being a superior protector than poorly-constructed, weak concrete. The differentiation is exacerbated by the presence of cracking; in some such cases the protection afforded by high quality concrete can be reduced beyond even the performance of low quality concrete. Wang et al. (1997) determined that a strong dependency existed between water permeability and crack openings of a specific size; the permeability difference between cracks smaller than 50 μm being minimal; the permeability difference between cracks of 50 μm and 180 μm being orders of magnitude apart; and the permeability difference between cracks of 200 μm and 400 μm being far less severe.

Specific to structural deterioration during the propagation phase, Gonzalez et al. (1995) have reported reinforcement diameter loss occurring at a rate 10 times greater in concrete when reinforcing steel has direct exposure to marine conditions through a surface crack versus uncracked concrete placed in the same conditions. For reinforcing bars having a nominal diameter of 8 mm, the impact of pitting corrosion extending to a maximum depth of 1.2 mm could be responsible for a capacity loss of up to 50 percent. Similar correlations between reinforcing bar mass loss and cover concrete cracking have also been reported by other researchers (Vidal, Castel and Francois 2004, Jaffer and Hansson 2008) with Sahmaran and Yaman (2008) observing that crack widths greater than 150 μm specifically showed evidence of corrosion activity significantly greater than in control samples having no cracking while those samples having crack widths less than 100 μm behaved largely similar. However, some research (Schiessl and Raupach 1997, Francois and Arliguie 1999) does not exhibit correlation between increasing crack openings, 200/300 μm versus 500 μm , and associated corrosion current and mass loss. In such cases it is likely that the difference is attributable to a critical crack dimension. Explained by the work of Wang et al. (1997), water diffusion and with it reactant availability, exhibits less dependency on crack dimension for those cracks greater than 200 μm . Those cracks larger than this critical crack dimension in essence behave approximately similar and are capable of sustaining high corrosion activity. Though not specifically addressed when cracks are prefabricated by removable inserts placed in the concrete during casting, the concept of all cracks larger than a critical crack size behaving identically is belied by field experimentation (Andrade et al. 1990, Poupard et al. 2006) in which maximal corrosion rates are achieved in progressively larger cracks. This leads to the interpretation that corrosion current density can have a limited dependency on crack size so long as the overall bond is kept largely intact providing continuous protection to areas not in the immediate vicinity of the crack as is the case with pre-inserted cracks. In natural conditions, where the bar anodic area is less distinctly defined by the crack width, larger crack sizes likely imply significantly greater anodic areas caused by bond breakdown along the bar surface emanating from the crack location and thus are capable of producing larger current.

Drawing from the experimental evidence of cracked conventional concrete research, several niches can be highlighted in which fiber reinforced concrete can be beneficial to overall corrosion resistance. During the initiation phase, the potential to have an allowable state of microcracking ($\leq 100 \mu\text{m}$) while not suffering a significant detriment in concrete permeability makes fiber reinforced concrete a candidate for many types of durability studies. Extending the potential benefit into the propagation phase, Schiessl and Raupach (1997) isolated the contribution of cathodic areas in limiting anodic current which could be developed in proximity to the cracked region. By varying the spacing between 500 μm wide cracks to 10 mm, 20 mm and 100 mm, the anodic currents were measured to be 27.7 μA , 50.5 μA and 113 μA . The implications of such results, having less concentrated bar deterioration occur in combination with

a multiple cracking scenario because of a lack of cathode area to balance the anode reaction, lends itself to fiber reinforced composites which are better capable of preventing macrocrack development and localization during flexural/tension loading.

Various forms of fiber reinforcement have been tested experimentally to meet such durability goals. Corrosion initiation, measured indirectly by water permeability has been shown by various researchers (Rapoport et al. 2002, Lawler et al. 2002, Lepech and Li 2009) to present competing performance behaviors with the addition of steel fiber and polymeric fibers. Rapoport reports an increase in composite permeability versus conventional concrete for cracks smaller than 100 μm owing to an overall increase in porosity and interface surfaces accompanying the inclusion of fibers in the concrete matrix. In contrast, for identical crack openings ($\geq 100 \mu\text{m}$), a comparison feature which Lepech disputes as unrealistic of actual load-deflection behavior of high performance fiber reinforced concrete in which crack size is better controlled, the inclusion of fibers results in a reduction of the coefficient of permeability by one to two orders of magnitude. With respect to the competing nature of these permeability changes, it should be noted that the relative increase and subsequent impact of porosity in uncracked or minimally cracked concrete is inconsequential in comparison to the magnitude of permeability increase occurring during moderate cracking, thus the net benefit of fiber reinforcement far outweighs the potential negatives if nearly any level of cracking will occur over the service life of the structure. Within the propagation phase, fiber reinforcement is also observed to both indirectly, by controlling mechanically induced cracking (Miyazato and Hiraishi 2005, Blunt 2008, Kobayashi et al. 2010) in advance of corrosion, and directly, by controlling corrosion induced cracking (Grubb et al. 2007, Sahmaran et al. 2008), restrict the magnitude of corrosion damage that can be developed. While the research works of Miyazato and Hiraishi (2005), Blunt (2008), and Kobayashi et al. (2010) confirmed the behaviors noted regarding fiber reinforcement effects upon permeability, they continued on to directly measure the effect of said permeability changes on the propagation response of reinforcing steel bars. In all cases, even after chlorides reached the depth of steel reinforcing bars, the corrosion damage was mitigated to be inconsequential with respect to bar diameter loss influencing composite performance criteria in contrast to equivalently loaded or cracked conventional concrete suffering deterioration of said performance criteria. Focusing only on the fiber influence of the corrosion damage propagation phase, Grubb et al. (2007) and Sahmaran et al. (2008) identified resistance to corrosion induced cracking at the steel to concrete interface as being critical to conserving reduced rates of corrosion current density which translates to reduction in the propagation slope as shown in Figure 3-2. Even with the formation of corrosion splitting cracks, Sahmaran et al. (2008) proved the value of crack width limitation by fiber reinforcement (0.1 mm versus 2 mm for conventional mortar) being a necessary requirement of maintaining a partially effective layer of cover concrete.

Briefly, it is also worth addressing the counterintuitive nature of utilizing steel fibers in conditions that would be otherwise corrosive to steel reinforcing bars. General, commercial-use steel fiber reinforcement is produced with low-carbon steel, such that unincorporated fibers exposed to moisture will quickly show evidence of rust. When placed in concrete, the fibers are protected by the same alkaline environment that stabilizes the passivation layer on conventional steel reinforcing bars. However, in the presence of identical chloride contaminated concrete conditions the fibers remain passive while steel reinforcing bars undergo corrosion. Many researchers (Mangat and Gurusamy 1988, Kosa and Naaman 1990, Granju and Balouch 2005, Balouch et al. 2010) have investigated the conditions necessary for corrosion of steel fibers in concrete and the potential deterioration that they may impart on composite performance. A

consensus is reached that only those steel fibers located within millimeters of an exposed surface, being either the original concrete surface or a crack face, are susceptible to corroding. Suggested reasoning for the predominant passivity of embedded steel fibers in chloride contaminated concrete includes chemical and geometric considerations; Mangat and Gurusamy (1988) propose the passivity is caused by a high surface concentration of calcium hydroxide in conjunction with limited potential cathode area to balance any anodic reaction; Granju and Balouch (2005) argue that the fiber to cement matrix bond achievable with small diameter fibers is substantially less porous than for conventional reinforcement and it is therefore more difficult for chloride ions to penetrate. Corroded composite performance as tested by Granju and Balouch (2005) and Kosa and Naaman (1990) determined that salt water induced corrosion of fibers bridging a mechanically induced crack face suffered from distinct differences relative to degree or fiber corrosion. For “lightly” corroded fibers, Granju and Balouch (2005) reported an increased composite toughness due to bond toughening. For corroded fibers having lost up to 10 percent of their diameter, Kosa and Naaman (1990) reported decaying composite toughness consistent with the duration of corrosion attack due to fibers fracturing prior to pull-out. Given enough time, it should be expected that exposed fibers will behave in a manner similar to Kosa and Naaman (1990) results and in order to maintain composite performance criteria, sufficient fiber reinforcement must be available within the region not yet encompassed by cracks.

Lastly, due to the constraints of researching a slow acting process within a limited timeframe, many researchers have investigated accelerated test protocols designed to achieving a representative corrosion damage state in a shortened period to time. Within reinforced concrete this has involved the use of applied currents in excess of the naturally occurring corrosion current to drive oxidation of the reinforcing steel (Gonzalez et al. 1995, El Maaddawy and Soudki 2003, Austin et al. 2004, Care and Raharinaivo 2007). Reported current densities employed in this technique have ranged from $100 \mu\text{A}/\text{cm}^2$ to $10 \text{mA}/\text{cm}^2$, relative to reported field exposure corrosion current densities being capped in the region of $100 \mu\text{A}/\text{cm}^2$. Summary conclusions by El Maaddawy and Soudki (2003) suggest current densities at the lower end of the above listed range are more applicable to generating behavior representative of field exposure while Care and Raharinaivo (2007) find that current densities in the range of 100 to $500 \mu\text{A}/\text{cm}^2$ produce appropriately scaled levels of damage. Utilizing accelerated testing has the added benefits of producing corrosion induced cracking in a rapid manner and allowing for subsequent investigation of cracking propensity and permeability of the surrounding concrete matrix. Such an approach is expected to provide a method for identifying the in-situ role of fiber reinforcement in responding to corrosion induced expansion stresses.

3.3 Test Methods

3.3.1 Electrochemical Test Methods

Testing corrosion activity (corrosion rate) of steel reinforcement embedded with concrete directly can vary from being simple and standardized, as in the case of half-cell potential mapping (ASTM C876 2009) or macrocell “galvanic” corrosion (ASTM G109 2013), to being significantly more difficult and requiring a greater understanding of electrochemical processes as in the case of microcell corrosion. For the purposes of the experiments conducted as a part of this project, all electrochemical (corrosion) measurements were taken using a Gamry Instruments G750 potentiostat. The potentiostat is a piece of equipment that allows the user to manipulate either current or potential (voltage) and monitor the corresponding effect on the other. The potentiostat utilized throughout this testing regime has the added benefit of having an IR

compensation function which compensates for the voltage drop caused by the semi conductive medium (saturated concrete) and a zero-resistance ammeter (ZRA) capability, which allows the user to directly record the current flow between two electrodes having different independent corrosion potentials. For macrocell “galvanic” corrosion, simplified to be the case in which the anode and cathode exist on separate reinforcing bars in regions of high and low chloride content respectively, the ZRA measurements are used to determine the steady-state current flow between the anodic bar (working electrode) and cathodic bar (counter electrode) (see Figure 3-3). Under such conditions, the relative areas of the working and counter electrodes and the corrosion potential of each electrode independently are important factors in determining the overall magnitude of current that is developed. For all of the macrocell “galvanic” corrosion specimens tested in this project, the ratio of the counter electrode bar area to working electrode bar area is 2, though it is a fair assumption that the actual anode area is less than the entire working electrode bar surface area for those samples in which localized cracking was implemented.

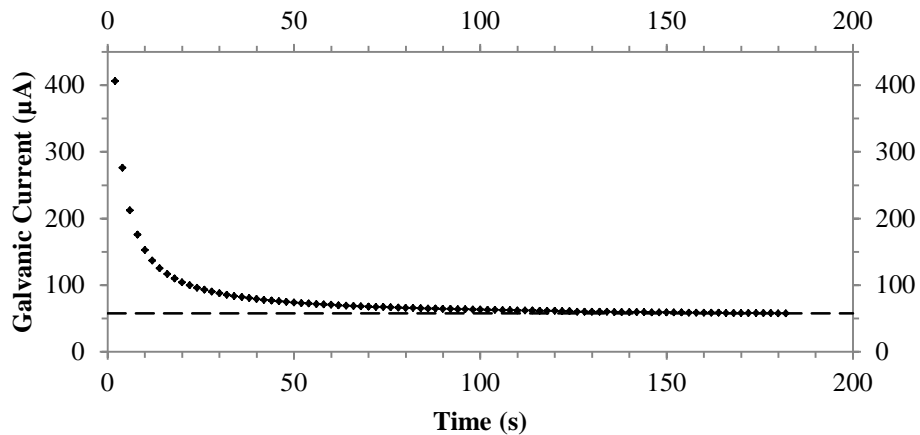


Figure 3-3 Typical Galvanic Corrosion Test Performance

To conduct microcell corrosion measurements, for the case in which the anode and cathode sites are located adjacently along a single embedded reinforcing bar, the ZRA capability cannot be used because the two reaction sites are already electrically connected. In such a condition, the potentiostat only allows the user to measure net current which is problematic since the corrosion potential (E_{corr}) of the single bar setup is defined as the potential at which anodic current and cathodic current are equivalent thus producing zero net current. To measure microcell corrosion the potential must be manipulated away from E_{corr} with the resulting changes in current recorded. Manipulation of the Butler-Volmer equation (Equation 1), in which the current is determined by the exchange current I_0 , the charge transfer coefficients α_a and α_c , the ion valency n , the rate constant k_B and temperature T , suggests that different ranges of potential change versus E_{corr} (overpotential, η) highlight different useful characteristics of the electrochemical cell.

$$I = I_0 * [e^{\alpha_a n e \eta / k_B T} - e^{-(1-\alpha_c) n e \eta / k_B T}]$$

Equation 1

Small perturbations in potential (+/- 10 millivolts (mV) vs. E_{corr}) are useful due to the linearized nature of the hyperbolic relationship exhibited by current and overpotential very near the

corrosion potential (Equation 2). In such a range where $V \sim IR$, the polarization resistance (R_p) of the bar surface can be extrapolated as the tangential slope at zero current (ASTM G59 2009).

$$I \sim I_0 \frac{(\alpha_a + 1 - \alpha_c)ne}{k_B T} \eta, \quad \eta \ll \frac{k_B T}{ne}$$

Equation 2

Using larger magnitude overpotential sweeps (± 75 mV vs. E_{corr}), the net current becomes dominated by the anodic current at positive overpotentials and the cathodic current at negative overpotentials (Equation 3).

$$I \sim \left\{ \begin{array}{ll} I_0 e^{\alpha_a ne \eta / k_B T}, & \eta \gg \frac{k_B T}{ne} \\ -I_0 e^{-(1-\alpha_c) ne \eta / k_B T}, & \eta \ll -\frac{k_B T}{ne} \end{array} \right\}$$

Equation 3

From these anodic and cathodic dominated regions, Stern and Geary (1957) suggested extracting Tafel slope values, β_a and β_c , from a log scale graph of current which can be manipulated into a value, B , characterizing the potential at which R_p and corrosion current (I_{corr}) are correlated (Equation 4).

$$B = \frac{\beta_a * \beta_c}{2.303 * (\beta_a + \beta_c)}$$

Equation 4

Specific to the experiments conducted within this investigation a complete suite of measurements follows a four step procedure; first, the corrosion potential of the anodic bar is monitored for steady-state behavior to ensure that the sample is stable (Figure 3-4); second, the polarization resistance test is conducted using a ± 10 mV sweep with the potentiostat applying current in order to achieve a controlled value of potential (Figure 3-5); third, a second corrosion potential test is conducted to ensure that the polarization occurring during the prior test did not alter the sample stability; and fourth, a tafel scan is conducted by polarizing the bar ± 75 mV, again with the potentiostat applying the current necessary to achieve the demanded potential (Figure 3-6). In order to minimize the probability of the large polarization applied during the tafel scan from changing the steady-state corrosion potential of the bar, for most experiments a subset of samples are designated only for corrosion potential and polarization resistance measurements (step 1 and 2). Reported results of polarization resistance are typically based on an average value of only this subset. While the data plotted in Figure 3-5 and Figure 3-6 are of separate samples, it is also worth noting that the anticipated exponential curvature is well represented within the tafel scan whereas the linearity of the most positive range (± 10 mV vs. E_{corr}) of the polarization resistance curve is mildly surprising. Such behavior is attributed to the relative numerical contributions of the anodic and cathodic reaction constants rather than an intrinsic ohmic resistance within the sample.

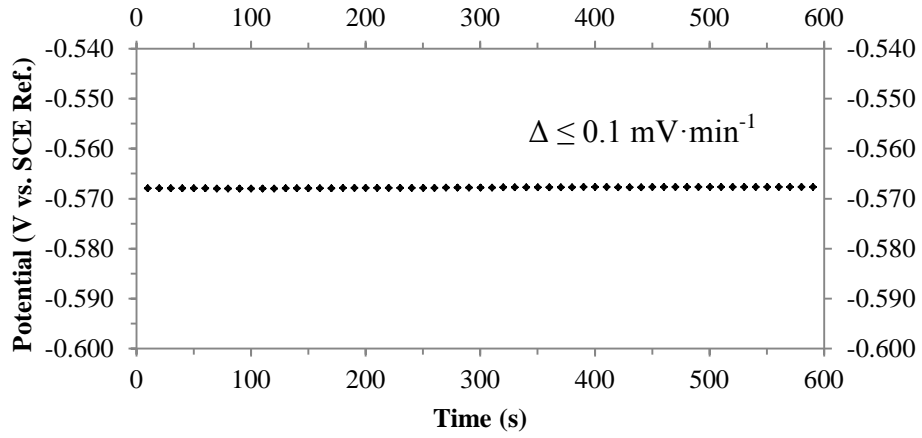


Figure 3-4 Typical Corrosion Potential Test Performance

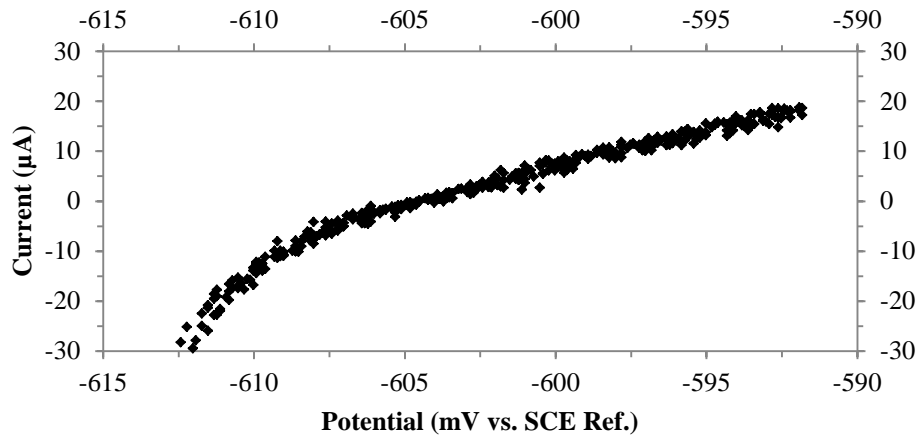


Figure 3-5 Typical Polarization Resistance Test Performance

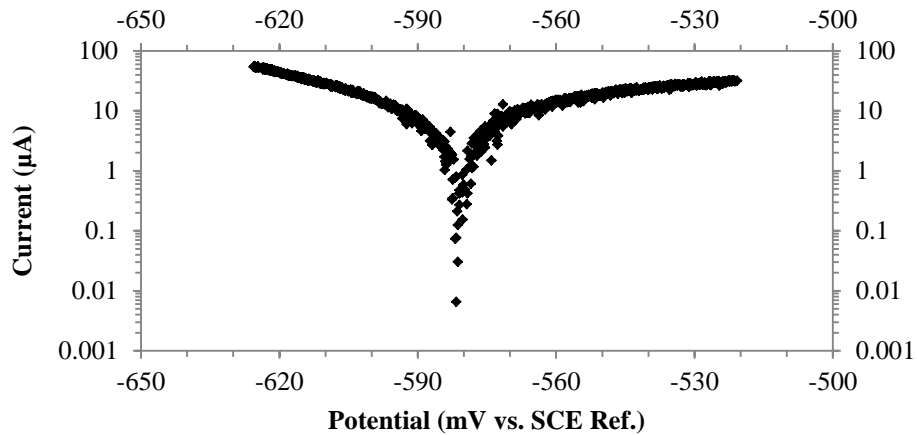


Figure 3-6 Typical Tafel Scan Test Performance

The Stern-Geary equation is utilized to calculate corrosion current values of samples based on the measured values of polarization resistance and coefficient extracted from the Tafel slopes (Equation 5).

$$I_{corr} = \frac{B}{r_p}$$

Equation 5

The collected results are then analyzed to identify samples which meet the criteria of active states of corrosion; corrosion potentials of the anodic bar less than -277 mV vs. a Saturated Calomel (Hg/HgCl) reference Electrode (SCE) or corrosion current density (I_{corr} normalized by anodic bar area) greater than 0.1-0.2 $\mu\text{A}/\text{cm}^2$ (ACI Committee 222 2001, Andrade and Alonso 1996).

3.3.2 Corrosion Damage Testing Methods

Two distinct test protocols were carried out to target the influence of hybrid fiber reinforcement on both the initiation and the propagation phases of corrosion damage.

The corrosion initiation phase was targeted utilizing ASTM G109 (2013) type testing in a manner similar to the testing carried out by Blunt (2008), where chloride penetration was measured through continuous salt water ponding of reinforced concrete beam elements. To further enhance the investigation of fiber reinforcement in relation to overall concrete durability an added dimension of damaged cover concrete was implemented by flexural loading prior to ponding. Doing so provided an indirect method of establishing the effectiveness of fiber reinforcement to minimize crack propagation during the cyclic bending tests and gain a measure of microcracked permeability in hybrid fiber reinforced concrete versus the macrocracked permeability of conventional concrete. Beyond the initiation phase, these beam samples were allowed to propagate to generate substantial corrosion induced cracking and were subsequently re-measured to investigate the roles of crack propagation and steel fiber corrosion on the residual capacity of reinforced concrete elements.

Corrosion propagation was addressed directly by bypassing the initiation phase through the dissolution of sodium chloride into the mixing water during concrete fabrication. By doing so, chloride ions were immediately present at the reinforcing bar surface and destabilized any formation of passive film. Fabrication of two sets of reinforced concrete cylinders allowed for testing of both conventional and accelerated corrosion damage with a goal of comparing the cracking damage of both cases in the context of fiber reinforcement. A representative value of corrosion current density of 1 $\mu\text{A}/\text{cm}^2$ was assumed based on the results of Blunt (2008) for chloride contaminated concrete of similar geometry from which the accelerated testing was carried out at a current density of 1 mA/cm^2 .

3.4 Materials

Low carbon steel reinforcement for all samples was purchased from local rebar suppliers. For all bar sizes greater than #4 (12 mm diameter), steel met the specifications of ASTM A615, while due to sourcing difficulty, all bars of size #3 (9 mm diameter) met the lower standards set by ASTM A36. The alloying composition and strength properties of both steel types as indicated by the corresponding mill certificates are provided in Table 3-1.

Table 3-1 Rebar Mill Certificates; Alloying Composition (%) and Strength (MPa)

	C	Mn	P	S	Si	Yield	Ultimate
A36	0.421	0.913	0.010	0.019	0.191	460	720
A615 ¹	0.398	1.038	0.013	0.023	0.108	460	730

¹Also contains Cr (0.102) and Cu (0.237) with all other alloying elements below 0.100 percent composition

The two concrete mixes of choice for investigation were the previously described Self-Consolidating Hybrid Fiber Reinforced Concrete (SC-HyFRC) and a reference Self-Consolidating Concrete (SCC) having an identical binder content and water to binder ratio of 0.45 (provided in Appendix B). Due to their chemical admixtures, both mixes were cast into molds for both corrosion initiation and corrosion propagation without the need for mechanical vibration.

Supplementary cylinders (100 mm diameter by 200 mm height) were cast for characterization of the effect of the 25 percent Class F fly ash replacement of portland cement in relation to relevant materials properties (concrete strength, chloride permeability) along with concrete containing a pure portland cement binder. In keeping with a standard curing procedure to be used for all concrete corrosion testing samples, the specimens were cured for 7 days in a room temperature fog room (96 percent relative humidity) after which they were removed and allowed to cure in ambient lab conditions until reaching an age of 28 or 84 days. Strength testing results, compiled in Table 3-2, are indicative of the pozzolanic reaction of the Class F fly ash having a slower rate of reaction than hydration of portland cement in addition to experiencing a dormancy period when stored dry, as occurs between the 28 and 84 day period.

Table 3-2 Fly Ash Influence upon Strength of Concrete Corrosion Mixes (MPa)

Age	Reference ¹	SCC ²	SC-HyFRC ²
28 days	53.1	37.4	39.3
84 days	52.9	36.7	36.2

¹Binder content by mass – 100 percent portland cement

²Binder content by mass – 25 percent Class F Fly ash, 75 percent portland cement

Determination of this dormancy was critical to the accelerated testing program due to the limited number of samples which could be tested simultaneously. By determining that no appreciable change in strength development took place between 28 and 84 days, it is assumed that all reinforced concrete cylinders had roughly the same level of unreacted cement and fly ash eliminating porosity from being a variable between samples cast of the same mix upon their participation in accelerated testing.

As both compressive strength and ion permeability can be correlated with concrete porosity, the strength results of Table 3-2 are indicative of SCC and SC-HyFRC mixes having similar chloride permeability coefficients. Such a postulation was tested experimentally by the NT Build 492 method of testing chloride migration. Utilizing an applied voltage, chloride ions are driven from a sodium chloride solution reservoir through a 100 mm diameter by 50 mm thick concrete disk cut out of 84 day aged cylinders, towards a positively charged plate in a sodium hydroxide reservoir for a prescribed length of time (Figure 3-7).



Figure 3-7 NT Build 492 Rapid Testing of Chloride Migration

Determination of a non-steady-state migration coefficient is made by subsequent identification of penetration depth by application of silver nitrate solution (Table 3-3). For the purposes of protection against corrosion damage, lower values of migration coefficients are indicative of more durable concrete.

Table 3-3 Concrete Mix Chloride Non-Steady-State Migration Coefficients ($\times 10^{-12} \text{ m}^2/\text{s}$)

	Reference ¹	SCC ²	SC-HyFRC ²
D_{nssm}	3.8	12.7	13.0

¹Binder content by mass – 100 percent portland cement

²Binder content by mass – 25 percent Class F Fly ash, 75 percent portland cement

As expected, the similarities of binder content and compressive strength of the SCC and SC-HyFRC translate to a strong similarity in chloride migration coefficient. As such, the apparent effect of fiber inclusion and possible changes in concrete porosity is deemed insignificant by this test method. Simultaneously the need for adequate and possibly extended curing of mixes incorporating pozzolanic materials such as fly ash is highlighted by Table 3-2 and Table 3-3, in order to generate concrete properties in line with conventional portland cement based composites.

3.5 Corrosion Testing Results

3.5.1 Corrosion Initiation Testing Results

Corrosion initiation testing conducted on reinforced concrete beam samples encompassed salt solution ponding of both preloaded (effectively precracked) and unloaded elements fabricated of both SCC and SC-HyFRC concrete mixes. All beam elements had dimensions of 152 by 152 by 610 mm with #3 (9 mm diameter) and #6 (18 mm diameter) reinforcing bars placed with 25 mm of clear cover at the top and bottom along the long axis. All reinforcing bars were prepared in a three part process; 1) an electrical connection to the bar was established by means of an insulated wire attached via ring terminal to a stainless steel screw threaded into a drilled hole at one end of

each bar, 2) removing the mill scale found on typical carbon steel rebars by sand blasting, 3) insulating the 4 inches of each bar end by application of a layer of MICCROStop lacquer followed by a layer of electrical tape and finished with a polyolefin heat shrink tube crimped at the free end to close. Mill scale removal by sand blasting was necessary in order to eliminate variable effects of chloride induced corrosion brought about by inhomogeneous cracking in the mill scale layer as described by Ghods et al. (2011). All reinforced beam samples were initially cured for 24 hours under wet burlap and plastic tarps after which they were demolded and placed in a fog room until reaching an age of 7 days. Following a further 21 days of dry curing, a subset of samples were tested in cyclic, 4-point bending having been inverted such that the top face during casting nearest the #3 rebar was placed face down and loaded in tension (Figure 3-8).

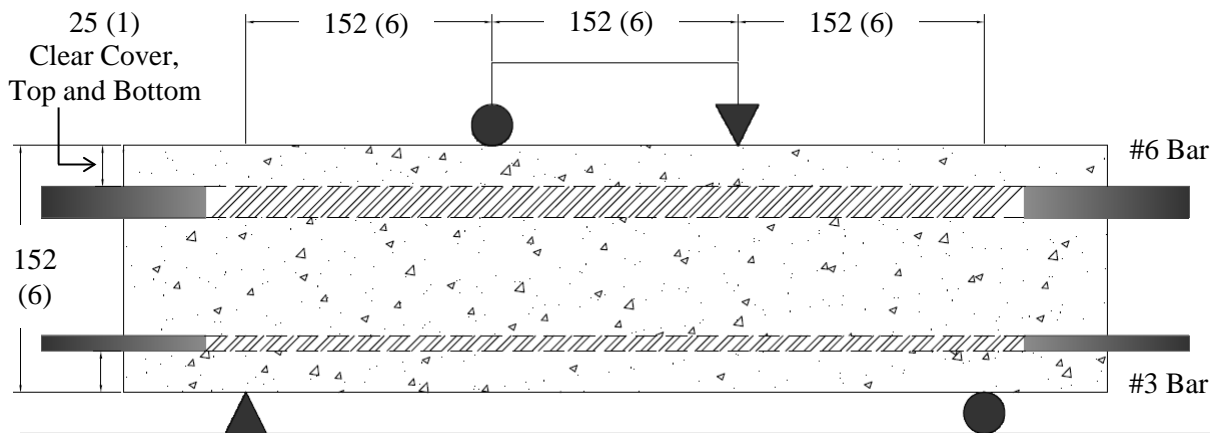


Figure 3-8 Reinforced Concrete Beam 4-Point Bending Test Dimensions, mm (inches)

Both SCC and SC-HyFRC type samples were exposed to 5 cycles of loading to 32 kN and unloading to 0 kN with their resulting load-deflection responses shown in Figure 3-9.

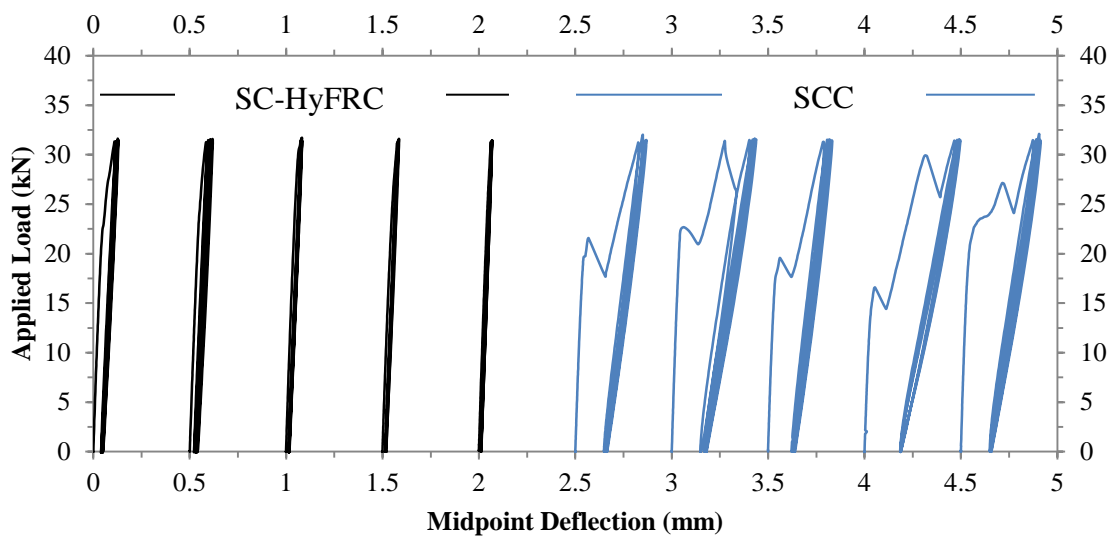


Figure 3-9 Cyclic Load Response of Reinforced Concrete Beams Prior to Corrosion Initiation

In the SCC beams flexural cracks develop between a load range of 16 and 23 kN with secondary cracking occurring in several samples at 30 kN. Splitting cracks, formed due to the radial tensile component of bearing stresses developed at the location of deformed “ribs” along the reinforcing bar when differential slip of the bar versus the surrounding concrete occurs after flexural cracking (Goto 1971), also opened to a significant length across all SCC samples (shown later in Figure 3-14a). In contrast, those beams fabricated with SC-HyFRC showed no instabilities in their load-deflection responses that would indicate the rapid formation of flexural cracking occurring during the prescribed loading protocol (with intact tensile surface shown later in Figure 3-14c). Taking into account the elastic behavior exhibited by SC-HyFRC samples in combination with the absence of splitting cracks on the tensile surface, the contribution of hybrid fiber reinforced concrete to carrying tensile load and suppressing cracking at the microscale is evident.

To characterize the cracks that were formed during the cyclic loading process, the tensile face of each sample was imaged using a flatbed scanner at 2400 dpi providing a pixel resolution of approximately 10 μm. All flexural and splitting cracks observable at this resolution are tabulated in Table 3-4.

Table 3-4 Cracking Behavior of Cyclically Loaded Reinforced Beam Samples

	Maximum Deflection (mm)	Residual Deflection (mm)	No. Flexural Cracks	Flexural Crack Width (mm)	Splitting Crack Length (mm)	Splitting Crack Width (mm)
SCC	0.37	0.16	1	0.30	180	0.09
	0.44	0.18	2	0.22	230	0.05
	0.33	0.14	1	0.32	250	0.12
	0.50	0.19	2	0.25	200	0.11
	0.38	0.14	2	0.20	130	0.07
SC-HyFRC	0.13	0.05	0	-	-	-
	0.12	0.04	0	-	-	-
	0.08	0.02	0	-	-	-
	0.09	0.02	0	-	-	-
	0.07	0.01	0	-	-	-

Consistent between all SCC mix samples is the presence of flexural cracks having a width greater than 200 μm, the limit suggested by Wang et al. (1997) after which ion transport is uninhibited by crack morphology/tortuosity. While all SCC mix samples displayed splitting cracks, the crack opening size is below those values that would be traditionally associated with the rapid ingress of chlorides. It is however important to note that the initiation of splitting cracks can only be brought about by damage incurred at the steel to concrete interface. Correspondingly, while the pathway from the tensile face to the reinforcing bar may be too tortuous for direct ion migration, those chlorides that travel through the transverse flexural cracks are likely to face relatively little resistance to lateral spreading along the region of damaged bond. Thus, rather than constraining the initial area of steel subjected to corrosion to the region of bar in close proximity to the intersection with the flexural crack, the initial area of steel

subjected to corrosion is more likely determined by the length of bar over which splitting cracks are evident (a surface area up to several orders of magnitude greater). Further, it is hypothesized that this action may be sufficient to produce a region of steel undergoing a form of crevice corrosion where by the local solution concentration deep within the splitting cracks become concentrated and exacerbates the oxidation of iron. In contrast, SC-HyFRC samples of this set did not exhibit measurable flexural cracks, such that it is expected that the concrete permeability has not been altered on the scale of orders of magnitude. It is however worth noting that residual deflection, as encountered in the SC-HyFRC beams, is an indicator of cumulative internal damage which in this scenario is prescribed to be microcracking.

In preparation of salt solution ponding, beam samples having been mechanically preloaded along with those that had undergone no loading were fitted with plastic walled ponding dams having a footprint of 100 by 406 mm on the face nearest the #3 reinforcing bar. Each dam was affixed to the concrete surface with Neoprene Rubber Flashing Cement such that a water tight seal was established. A latex based moisture barrier was provided to all concrete faces except for the bottom face, farthest from the ponding interface, in order to establish a directional flow of chlorides towards an evaporation surface. After testing each connection for water tightness over a 48 hour period, ponding reservoirs were filled to a depth of 25 mm with 3.5 weight percent NaCl solution, the wiring of the top and bottom bars was connected to allow for the development of a galvanic cell and the samples were placed within a 50 °C, 50 percent relative humidity environmental chamber.

Electrochemical testing of each beam was conducted periodically over a 10 month period during which ponding was maintained by adding additional salt solution as necessary to account for losses due to evaporation and ensure the concrete remained wetted. All potential measurements were taken relative to a Saturated Calomel Reference electrode submerged within the ponding solution (Figure 3-10). For potentiodynamic measurements, the lower passive #6 reinforcing bar was utilized as a counter electrode.

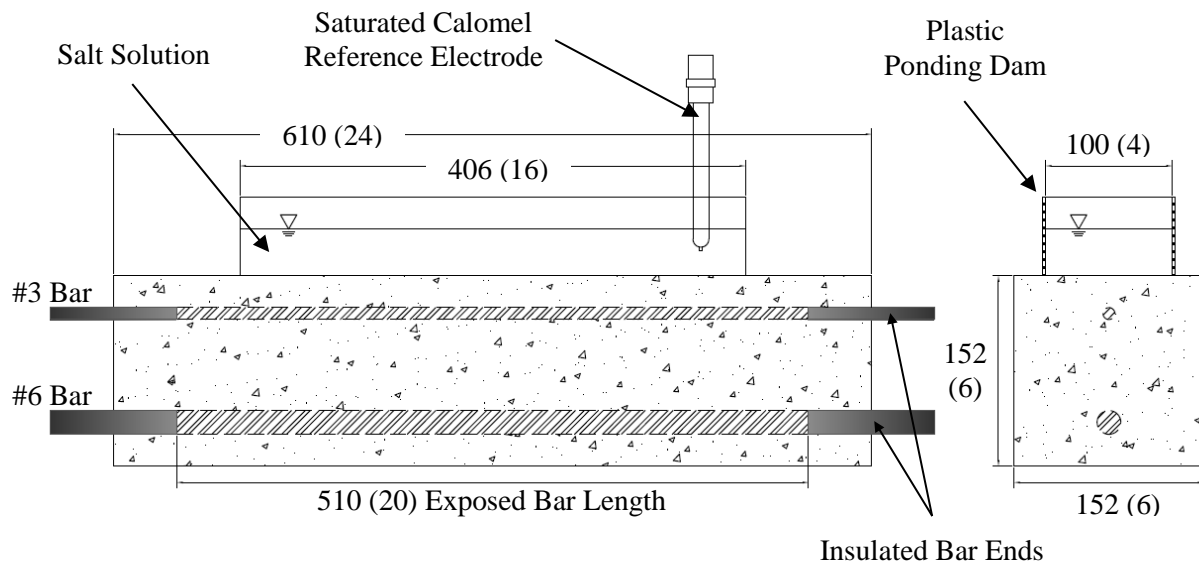


Figure 3-10 Reinforced Concrete Beam Electrochemical Test Setup, mm (inches)

Measurements of corrosion currents, galvanic current or microcell current, are normalized by the exposed surface of the working electrode bar (#3 reinforcement) being 152 cm². For uncracked

samples in which chloride penetration might be fairly assumed to occur at a similar rate across the entire ponding face, this normalization is likely inconsequential. However, for those samples in which flexural and splitting cracks are formed, the calculated value of corrosion current density utilizing this method underestimates the actual response to a degree determined by the relative area of the bar acting as an anode versus the entire surface area. This was deemed acceptable for both the lack of an efficient non-destructive method of determining appropriate anode area along a single electrode and the extent to which splitting cracks had developed along a large length of the bar.

Data collection was carried out on a weekly and biweekly schedule in the early age of corrosion testing in order to capture initiation activity within a relevant period of time. As testing progressed, due to the lack of differentiation from measurement to measurement, this schedule was relaxed to monthly and bimonthly testing. After 42 weeks, all of the samples were left in storage and the ponding solution was allowed to evaporate with the chamber conditions (50 °C and 50 percent relative humidity) and absorbed chloride content left to propagate corrosion damage.

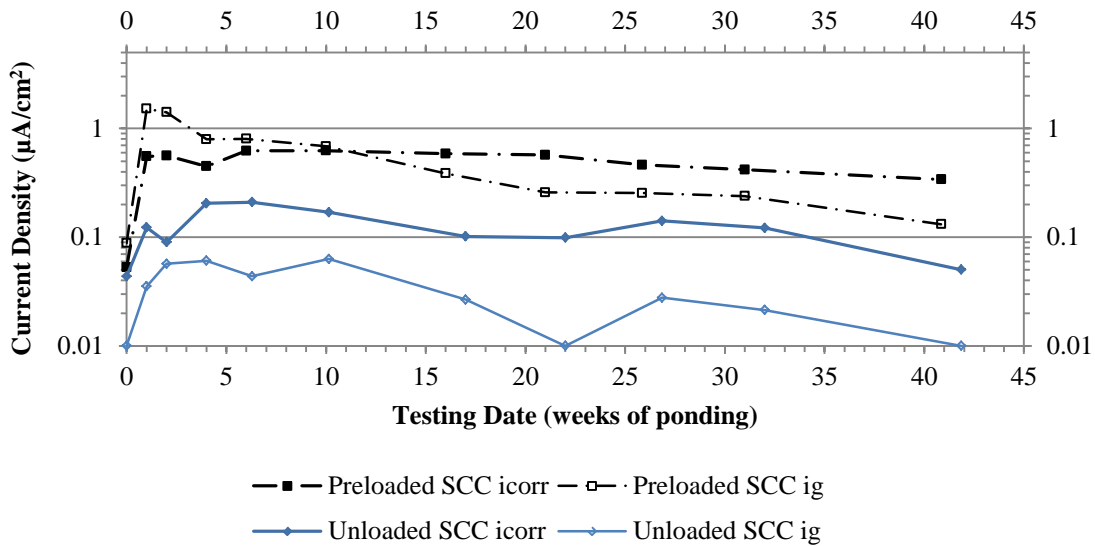


Figure 3-11 Corrosion Current Density of SCC Beams (i_{corr} – microcell, i_g – galvanic)

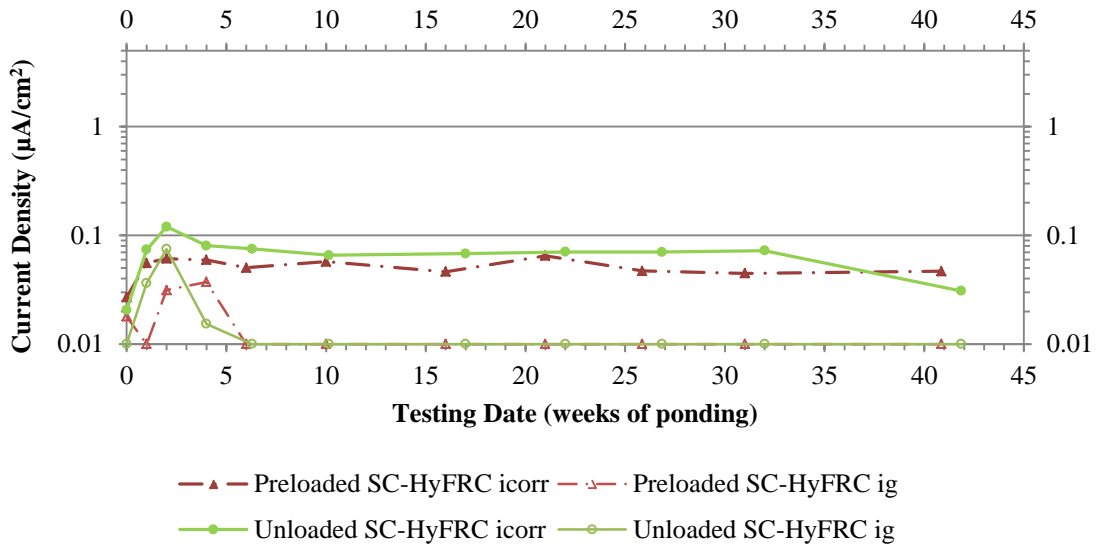


Figure 3-12 Corrosion Current Density of SC-HyFRC Beams (i_{corr} – microcell, i_g – galvanic)

As expected, the large crack openings existing within the preloaded SCC beams allowed for rapid transportation of chloride ions to the depth of reinforcement and depassivated the steel which was confirmed by the level of corrosion activity noted at the first measurement point of 1 week following the ponding initiation (Figure 3-11). Behavior of all other samples at that stage of testing indicated that sufficient cover concrete protection remained to provide a barrier to chloride migration (Figure 3-11 and Figure 3-12). Following 1 month of ponding, the unloaded SCC beams were the next to exhibit a corrosion current density in excess of $0.2 \mu A/cm^2$, while at no point during the entire 42 week ponding period was the threshold broken by either the preloaded or unloaded SC-HyFRC samples. Simultaneously, only in the case of the cracked samples did the galvanic current density ever exceed the microcell current density and even then after an initial 11 weeks it was overtaken. It should be noted that the unloaded SCC sample set displayed the largest variation in performance during the period of ponding with a significant spread in monitored corrosion activity. It is unclear whether this variability was brought about by fabrication issues, curing issues or general test protocol issues. For all other subcategories of samples the variability in sample performance (measured corrosion potential, polarization resistance, etc.) was confined to a limited range.

Following 12 months of storage, each sample was removed from the environmental chamber and inspected for accumulated corrosion damage. In all cases of concrete type and initial loading condition, the samples displayed signs of distress exceeding their earlier state during active ponding. For the SCC mixes this distress was illustrated as corrosion induced splitting crack formation (in unloaded samples) and propagation (in preloaded samples) along the top reinforcing bar and spalling of chunks of concrete emanating from splitting cracks formed around the bottom reinforcing bar predominantly in preloaded samples (Figure 3-13 and Figure 3-14).

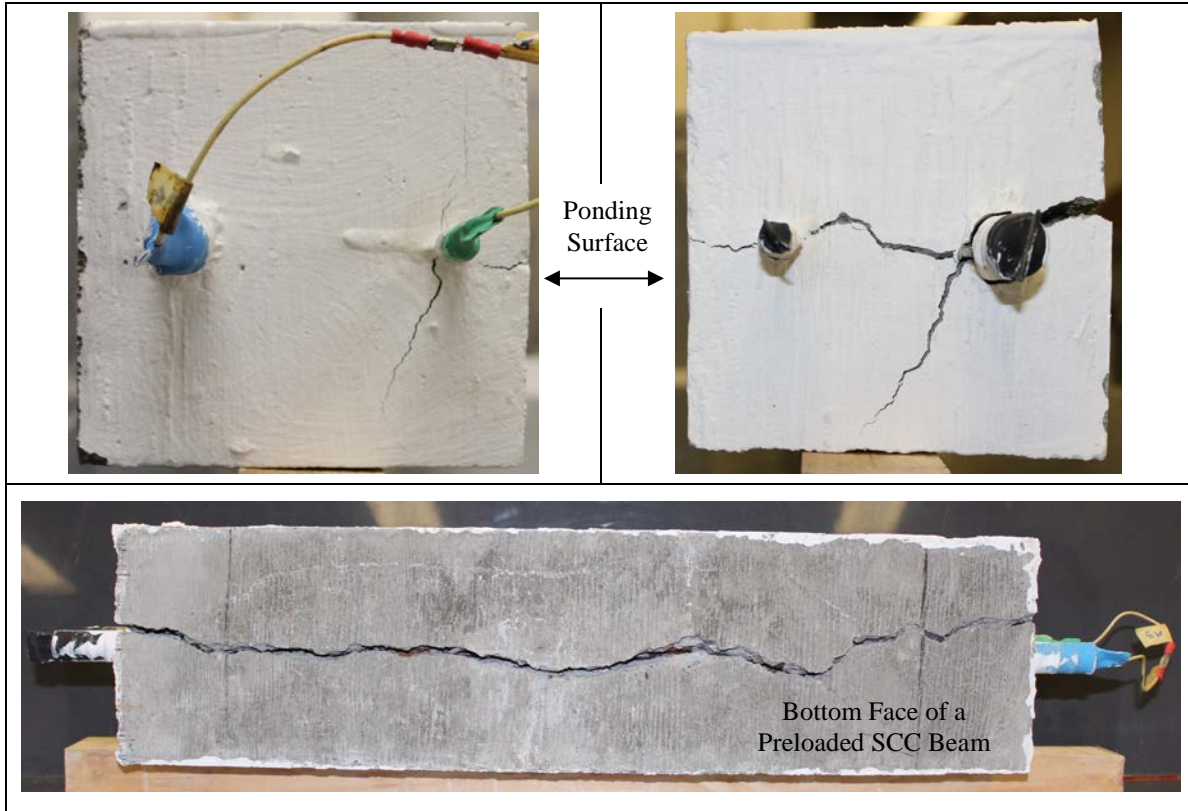


Figure 3-13 Observations of Splitting Crack Damage in Various SCC Beams

For the SC-HyFRC mixes, distress was noted as corrosion of steel fibers at both the bottom face and at the ponding surface with localized cases of mortar pop-outs. However, no splitting crack was apparent on any face of the SC-HyFRC samples illustrating the crack resistant nature of fiber reinforcement in the cover layer of concrete (Figure 3-14). Corrosion testing confirmed the physical observations in the sense that samples which were previously passive due to a lack of chloride penetration during ponding were now actively corroding. Similarly the magnitude of active corrosion in those samples having splitting cracks, whether induced solely by corrosion damage (unloaded SCC) or a combination of mechanical and corrosion damage (preloaded SCC) is noted to substantially exceed the values reported earlier in Figure 3-11, which emphasizes the importance of local crack control achieved with fiber reinforcement. A representative sample of before (at the culmination of ponding) and after readings of the top #3 reinforcing bar are provided in Table 3-5 with the addition of measurements of the lower #6 reinforcing bar.

Table 3-5 Final Corrosion Measurements of SCC and SC-HyFRC Corrosion Beams

	SCC, Unloaded	SCC, Preloaded	SC-HyFRC, Unloaded	SC-HyFRC, Preloaded
#3 Bar, Ponding E_{corr} (mV vs. SCE)	-145	-380	-120	-290
#3 Bar, Final E_{corr} (mV vs. SCE)	-500	-520	-460	-470
#3 Bar, Ponding i_{corr} ($\mu\text{A}/\text{cm}^2$)	< 0.1	0.3	< 0.1	< 0.1

#3 Bar, Final i_{corr} ($\mu\text{A}/\text{cm}^2$)	2.1	5.9	0.2	0.6
#6 Bar, Final E_{corr} (mV vs. SCE)	-130	-500	-100	-150
#6 Bar, Final i_{corr} ($\mu\text{A}/\text{cm}^2$)	< 0.1	58.6	< 0.1	< 0.1

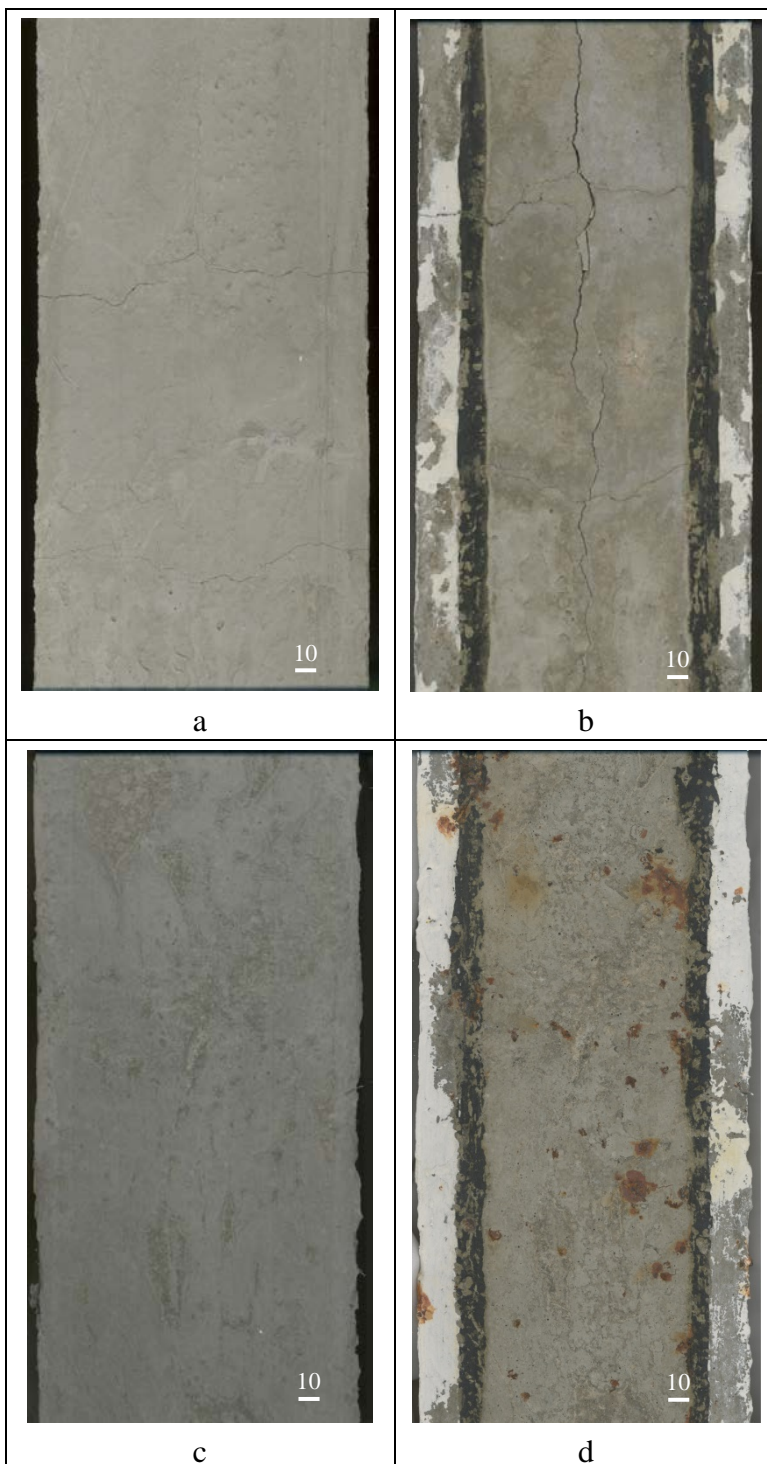


Figure 3-14 Prior to Corrosion (a,c) and Final (b,d) Tensile Face Comparison of Preloaded SCC (a,b) and SC-HyFRC (c,d) Beam Samples, mm

The influence of corrosion damage on residual flexural capacity was determined by loading the corroded beam samples in four point bending monotonically to their capacity. Due to limitations within the support system to accommodate non-planar surfaces, loading of SCC beams having extensive splitting cracks to the point of spalling was not possible. While residual flexural capacity data could not be collected for unloaded and loaded SCC beams due to their extensive corrosion damage (Figure 3-13), it should be expected that due to the splitting cracks that were formed in the tensile region, nearly all bond between reinforcing bar and concrete was lost thus providing negligible tensile contribution to a resisting moment couple. With respect to the SC-HyFRC beams, the residual flexural testing illuminates whether the corrosion of surface fibers limits the overall contribution of fiber reinforcement to carrying tensile load as had been observed in Figure 3-9. Utilizing flexural data gathered 28 days after sample fabrication and prior to any damage, displayed as “SC-HyFRC” and “SCC” in Figure 3-15, it is apparent that despite the corrosion damage accrued in either preloaded or unloaded SC-HyFRC beams their performance falls within the envelope of undamaged fiber reinforced samples and still exceeds the performance of undamaged SCC samples.

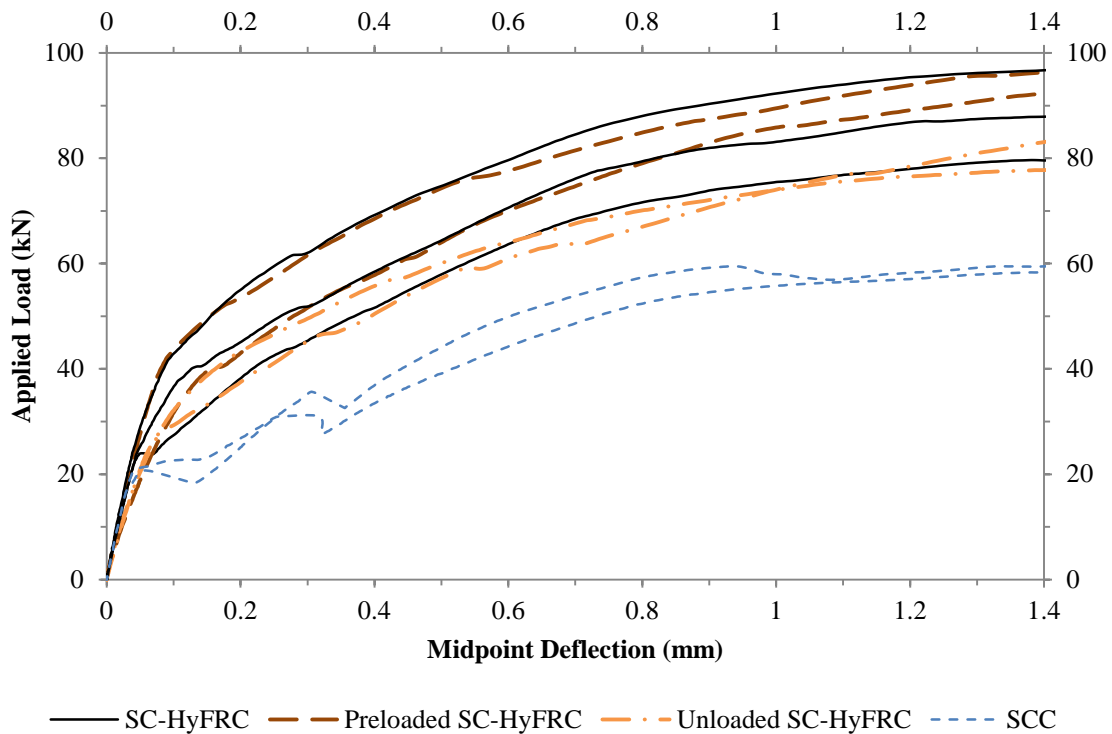


Figure 3-15 Residual Flexural Capacity Testing of Corroded SC-HyFRC Beams Relative to Original 28-Day Flexural Response of SCC (dashed blue) and SC-HyFRC (solid black) Beams

Based upon flexural capacity comparisons, the corrosion of steel fibers to the degree encountered during this testing can be considered inconsequential to determining overall load-deflection behavior. In closing, it can be stated that despite the active levels of corrosion established along the reinforcing bar surface (Table 3-5), those samples fabricated with SC-HyFRC and subjected

to identical loading conditions can be counted on to contribute to the ductility of reinforced concrete in a manner which conventional concrete cannot. Similarly, by comparison of the corrosion rates at the termination of testing it is apparent that the reduced corrosion rate associated with SC-HyFRC can provide a measure of durability enhancement. In combination these ductility and durability benefits generate substantial benefits to the sustainability of structures fabricated with SC-HyFRC that might be reasonably expected to encounter corrosive environments.

To better understand the role played by fiber reinforcement and associated crack control upon the migration of chloride ions and the transition from the initiation phase to the propagation phase, a single SC-HyFRC beam was cyclically loaded to induce flexural cracks in the same manner as the beams described earlier. High resolution imaging determined that the beam had a single 80 μm flexural crack and no evidence of splitting cracks. This crack being roughly one-half to one-third the size of the cracks encountered in the preloaded SCC beams would not normally be associated with corrosion susceptibility. However, over the course of monitoring the precracked SC-HyFRC in the same procedure as the other beams (Figure 3-16) it became apparent that an active state of corrosion was reached. Rapid ingress of chloride ions produced depassivation of the #3 reinforcing bar within the first week of ponding similar to the preloaded SCC beams, suggesting a modification to the crack path between the ponding surface and reinforcing bar depth the allowed for easier transport than would normally occur in a crack of 80 μm .

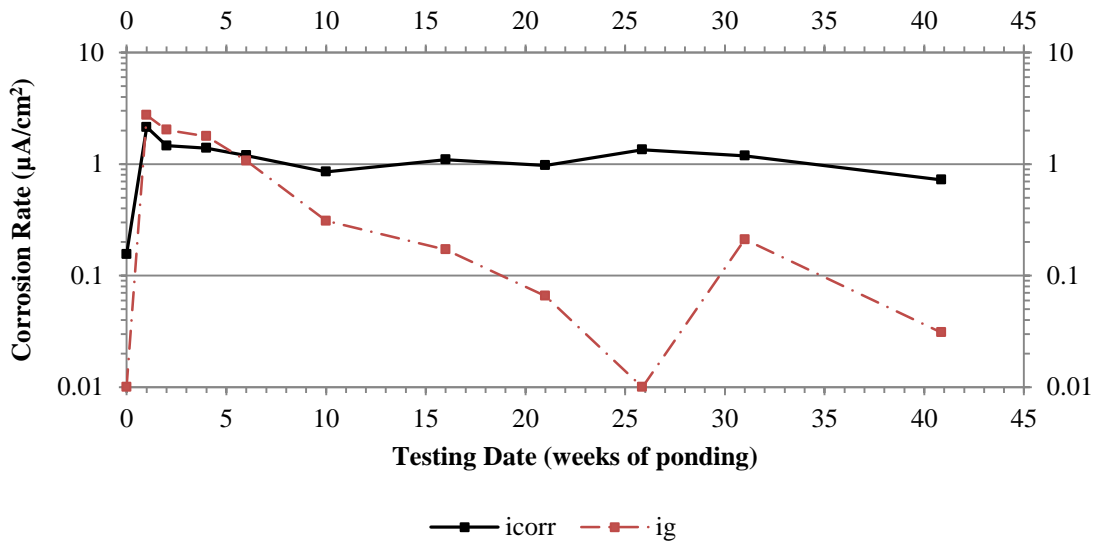


Figure 3-16 Corrosion Current Density of Flexure-Induced Precracked SC-HyFRC Beam

From a corrosion rate perspective, though the precracked SC-HyFRC beam exhibited behavior consistent with the preloaded SCC beams during the ponding duration, during the period of long term storage the presence of fibers restricted the development of splitting cracks that would otherwise have generated damage at the #6 bar location. Rather the final measurement performance is more closely related to the values observed for unloaded SCC samples in which the top bar is undergoing corrosion but the bottom bar remains passive (Table 3-6). External observations of the ponding surface after corrosion show the onset of a short length of splitting crack which had not existed prior (Figure 3-17). Yet in large part the

appearance of the beam, specifically the degree of fiber corrosion and flexural crack width, were unchanged.

Table 3-6 Final Electrochemical Measurements of Flexure-Induced Cracked SC-HyFRC Beam

#3 Bar, Ponding E_{corr} (mV vs. SCE)	#3 Bar, Final E_{corr} (mV vs. SCE)	#3 Bar, Ponding i_{corr} ($\mu\text{A}/\text{cm}^2$)	#3 Bar, Final i_{corr} ($\mu\text{A}/\text{cm}^2$)	#6 Bar, Final E_{corr} (mV vs. SCE)
-390	-390	0.7	2.3	-140

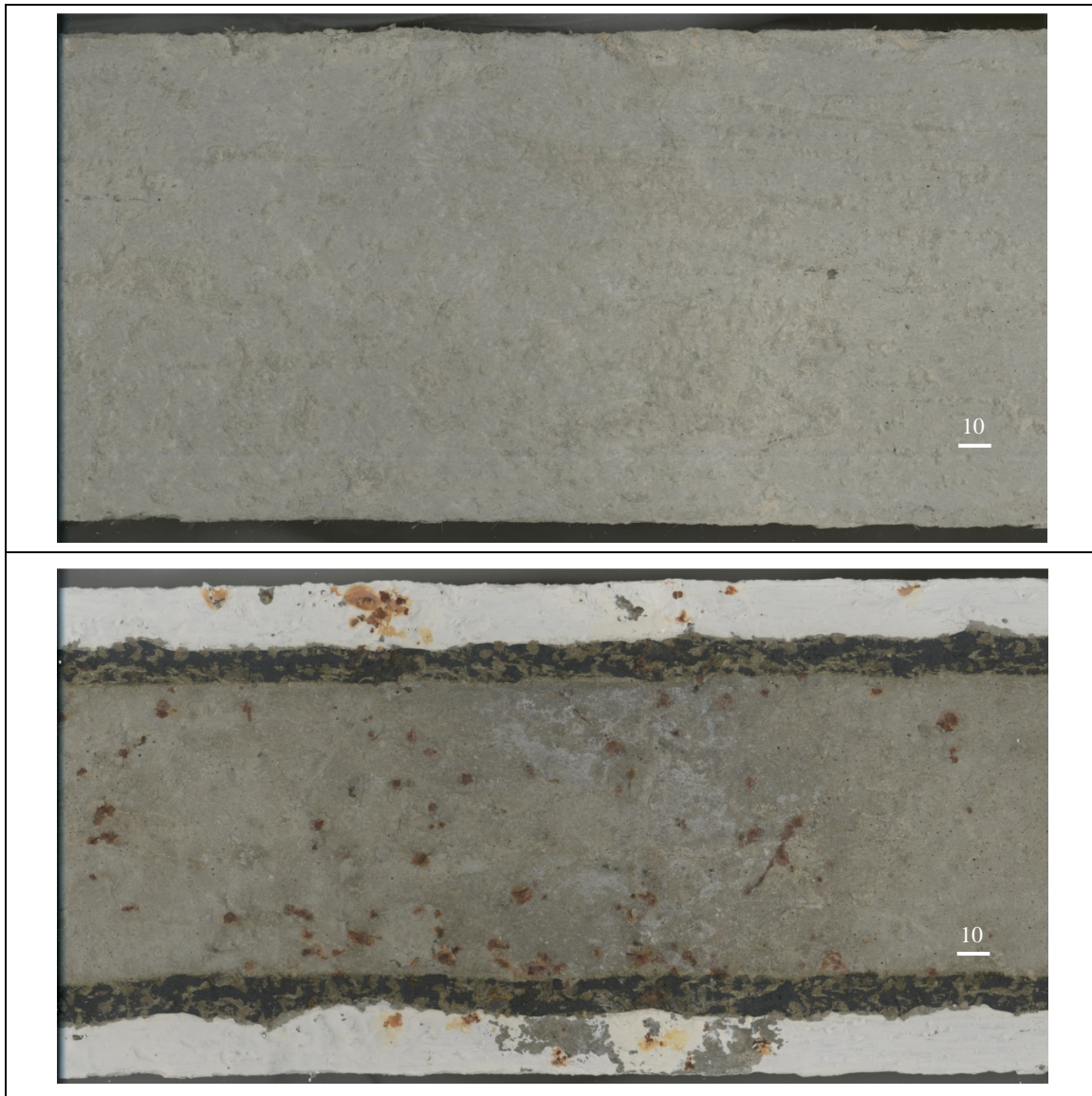


Figure 3-17 Surface Imaging of the Cracked SC-HyFRC Beam Prior to and After Corrosion Damage, mm

Upon flexural reloading, the presence of high corrosion rates recorded along the tensile reinforcing bar did not appear to provide any detrimental effect to the bending performance. The elastic performance of the beam was largely uncompromised, with only the peak composite

loading showing some signs of degradation (Figure 3-18). Most likely this degradation is associated with bond deterioration occurring with the advanced levels of corrosion damage as the onset of bar slip was both more sudden and severe than is typically associated with the SC-HyFRC mixture.

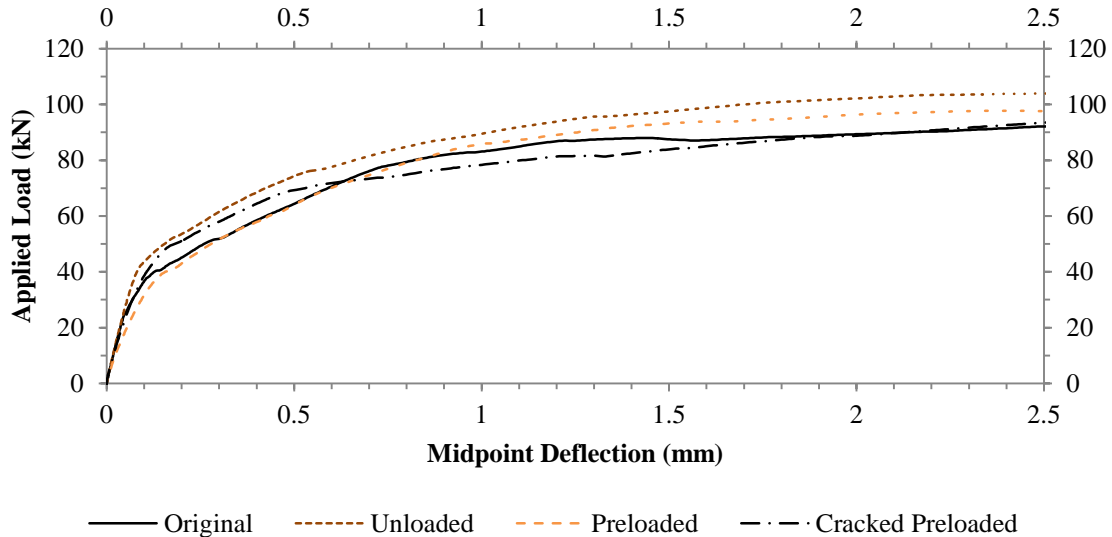


Figure 3-18 Residual Flexural Capacity of Corroded Cracked SC-HyFRC Beam Relative to Original and Corrosion-Damaged Unloaded/Preloaded SC-HyFRC Beams

3.5.2 Corrosion Propagation Testing Results

Corrosion propagation testing of hybrid fiber reinforced concrete consisted of conventional and accelerated corrosion testing of reinforced concrete cylinders fabricated of SC-HyFRC and a reference SCC for comparison. Reinforced cylinders for both tests were fabricated to have a single #8 (25 mm diameter) A615 steel reinforcing bar placed along the central axis of a 100 mm diameter by 200 mm height concrete cylinder (shown in Figure 3-19). Each 254 mm length of bar was prepared in a manner similar to those used in the corrosion initiation testing such that mill scale was removed by sand blasting, an electrical connection was established by a wire connection to a stainless steel screw threaded into one end of the bar, and the bar ends were insulated by a multilayer protective coating comprised of MICCROStop laquer, electrical tape and polyolefin heat shrink tubing. Sodium chloride was dissolved into the concrete mixing water to establish a chloride ion content equivalent to 4 percent of the cement by mass which ensured depassivation of the 111 cm² exposed bar surface area.

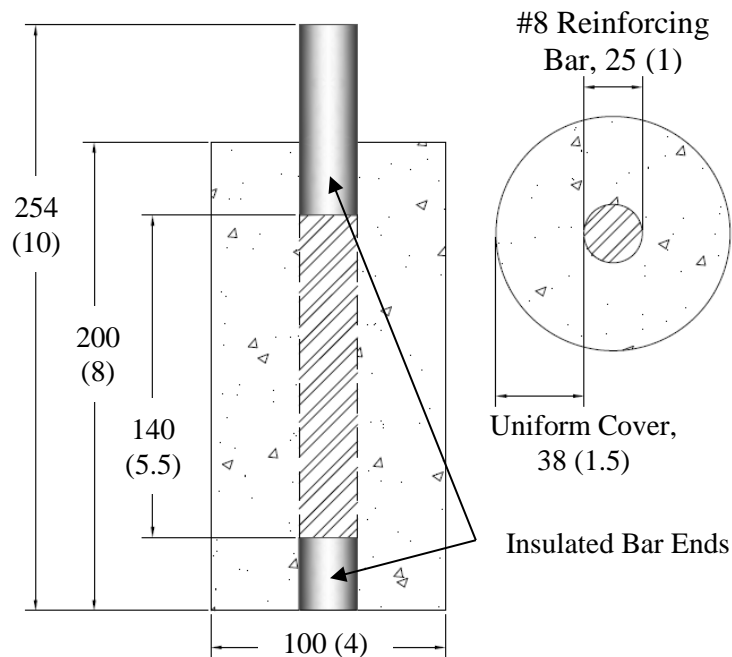


Figure 3-19 Lollipop Sample Dimensions, mm (inches)

Following a conventional testing protocol established by Blunt (2008), the reinforced concrete cylinders were cured under wet conditions for 7 days and then air cured for an additional 28 days, after which samples were returned to the fog room and allowed to remain saturated with periodic removal for electrochemical testing. Testing was carried out by immersion of the sample in a 3.5 weight percent salt solution bath, utilizing a stainless steel mesh wrapped around the circumference of the cylinder to serve as a counter electrode and a wetted sponge providing a conductive connection between the concrete surface and the saturated calomel reference electrode (Figure 3-20). Because of the uniform dispersion of chlorides throughout the sample, current is normalized by total exposed bar surface area for all presentations of corrosion current density. Having reached a steady corrosion current density within one year without exhibiting any propensity for crack formation, the storage cycle was altered after 80 weeks (denoted by the dashed vertical line in Figure 3-21) to cycle between saturated storage in the fog room and dry storage on a lab shelf.

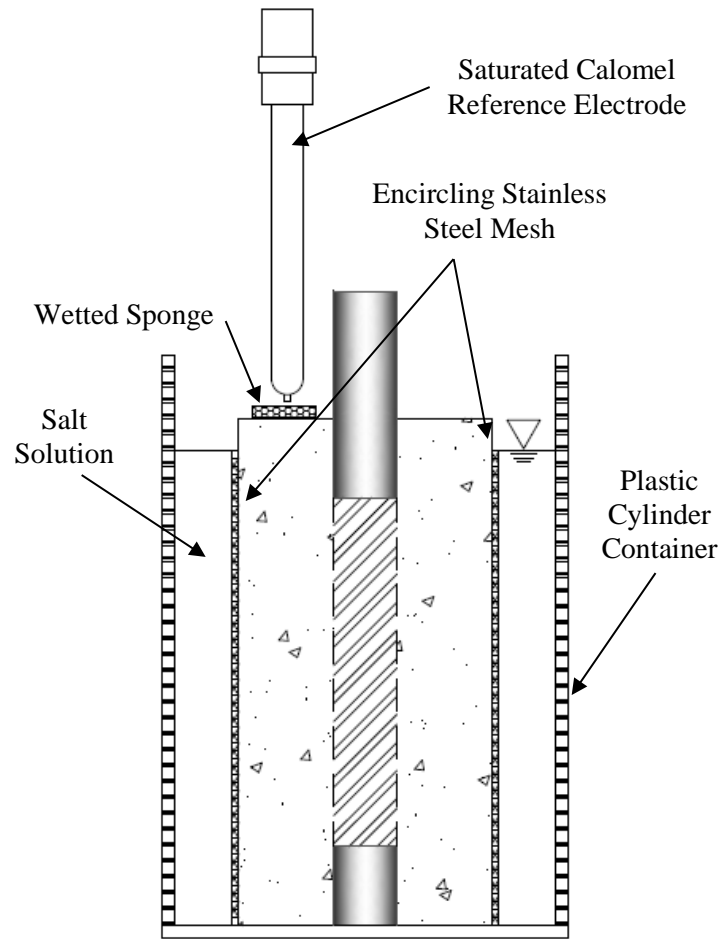


Figure 3-20 Lollipop Sample Electrochemical Test Setup

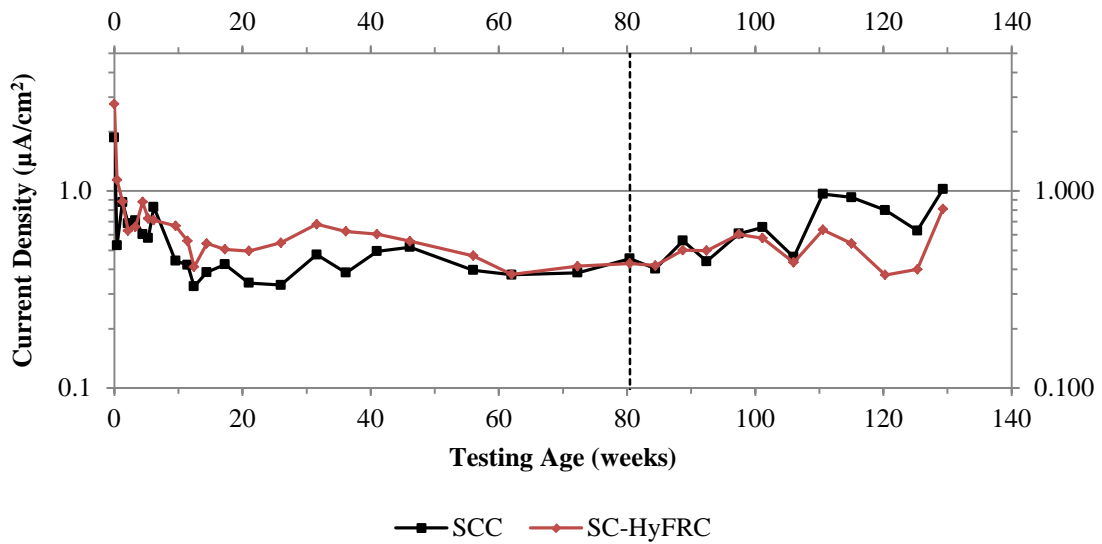


Figure 3-21 Conventional Corrosion Propagation Test Response of SCC and SC-HyFRC Mixes

Due to the inclusion of chloride ions within the fresh concrete, from the first measurement point taken at a concrete age of 4 weeks (0 weeks testing age) both sample types exhibited corrosion potentials more negative than -500 mV versus SCE and corrosion current densities greater than $1 \mu\text{A}/\text{cm}^2$. Over the course of the next 5 months as concrete hydration continued and the material porosity decreased, the sustained corrosion rate followed a general trend downward, stabilizing at a moderate $0.5 \mu\text{A}/\text{cm}^2$ for both mix types. Following the implementation of wet/dry cycling at 80 weeks, a slow increase in average corrosion rate was noted culminating in cracks being observed in the SCC cylinders prior to the measurements taken at a testing age of 110 weeks.

Accelerated testing of corrosion propagation behavior was conducted on identical reinforced concrete cylinder samples by the impressed current technique utilizing a test setup largely similar to that depicted in Figure 3-20 with the removal of the reference electrode. After completing the 28 day curing protocol, samples were submerged in a salt solution bath and allowed to saturate. The Gamry Instruments potentiostat was used to apply a steady current of $1 \text{ mA}/\text{cm}^2$ to oxidize iron at the bar surface with the encircling stainless steel mesh used as the counter electrode. The magnitude of current was chosen based on steady-state response of the samples of Blunt (2008) having a water to binder ratio of 0.54 exhibiting current densities of $1 \mu\text{A}/\text{cm}^2$ over a 1 year period with no external signs of distress. Exposure durations were limited to 1 and 2 days, after which samples were placed back in salt solution baths and periodically tested for corrosion activity to determine the influence of the corrosion induced cracks formed under high current on the steady state corrosion current density. Under the assumption that 100 percent of the applied current would go to iron oxidation, the magnitude of current applied for 1 and 2 days would translate to 2.7 and 5.5 years of continuous behavior by the samples of Blunt. Following the accelerated phase of testing, samples were tested for corrosion via the linear polarization resistance technique carried out in the configuration of Figure 3-20. Calculated corrosion current densities of the corroded reinforced cylinders are shown in Figure 3-22 where “-1” and “-2” signify exposure to the elevated current for 1 and 2 day durations.

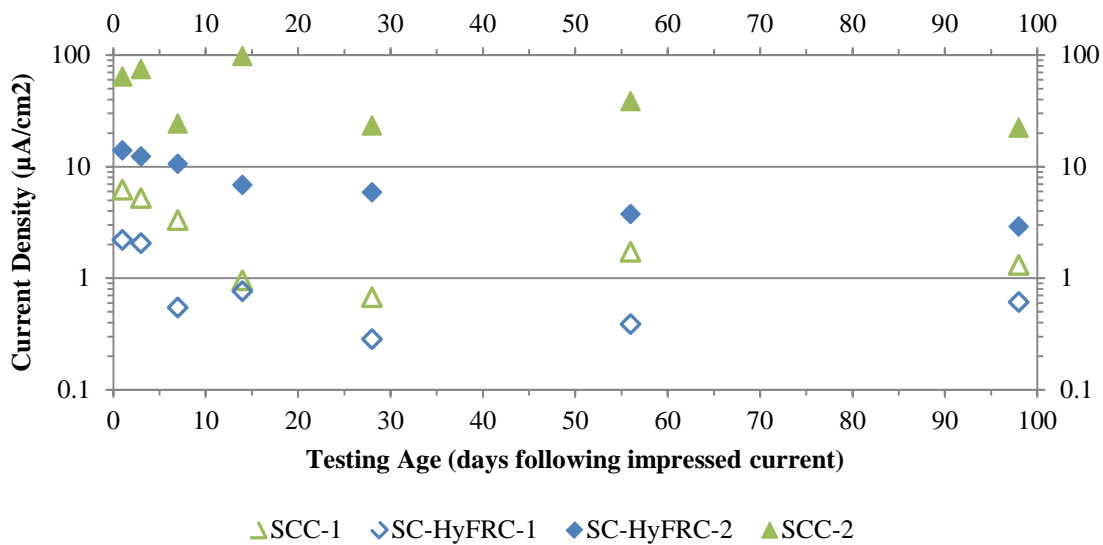


Figure 3-22 Accelerated Corrosion Propagation Test Response of SCC and SC-HyFRC Mixes

As anticipated, the greater exposure times, 2 days of continuous current, correlated well with the extent of cracking damage incurred by the cylinders. Similarly, the presence of fibers and their associated crack resistance produced comparable reductions in cracking damage (shown later in Figure 3-27 and Figure 3-28). Both of these factors are well represented in the corrosion current densities of Figure 3-22 in which a ranking of most to least corroding sample set would be; SCC-2, SC-HyFRC-2, SCC-1 and SC-HyFRC-1.

3.6 Corrosion Testing Discussion

3.6.1 Corrosion Initiation Testing Discussion

Due to the differences in sample response observed between the period of active ponding and the final observations, discussion of issues encountered is split to address those features for which regular measurements provide a more complete time history versus the relative snapshot of the damage state taken at the final measurement.

The relative magnitudes of microcell and galvanic current developed within each subset of beams may be occurring because of a theorized critical cathode to anode area ratio necessary for macrocell current development. Specific to the preloaded SCC being the only set for which galvanic current exceeds microcell current, as the initial anode area defined by depassivation is limited to the steel surface area in direct proximity to cracking the cathode area (bottom bar electrode) is sufficiently large and observed to produce a galvanic current in excess of the microcell current. However, as the chloride ions migrate along the length of the top bar the anode area increases while area ratio reduces bringing about the slow decay observed in Figure 3-11. Throughout the other beam types, the lack of pre-installed cracking did not allow for rapid heterogeneous migration of chloride ions but rather a more homogenous front of chlorides descended along the entire bar length beneath the ponding reservoir. Specific to the two sets of SC-HyFRC beams, the compiled electrochemical data would strongly suggest that cyclical loading at the load level used is responsible for no differentiation in response compared to the unloaded SC-HyFRC beams. The effective suppression of flexural cracking allows the cover concrete to maintain its full protective capacity with respect to chloride permeability within the 40 week duration of this non-destructive analysis phase of testing.

Utilizing destructive analysis methods at the completion of corrosion testing, several issues of critical interest to describe the damage propagation observed are correlating chloride migration depth with the depassivation of the bars evident in Table 3-5 and determining the distribution of steel fiber corrosion apparent in Figure 3-14 as it relates to chloride contamination and concrete carbonation. Visual indication of these issues was accomplished by core drilling full depth samples from all beam types at locations adjacent to the bar within the ponding footprint. One set of cores were cracked open by the splitting tension test with manual prying of the fiber reinforced samples required to separate the opposing faces. From each core sample this allowed colorimetric indications by both silver nitrate staining to determine chloride migration and phenolphthalein staining to determine carbonation depth. As expected, based on the corrosion damage occurring in the bottom bar of the preloaded SCC samples, silver chloride precipitates were evident through the entire depth of the core. Silver chloride precipitate depth of the unloaded SCC samples varied in a manner similar to their corrosion performance with some samples showing full depth penetration while for others the presence of silver chloride was contained to the top most 75 mm. In contrast, for SC-HyFRC cores the silver chloride precipitates were only measured to depths of 24 mm and 44 mm from the ponding surface for the unloaded and preloaded beams respectively (Figure 3-23a,b). Such a result is consistent with the

perception of internal microcracking having been established as evidenced by the residual displacements observed following cyclical loading. Over the course of this investigation the microcracking, though determined to be smaller than 10 μm in size by lack of scanner imaging, participated in increasing the ion mobility because of increased porosity within the concrete. If corrosion-induced splitting cracks had been suppressed in the unloaded SCC beam it would be expected that chloride migration depth would be of a scale similar to that of the unloaded SC-HyFRC core, however the magnitude of splitting cracks that formed in the unloaded SCC beam (Figure 3-13) in some cases allowed for rapid migration to the bottom bar even after the conclusion of ponding. It is also important to point out that no effort was made to correlate the local chloride content necessary for steel corrosion with the chloride content necessary to generate the colorimetric differentiation associated with the silver nitrate staining test. As such, despite the seemingly strong correlation between chloride depth and reinforcing bar half-cell potentials it is possible that the depths reported based on color underestimate the depth to which the critical chloride content has reached. This was later expanded upon by direct chloride content analysis with results to be discussed later that largely confirm and verify the usage silver nitrate staining as an efficient method of determining chloride profiles in concrete. Carbonation depth testing by phenolphthalein indicator likewise illuminates regions of concrete at which the extent of carbonation has reduced pH to 8, below the value necessary to destabilize steel passivation, however it is utilized here for rapid identification with an acceptable margin of error. All cores regardless of concrete type or initial loading state exhibited approximately equal carbonation results with depths extending 3 mm from the top ponding face and 8 mm from the unsealed bottom beam face (Figure 3-23c). Such results are consistent with the fact that the top face was immersed by salt solution for the first 10 months and subsequently protected from steady airflow generated by the chamber circulation system by the in-place reservoir walls while the bottom face had roughly double the direct exposure time to the environmental chamber conditions.

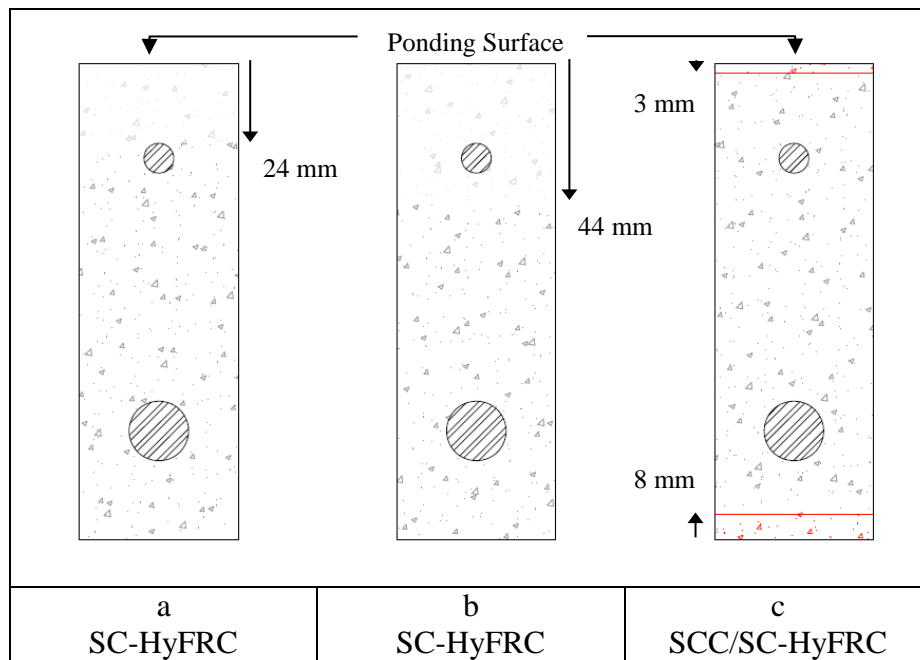


Figure 3-23 Color Indicator Stained Cores of Concrete; a) AgCl Depth in Unloaded SC-HyFRC Beams, b) AgCl depth in Preloaded SC-HyFRC Beams, c) Carbonation Depths (Consistent in all SCC and SC-HyFRC Beams), Approximate Depths of Reinforcing Bars Shown for Reference

Analysis of fiber corrosion as a function of depth and acid-soluble chloride content analysis was performed by segmentation of a second set of concrete cores extracted from the SC-HyFRC beams into six 25 mm disks. Each disk was crushed and ground by mortar and pestle to remove all adhered pieces of cement after which the steel fibers could be extracted while the pulverized concrete was retained for acid digestion. Chloride content analysis was carried out by the protocols outlined in ASTM C1152 (2004) utilizing 1+1 nitric acid to digest the concrete powder followed by a silver nitrate titration to determine the equivalence points corresponding to Cl⁻ ion activity in solution for each 25 mm segment of beam depth. The resulting chloride contents are plotted in Figure 3-24 having been normalized by the concrete binder content. The approximate depths of the #3 and #6 reinforcing bars are outlined at heights of 127 and 44 mm from the bottom beam face (corresponding to depths of 25 and 108 mm from the ponding surface), with the quantity of chlorides at each location consistent with the earlier described measurements of corrosion activity.

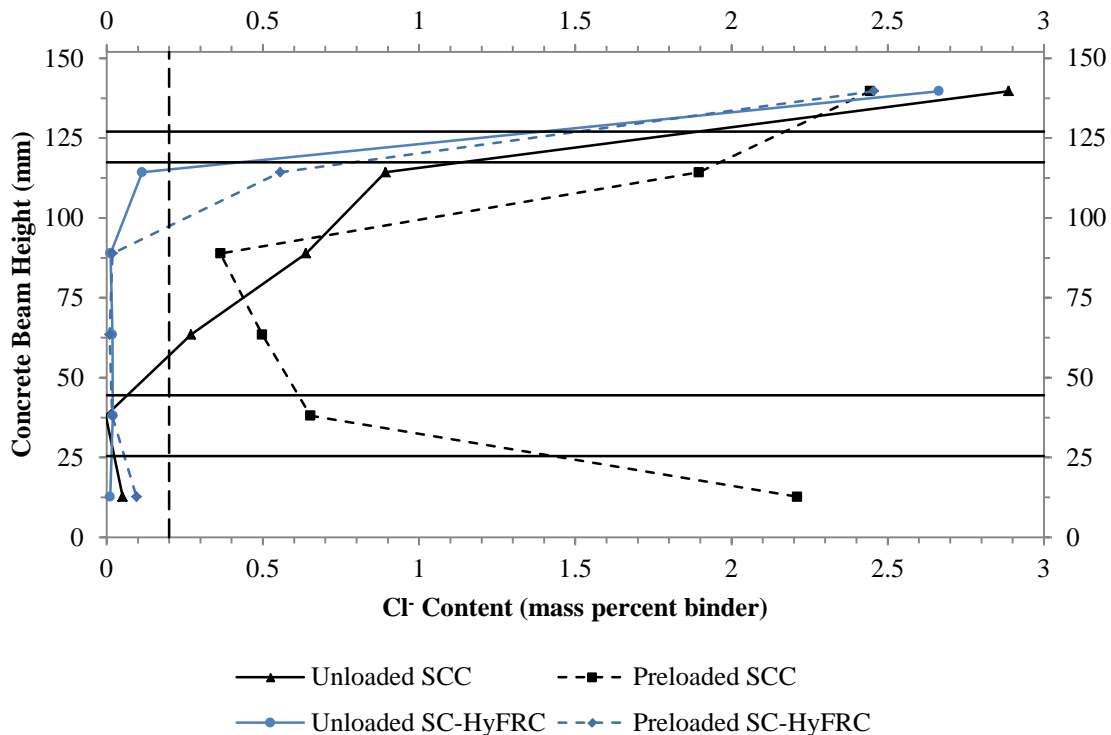


Figure 3-24 ASTM C1152 Chloride Concentration Profile of SCC and SC-HyFRC Beam Cores, with ACI 222 (2001) Limit of 0.2 Percent and Reinforcing Bar Locations Shown for Reference

Relative to the silver chloride precipitate color method, the chloride content analysis confirms the greater depth of chloride migration in the preloaded SC-HyFRC sample versus unloaded SC-HyFRC sample. Within the second 25 mm segment from the ponding surface (25 to 50 mm of depth), at which point the silver chloride precipitate method did not uncover chlorides in the unloaded fiber core, the acid soluble chloride content is measured to be 0.11 percent of binder mass which is below the 0.2 percent ACI limit. Conversely, the preloaded SC-HyFRC sample is noted to have a chloride content of 0.56 percent of binder mass in agreement with the depth of silver chloride precipitates reaching 44 mm. Both methods are consistent in evaluating insignificant chloride contents at depths below this level with values of 0.02 percent of binder

mass being recorded for both unloaded and preloaded SC-HyFRC at a depth of 63 mm (89 mm height in Figure 3-24). The chloride content profile of the preloaded SCC sample is likewise consistent with all depths of measurement displaying chloride contents in excess of 0.2 percent of binder mass. Interestingly, the chloride content is maximal at both the top and bottom surfaces while reaching a minimum at the mid height of the beam. This distribution might be caused by a combination of an accrual of bound chlorides in the top region nearest the ponding surface (which are released during the acid digestion) and an accumulation near the bottom surface brought about by ion transport depositing the chlorides as water is evaporated from the unsealed bottom face. For the specific unloaded SCC sample chosen for chloride content analysis, the resulting profile is in agreement with the electrochemical measurements, having a top bar undergoing active corrosion and a passive bottom bar. It is however worth noting that the depth to which the chloride content exceeds the ACI limit, 89 mm, does slightly exceed the depth illuminated by the colorimetric method suggesting that the rapid method may be slightly non-conservative. As it is also possible for there to be spatial variation of chloride migration between adjacent regions of the beam it is unclear whether this discrepancy could also be merely attributed to different sets of cores being used for each test procedure.

For both preloaded and unloaded beam core samples, corroded fibers were only uncovered from the 25 mm nearest the top and bottom faces of the beam regardless of chloride content profile (see the disparity in chloride contents at 13 and 140 mm heights of the unloaded and preloaded SC-HyFRC samples in Figure 3-24). Such behavior is inconsistent with the results of Mangat and Gurusamy (1988) and Balouch et al. (2010) who suggest that the critical chloride content threshold of fibers exceeds that of conventional steel rebar. Though the segmentation size did not allow for further differentiation of depth of fiber corrosion it is anecdotally noted that a strong correlation existed between carbonation depths and the occurrence of fiber corrosion. Such behavior may indicate that the local hydroxide content is rather the critical parameter responsible for providing the exceptional corrosion resistance exhibited by steel fibers in concrete. Interestingly, while the volume of fly ash included within the mixes studied here does not consume all of the portlandite, this could be a cause of concern in those concrete mixes which utilize high volume replacement of portland cement by SCMs to achieve a lower carbon footprint. Currently, there are no studies of which the author is aware that have looked specifically at corrosion of steel fiber reinforcement in a portlandite-free cementitious matrix.

Isolation of steel fiber corrosion to only limited areas at the extreme top and bottom of the reinforced concrete beam elements also helps to explain the flexural capacity retention exhibited by SC-HyFRC beams. With a large portion of the beam unaffected by fiber corrosion, a significant volume of fibers remained in place to deal with arresting flexural cracking under increasing load. From Figure 3-15 it is also worth noting that between the corrosion damaged samples, superior performance was measured for the preloaded sample set which simultaneously exhibited greater levels of corrosion activity. This contradictory phenomenon is explained by the nature of the bond existing between reinforcing steel and the surrounding concrete. Under normal conditions this interface typically has a more porous nature than the bulk concrete and thus has a limited frictional component to resist differential displacement occurring between steel and concrete owing to differences in elastic modulus during loading. Under light to moderate levels of corrosion attack, corresponding to rust production insufficient to produce splitting cracks, Al-Sulaimani et al. (1990) showed that this densification of the interface generated better bond behavior. Due to the crack resistance afforded by hybrid fiber reinforcement, the SC-HyFRC beams are able to withstand a greater degree of rust buildup at the interface without the

propagation of splitting cracks that form in comparable SCC beams and strengthen the interfacial bond by further densification. Thus to the extent that splitting cracks are controlled the continued corrosion of the reinforcing bar should not pose a serious threat to bond performance. At an undetermined future point (suggested by the results of the acceleration corrosion propagation tests), the continued corrosion of the reinforcing bar would produce enough expansion pressure to propagate splitting cracks far enough to lose overall bond performance in spite of the presence of fiber reinforcement but such a behavior was not observable within the scope of this investigation.

Lastly, following all other testing a destructive extraction of the reinforcing bars from the two concrete beams of each subcategory was carried out. The rust coating each bar was removed with a hexamethylenetetramine hydrochloric acid solution in addition to the removal of all protective layers of coating at each bar end. Subsequently the bare bar weights were compared to the original bar masses to determine corrosion mass loss (Table 3-7 and Figure 3-25).

Table 3-7 Reinforcing Bar Mass Loss of SCC and SC-HyFRC Beams, g

Beam Designation	Unloaded SCC		Preloaded SCC		Unloaded SC-HyFRC		Preloaded SC-HyFRC	
	Y*	Z	M	P*	AB*	U	I	T*
#3, top	7.9	4.2	5.7	12.4	0.5	1.7	3.5	0.7
#6, bottom	5.9	19.8	111.6	61.2	2.7	1.1	1.4	4.4

*Beam samples were also utilized for coring and may have suffered from minor abrasion of the #6 bar by the coring drill bit

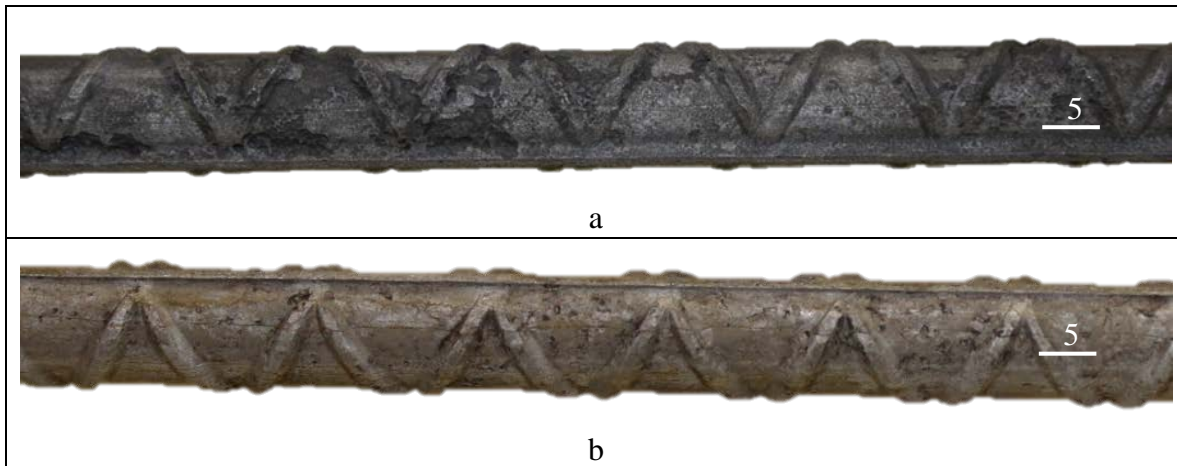


Figure 3-25 Reinforcing Bar Surfaces of Preloaded a) SCC and b) SC-HyFRC #3 Reinforcing Bars Following Acid Cleaning, mm

On comparison, it is immediately apparent that the external signs of distress exhibited by the SCC beams were strongly correlated with significant mass loss internally at the reinforcing bar. Those beams which suffered splitting crack damage incurred mass loss many times greater than

the SC-HyFRC samples for which no cracking was evident. Similarly, while there is some scatter in the overall mass losses experienced with the unloaded and preloaded SC-HyFRC reinforcing bars the relative magnitude is largely similar and in good correlation with the similar measurements of corrosion measured. Overall, the corrosion related mass losses of reinforcing steel provide still more evidence of the relative importance that fiber reinforced crack control can carry in determining the magnitude of corrosion damage.

3.6.2 Corrosion Propagation Testing Discussion

Despite the different testing procedures of conventional and accelerated corrosion propagation testing, strong similarities are evident when comparing the influence of hybrid fiber reinforcement in controlling the cracking and thus the propagation of corrosion in concrete. To understand the distribution of cracking within each concrete type, samples were saw cut at their mid height and photographed for comparison (Figure 3-26, Figure 3-27, Figure 3-28). In the process of cutting the SC-HyFRC sample shown in Figure 3-26 it was also noted that though fiber corrosion was evident on the cylinder surfaces, throughout the core of the samples no signs of fiber corrosion were evident in spite of the high chloride content throughout. Carbonation of the cylinder samples was not addressed but taking into account the length of time that the cylinders remained saturated it should be expected that the depth of carbonation was a few millimeters at most. Therefore the performance of the steel fibers with respect to direct corrosion is in agreement with the performance noted in the reinforced beam elements.

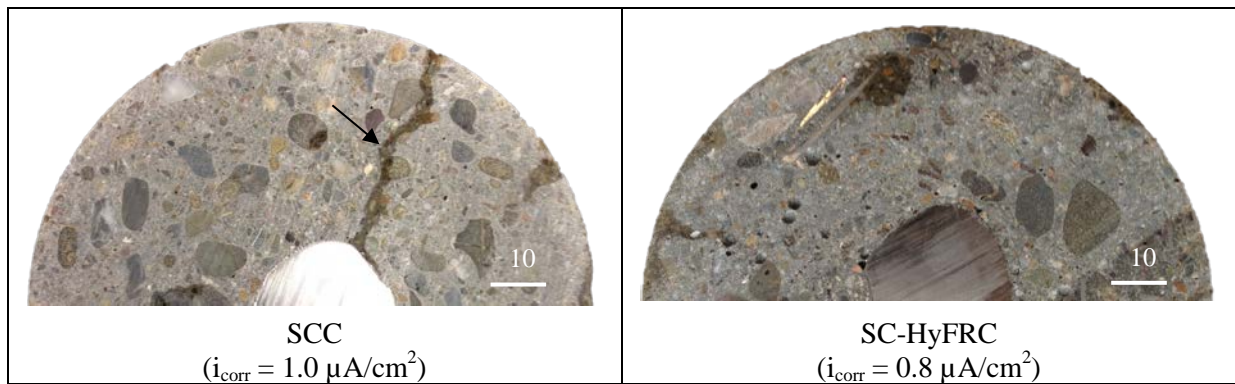


Figure 3-26 Crack Development in Conventional Corrosion Propagation Testing at 130 Weeks

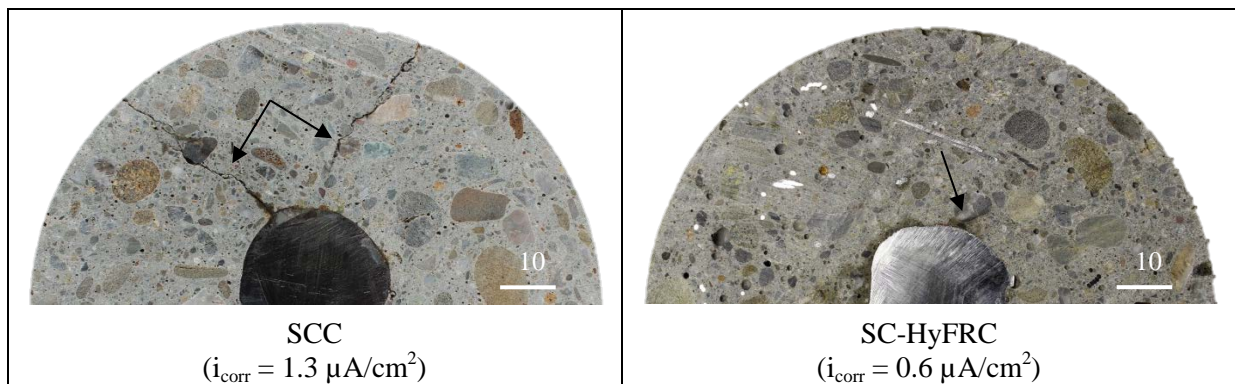


Figure 3-27 Crack Development in Accelerated Corrosion Propagation Testing, 1 Day of Current

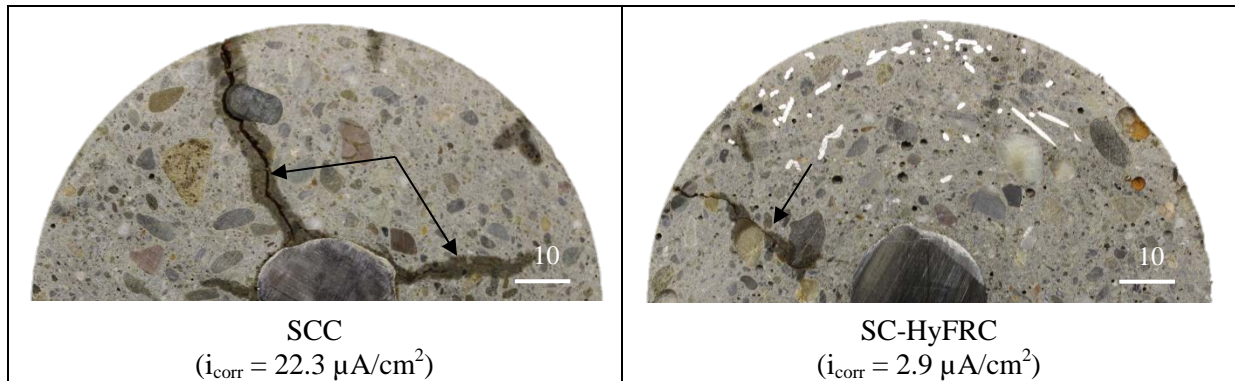


Figure 3-28 Crack Development in Accelerated Corrosion Propagation Testing, 2 Days of Current

Full depth cover cracking is notable on the SCC images of both Figure 3-26 and Figure 3-27, with a likewise similar magnitude of corrosion current density. Under more aggressive acceleration, as depicted in Figure 3-28, the corrosion induced cracking grows, allowing for greater reactant transport necessary for maintenance of a higher current density. In contrast, though they exhibit similar current density, no cracks emanating from the bar surface can be noted for the SC-HyFRC sample of Figure 3-26 while a small single crack extends 8 mm radially in Figure 3-27. While the images and correlated corrosion current densities depicted in Figure 3-26 appear to be in contrast with the results of the beam initiation testing, two factors must be considered which differentiate its response. First, within the corrosion initiation beam experiment the immediate divergence of cracked and uncracked samples can be attributed to the chloride migration dependence on depassivating the steel bar. In the conventional corrosion propagation cylinders, the chlorides are premixed into the fresh concrete so the onset of cracking does not bring about a sudden change in local chloride concentration. Second, as was experienced in the corrosion initiation beams, after corrosion initiated the corrosion rate remained steady beyond the first 40 weeks. The cracking observed in Figure 3-26 occurred 20 weeks prior to the information displayed, which possibly accounts for the relative dormancy. Cracking is undoubtedly critical with respect to aggravating corrosion rates but the sudden difference perceived in many experiments associated with chloride induced corrosion may be largely related to the impact of the initiation phase rather than the propagation phase. Differentiation associated with the propagation phase may take longer to establish as the crack growth (widening) rate may occur at a much slower pace than the radial propagation though it is still evident when taking into account the “long term” performance of SCC beams of Section 3.5.1 and the SCC cylinders of Figure 3-28.

Taking into account the actual conventional corrosion rates of the SCC and SC-HyFRC mixes were roughly half of those of Blunt (2008) due to the lower porosity brought about by both a lower water cement ratio and continued pozzolanic reaction of fly ash under saturated sample storage, it does seem within reason to state that the accelerated test method utilizing a current density of 1 mA/cm^2 does produce representative damage within either a plain or fiber reinforced concrete matrix.

Crack formation and associated i_{corr} values in Figure 3-26 and Figure 3-27 match well with the mechanism by which fiber crack control was thought to limit corrosion damage proposed but not experimentally observed by Blunt (2008) (Figure 3-29). With oxygen and moisture permeability so dependent on concrete permeability and by consequence the cracking behavior

of the concrete cover, the crack restraint observable even under more aggressive loading conditions (Figure 3-28) would provide a useful update to the graphical representation. Specifically that after forming cracks extending through the complete cover thickness, the crack opening dimension as a parameter is likewise associated with levels of reactant transport in excess of that described in Figure 3-29.

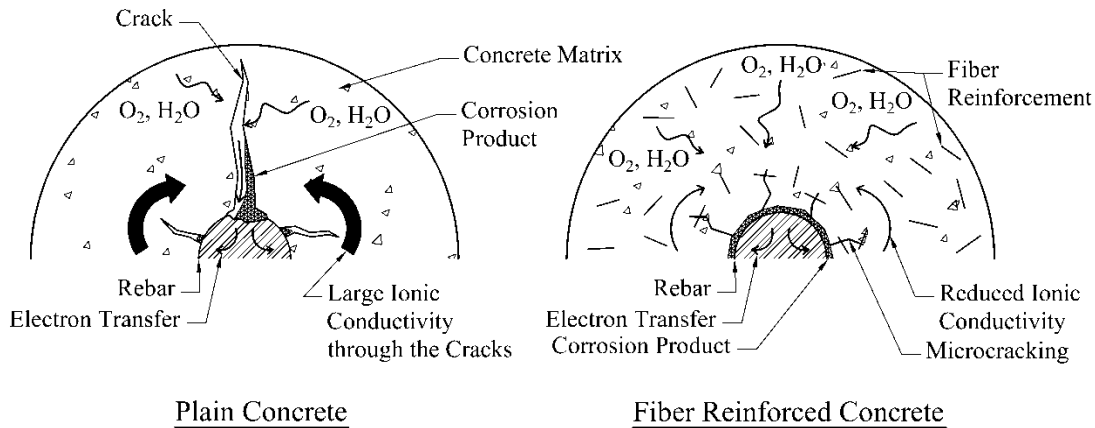


Figure 3-29 Proposed Mechanism of Corrosion Control through Fiber Crack Control of the Propagation Phase (after Blunt 2008)

For a more quantitative comparison of conventional and accelerated test performance, electric charge transfer can be used to provide a more direct measurement of iron oxidation. Integration of the current density time history of the conventional samples depicted in Figure 3-21 provides a measure of total charge transferred during the 130 weeks of testing equivalent to roughly 4600 coulombs for both SCC and SC-HyFRC samples. For the 1 day accelerated test program, the potentiostat delivers roughly 9600 coulombs to the system. From a charge comparison, the magnitude of this difference is then the reason for crack formations in the accelerated test that were not yet developed in the conventional propagation test samples. Similarly, the reinforcing bar mass losses can also provide a quantitative comparison of the different test procedures. Having extracted the reinforcing bars and cleaned them in the same manner described with the beam samples the resulting mass loss values are provided in Table 3-8 and Table 3-9. The conventional propagation cylinders match well with the predicted mass loss based on Faraday’s Law and because of their similar corrosion current time history display significantly similar levels of mass loss.

Table 3-8 Reinforcing Bar Mass Loss of SCC and SC-HyFRC Conventional Propagation Cylinders, g

Prediction ¹	SCC	SC-HyFRC
1.33	1.3 - 1.8	1.3 - 1.7

¹Based on Faraday’s Law and integration of corrosion current density time history (Figure 3-21)

Table 3-9 Reinforcing Bar Mass Loss of SCC and SC-HyFRC Accelerated Propagation Cylinders, g

	SCC-1	SCC-2	SC-HyFRC-1	SC-HyFRC-1
Actual	1.3	4.3	1.4	3.5

Prediction ¹	3.2	17.0	2.9	7.3
-------------------------	-----	------	-----	-----

¹Based on Faraday's Law and integration of applied current and corrosion current density time history (Figure 3-22)

Conversely, the predicted and actual mass losses of the accelerated propagation cylinders are wildly divergent. For most specimen types, the mass loss is roughly half of the predicted value while for the most extreme case the actual mass loss is one quarter the predicted value.

Drawing a conclusion that accelerated testing can produce meaningful interpretations of cracking potential of concrete mixes would appear to be valid, however it remains unclear whether predictive estimations should be made of issues such as composite capacity loss whereby steel mass loss in combination with concrete integrity are vital components. This uncertainty comes down to two primary components; 1) what is the actual efficiency of current applied during accelerated testing in oxidizing iron, and 2) what effect does the highly accelerated rate of iron dissolution have on the response of the surrounding concrete. Largely, the answer to both of these questions comes down to the degree of acceleration employed which is synonymous with the current density chosen. With respect to current efficiency, because the circuit is not free of resistance, to produce higher currents requires the application of larger voltages. This proves problematic due to the voltage range outside of which water will break down into oxygen or hydrogen gas. In such cases the efficiency of the applied current towards iron oxidation will be reduced and overestimate the gravimetric loss of the reinforcing steel as seems to be evident in Table 3-9. A second effect of artificially high current is the rate of iron dissolution into the interface layer surrounding the reinforcing bar. Under conventional conditions, these iron ions might be expected to quickly combine into iron oxides that generate expansive pressure at the interface. However, under conditions in which the interfacial solution is both saturated with iron ions and highly acidified (as a function of not having a locally counterbalancing cathodic reaction) it may be possible for some iron to migrate outward being both repelled by the positively charged bar surface and driven away by the concentration gradient. Should iron oxides form further within the layer of cover concrete the resulting expansion pressure generated at the steel interface will be reduced and change the concrete cracking behavior. In experimentation, one aspect of rust formation that differed between conventional and accelerated testing was the extrusion of rust through the cracks in accelerated tests to a degree not encountered under conventional testing implying a greater mobility. Similarly, as chlorides migrate towards the positive charge of the bar interface during the applied current test, their charge must be in a local sense balanced by an accumulation of protons leading to regions of acidification within the concrete. In such areas, a Pourbaix diagram would suggest the stable species of iron molecule may be changed and form different types of corrosion products with associated differences in volumetric expansion and thus cracking potential.

In combination, these issues would seem to make accelerated testing a potentially dangerous method from which long term projections can be made. Yet these issues of chemistry can be controlled and meaningful data collected under a still shortened time frame by careful consideration of current amplitude. With corrosion current densities within cracked concrete being measured as high as 22.3 and 58.6 $\mu\text{A}/\text{cm}^2$ for cylinder and beam tests within this study and published case studies reporting values as high as 100 $\mu\text{A}/\text{cm}^2$, a recommended level of current might be in the range of 200-300 $\mu\text{A}/\text{cm}^2$. At such levels, given the geometry of the samples the voltage necessary to produce the current would fall within an acceptable range. At the same time if total applied current durations were broken into shorter segments with "rest"

periods in between, concentration gradients would be allowed to normalize and lessen the impact on overall expansion behavior.

3.7 Conclusions

Hybrid fiber reinforcement provided by the SC-HyFRC material is proven to provide significant advantages to corrosion resistance. Experimentally this is shown by both corrosion initiation and corrosion propagation phase examination.

Corrosion initiation resistance is enhanced with SC-HyFRC by its capacity to withstand damage imposed by cyclical bending loads, while identical loading effectively eliminates the duration of the initiation phase in identical SCC samples due to flexural crack development. This cover concrete crack resistance is not confined merely to concrete bending loads but may also extend to issues such as salt scaling and frost action. Indirectly, SC-HyFRC also enhances corrosion initiation resistance of reinforcing layers away from the exposed surface by preventing the formation of splitting cracks from occurring that otherwise allow chloride migration to reach further depths.

Within the propagation phase of corrosion damage, crack resistance is strongly correlated with reduced corrosion activity and less deterioration of the steel to concrete interface. Even when surrounded by concrete contaminated with chloride ions and exhibiting similar corrosion potential as SCC beams, crack control at the reaction site by hybrid fiber reinforcement was responsible for an order of magnitude decrease in current density. Crack suppression as experienced within the reinforced SC-HyFRC beam samples ensures that the structural integrity of the concrete element to resist bending loads is maintained. Further, by preventing the formation of corrosion induced cracks, the rust formation that does occur is beneficial in densifying the porous interface between concrete and reinforcing bars and serves to enhance the bond behavior required for composite action during loading.

This issue of structural integrity is largely unaffected by steel fiber corrosion which is confined to only a depth within 10 mm of the exposed concrete faces in the duration of time investigated (2 years). As an aside, though the durability issue of carbonation was not directly addressed within this study, the results herein would seem to indicate that a more complete evaluation of the corrosion resistance of steel fibers within fully carbonated concrete should be investigated. From the standpoint of chloride induced corrosion, the steel fibers behave in a manner consistent with reported literature and because of the fiber hybridization and fiber volume provided within the SC-HyFRC matrix, sufficient undamaged fibers are at all times available to carry required loading.

To rapidly generate an assessment of corrosion cracking resistance the use of accelerated corrosion testing by means of applied current is validated in so far as it correctly produces the expansion necessary to induce damage at a similar scale as occurs during conventional corrosion propagation. There remain unanswered questions regarding the validity of using accelerated testing to produce charge specific levels of corrosion deterioration that can then be attributed to composite performance criteria such as bar pullout or flexural loading. However, it is suggested that provided current densities be limited to ranges consistent with field measured corrosion activity, it may be possible to produce representative deterioration at a rate of order(s) of magnitude greater than would occur naturally and thus can still prove effective for accelerated testing.

4 Alkali-Silica Reaction Damage Resistance

4.1 Introduction

Deterioration of concrete can also be attributed to the constituent materials of the concrete used in fabrication as is the case with Alkali-Aggregate Reaction (AAR) of which the subcategory of Alkali-Silica Reaction (ASR) is most prominent in the United States. The extent to which ASR can produce damage within concrete is determined by the mineralogy of the aggregates (coarse and fine) used in production as well as the alkali (typically sodium, Na, and potassium, K) content of the pore solution and the availability of moisture. When all criteria for damage are simultaneously met in a given concrete element, the resulting damage is observed as map cracking occurring across the exposed surface and general deterioration of concrete mechanical properties.

Historically, ASR damage has been identified as the root cause of structure deterioration since the 1940s, being first identified and reported in Southern California by T.E. Stanton (Stanton 1940) when investigating the unexpected deterioration of several concrete highway structures in Monterey and Los Angeles counties. Remarkably, even in the early stages of researching this problem, Stanton was able to correctly identify the concrete constituents responsible and suggested remedial actions that would prove successful. In the decades that followed, ASR was identified as causing deterioration of concrete structures worldwide.

To combat this problem, researchers have classified the mineral types that are susceptible to alkali-silica reaction (Table 4-1) and identified the rock types that would warrant additional testing prior to use. Currently, many Departments of Transportation at the state level maintain listings of quarry locations and associated ASR susceptibility to inform the public.

Table 4-1 ASR Associated Minerals (ranked from most to least deleterious, Thomas et al. 2013)

Opal
Tridymite
Cristobalite
Volcanic Glass
Cryptocrystalline (or microcrystalline) Quartz
Strained Quartz

Additionally, an alkali limit of 0.60 percent $\text{Na}_2\text{O}_{\text{eq}}$ ($\text{Na}_2\text{O} + 0.658 \cdot \text{K}_2\text{O}$) is imposed and standardized by ASTM C150 (2012) on portland cements when potentially reactive aggregates may be used, but has further been applied to commercially available portland cement within many states including California. Furthermore, the use of pozzolanic materials such as fly ash and granulated blast furnace slag as admixtures and for partial portland cement replacement has gained acceptance in modern concrete construction and contributed to the mitigation of ASR damage (Dunstan 1981, Shehata and Thomas 2000, Thomas 2011).

Nevertheless, the issue of ASR damage in concrete structures was not eradicated and persists even to this day with case studies of damage reported in most of the lower 48 states and spread across 50 countries. The continuation of this problem can most easily be associated with the regional availability or lack thereof of “good” aggregates. Due to transportation costs, it is often not financially feasible to ship aggregates long distances from quarries characterized by non-reactive minerals to construction sites resulting in the need to use whatever is locally available. Consequently, reactive aggregates are invariably used with demand further driven by the

diminishing supply of inert aggregates, having already been mined and utilized in past concrete. Many cases of ASR damage in recently constructed concrete can then be attributed to a lack of understanding by the concrete technician on the underlying chemistry of alkali-silica reaction and appropriate application of mitigation mechanisms.

In this void, the use of fiber reinforcement within the concrete for structural performance may be able to provide a safety net capable of arresting ASR before it can significantly damage the concrete should the more conventional mitigation methods be mistakenly used or overlooked entirely. As ASR is spatially associated with the aggregate constituents, one of the primary requirements of any mitigation mechanism must be the ability to be deployed in an equally spatially dispersed pattern. Secondly, because ASR damage is achieved through an expansive formation, a toughening mechanism of the cement matrix to localized tensile hoop stresses should be available. High performance fiber reinforcement in concrete is capable of meeting both of these criteria in addition to achieving its macroscale performance based objectives (deflection hardening, strain hardening).

4.2 Background

To generate ASR in concrete a structure must meet three necessary criteria which are; 1) the presence of a reactive aggregate, 2) the presence of unbound alkalis in the pore solution and 3) the presence of moisture. As mentioned earlier, the mineral types susceptible to reacting are fairly well qualified and detectable through methods such as petrographic examination. The commonality shared by all reactive mineral types is the lack of an ordered crystal structure of silica such as occurs in crystalline quartz. The local environment within concrete conventionally is a high pH solution established by the dissolution of sodium and potassium ions being available from portland cement clinker grains and balanced by hydroxyl ions (Glasser 1992). At the high pH (12-13) found in concrete pore solution, the siloxane bridges (Si-O-Si) of exposed silica constituents in the aggregate are broken with resulting silanol bonds (Si-OH...OH-Si) formed. Hydroxyl groups in solution are then able to react with the silanol bonds leaving exposed negatively charged Si-O⁻ sites. Reacting with positively charged cations present in the pore solution (Na⁺, K⁺), an alkali-silica gel is produced. In the case of disordered or low-density crystalline silica formations (Table 1), the available silica bonds to be attacked by hydroxyl ions are greatly increased due to the ability of ions to penetrate beyond the surface layer (Dent Glasser and Kataoka 1981), thus increasing the gel formation potential. The resulting gel having a composition of silica, alkali (Na, K) and calcium is deleterious because of its swelling potential when imbibing moisture from its surroundings. Such swelling can produce expansion pressures exceeding the tensile stress capacity of the aggregate and/or nearby cement matrix resulting in cracking. Such cracking can increase the exposed surface area of potentially reactive aggregate in addition to increasing the mobility of ion transport through the concrete thus extending the problem while simultaneously decreasing the soundness of the concrete to resisting other forms of loading, both environmental and mechanical.

Conventional mitigation to controlling the damage associated with ASR is achieved through the incorporation of supplementary cementitious materials (SCMs) into the binder content of new concrete. Even though such materials are characterized by potentially deleterious silica formations (silica fume) or additional alkali contribution (fly ash) such materials are experimentally proven to reduce the total amount of alkalis by increasing the overall alkali binding capacity (Thomas 2011). Pozzolanic reactions occurring between SCMs and portlandite are also responsible for strengthening/densifying the cement matrix and decreasing water mobility which may provide a secondary effect to limiting expansion. With the inclusion of

sufficient SCM in concrete, the expansion potential is limited to non-damaging states in which the soundness of the concrete can be maintained. It however must be noted that not all SCMs are equivalently effective, nor is a single content of inclusion sufficient for all aggregate types. In past studies with respect to SCM replacement level, the use of silica fume has been cited as most efficient followed by Class F fly ash, with slag and Class C fly ash interchangeable depending on alkali and calcium oxide contents (Duchesne and Berube 1994). More recently, with multi decade monitoring of ASR reactivity at research facilities across North America, there is a growing sense that some SCMs may be merely delaying the onset of damaging levels of expansion rather than eliminating them. Whether such behavior can bring about damage of SCM mitigated concrete is then dependent on the life expectancy of the structure, with those structures destined for century-plus levels of service being the most susceptible.

Several research groups have also approached the subject of controlling ASR expansion through confinement of the reaction product. While earlier research addressed the issue of actively applied stress (from pre-stressing or another external source) and its effect on ASR related expansion, Jones and Clark (1996) were some of the first to investigate the effect of passively applied stress, as a function of steel reinforcing ratio, with a predictable relationship developed between higher reinforcing ratios and improved expansion restraint. Limitations uncovered when depending on steel reinforcing bars to provide restraint included the lack of effect on the early microcracking stage of damage and the orientation dependency of restraint; i.e. no restraint was achieved in a direction perpendicular to the orientation of the reinforcing bar (Mohammed, Hamada and Yamaji 2003). These limitations highlight the need for dispersed, microscale, three dimensional confining capabilities in order to achieve adequate control over ASR expansion. Microfiber reinforcement was first employed successfully to meet these criteria by Turanli et al. (2001) with between one and seven percent volume fraction of steel microfibers in mortar bars fabricated with five percent opal substitution. Such mixtures were observed to restrain expansion potential with increasing effectiveness being obtained through a lengthened curing period. Subsequent work focused on the use of more conventional volume fractions of fiber reinforcement (both micro, 0.15 percent, and macro, 0.5 and 1.0 percent) by Haddad and Smadi (2004) in concrete fabricated with natural reactive aggregate and manufactured reactive particles exhibited less pronounced confining effects with fiber reinforcement performing worse with respect to expansion potential in all but the most reinforced (1 percent macrofiber) case. Andic et al. (2008) observed a likewise ineffective performance of microfiber reinforcement (0.1 to 3 percent) made of carbon, PVA and steel when following the conventional curing procedure of ASTM C1260 (2007) of one day in 80 °C water. However, when allowing for an extended curing duration thus producing an improved cement matrix to fiber bond capacity, fiber volume additions greater than one percent were effective at limiting expansion of a natural reactive aggregate. Burgher et al. (2008) found inconsistent behavior when investigating the incorporation of 0.5, 1.0 and 1.5 percent steel macrofibers in concrete fabricated with natural reactive aggregates and tested via ASTM C1293 (2008). Macrofiber reinforcement as low as 0.5 volume percent did prove effective at restricting expansion but the expected response of higher fiber volume fractions being more effective could not be replicated between subsequent mixes nor between different reactive aggregate types. Recently, Yazici (2012) and Hernandez-Cruz et al. (2014) have investigated one to two percent steel microfibers and one percent polypropylene microfibers respectively, with both achieving moderate success in restraining ASR expansion.

Perhaps the most complete evaluation of the mechanism through which fiber reinforcement can influence ASR gel formation beyond the issue of merely expansion constraint is reported by

Ostertag et al. (2007) in investigating heavily microfiber reinforced (seven volume percent steel microfiber) mortar bars fabricated around borosilicate glass rods acting as a reaction site. Under such a reinforcement scheme, the reactivity of the glass rod was reported to be decreased as measured by diameter loss over time with the expansive pressure producing less cracking around the rod perimeter. Consequently, the gel elemental concentrations in the confined case were higher than in the control leading to a greater gel viscosity. Correlating glass rod dissolution (diameter loss) with gel concentration implies that the mechanical confinement afforded by fiber reinforcement has an additional effect of creating a chemical deterrent to continued silica dissolution due to the already present high concentration in the surrounding gel. Whether such an effect can be likewise produced with less fiber reinforcement or with natural reactive aggregates remains unclear due to the extreme difficulty encountered with in situ gel extraction.

At the structural level, the importance of ASR deterioration lies in the impact it can have on the mechanical properties of concrete. In conventional concrete these properties typically are the strength (f'_c) and the elastic modulus (E) from which an ability to meet performance criteria can be judged. Commonly, it is the value of elastic modulus which first exhibits distress and signals the possibility of ASR damage. With natural reactive aggregates observed to undergo internal cracking due to gel swelling as a precursor to microcracks forming in the surrounding cement paste, it is believed that the composite stiffness of concrete (cement paste plus aggregate) is more sensitive than the compressive strength which for normal strength concrete typically is more dependent upon the cement paste and internal void structure. Indeed, this earlier sensitivity in elastic modulus is observed experimentally (Pleau et al. 1989, Multon et al. 2005) while severe cases of ASR concrete distress are deleterious to both stiffness and strength (Swamy and Al-Asali 1988, Ahmed et al. 2003). Prior research has not illuminated the extent to which fiber reinforcement may successfully contain internal aggregate cracking (with opal aggregate experiments limited to investigating surface reactivity expansion effects) but it is expected that the crack resistance observed under other types of loading can be extrapolated to providing a strong matrix crack resistance enhancement. On the scale of mortar bars, the residual capacity of fiber reinforcement pre-engaged by ASR expansion to subsequent mechanical loading through bending has been investigated by Yi and Ostertag (2005) and Yazici (2012) with steel microfiber reinforcement in dosages ranging between 1 and 7 volume percent. In contrast to samples having no fiber reinforcement, the steel microfiber mixtures of both experimental programs were observed to maintain peak flexural load capacity and toughness after significant ASR exposure. There has been no work previously conducted specifically focused on the residual flexural capacity of fiber reinforced concrete (macrofibers/hybrid fibers with reactive coarse aggregates).

4.3 Test Methods

4.3.1 ASR Expansion Testing Methods

The field of alkali-silica reaction has been well studied since the 1940s when it was first acknowledged by Professor Stanton. Extensive testing has been performed to both survey aggregate inventories in order to identify sources which are more likely to contain potentially susceptible quantities of non-crystalline silica and determine mitigation and remedial actions. Through time, testing procedures have slowly evolved to meet the demands of industry needs for speed and accuracy, although it would be fair to characterize existing testing methodologies as a work in progress. At present, testing in the United States is conducted by primarily 2 methods outlined in ASTM C1260 (Accelerated Mortar Bar Test, AMBT) and ASTM C1293 (Concrete Prism Test, CPT).

For industrial purposes, in which limited time is made available for testing prior to construction phase, the AMBT protocol has become the fashionable choice. The benefits afforded-by and popularity-of utilizing the AMBT test are primarily based on speed. Complete testing can be achieved in roughly 2 weeks (16 days) from the point of fabricating samples, with results that are in the majority of aggregate types, accurate enough to project realistic behavior. With this speed, multiple variants of aggregate types and/or mitigation techniques can be tested within an acceptable time frame. However, with the increased level of reaction acceleration there are shortcomings in meeting performance criteria. Recent research (Drimalas et al. 2014) has identified specific classes of aggregate in which the AMBT test cannot capture detrimental levels of behavior, but nevertheless long term analysis of concrete containing such aggregates does show signs of suffering alkali-silica distress. Moreover, the experimental conditions of the AMBT test may also incorrectly adjust the response behavior of some mixes incorporating pozzolanic materials which are used as for mitigation. Because performance of the AMBT procedure is measured as cumulative expansion of a specimen, and expansion levels are highly influenced by cracking and swelling, it should be realized that the intrinsic tensile strength of the specimen (its ability to resist expansive pressures with minimal straining/cracking) is a key factor in determining successful performance. In mortar mixes which engage pozzolanic materials, such as fly ash, as a mitigation for overall expansion it is expected that soaking in high temperature (80 C) sodium hydroxide solution is likely to simultaneously accelerate not only the alkali silica reaction of interest but also the hydration reaction and by association the strength gain and densification of the surrounding mortar matrix. Unless these two effects can be decoupled it is important to realize that expansion suppression may be artificially restrained in part by a reduced alkali permeability and an over-strengthened matrix.

In contrast with the extreme levels of acceleration achieved in the AMBT test, the CPT is widely considered an improved response characterization with respect to in situ response. The alkali supply in relation to demand is not held at near “endless” as is the case with soaking in 1M NaOH solution, rather alkali levels are dictated as a percentage of total cementitious mass (1.25 percent total alkalis ($\text{Na}_2\text{O}_{\text{eq}}$) by mass of cement). Limiting the availability of alkalis to the reaction sites is more representative of conditions in which free alkalis in the concrete are depleted and ingress from environmental sources is limited by transport properties. The temperature to achieve acceleration is lowered to 38 °C which is in much closer agreement to environmental conditions that may be encountered. The time scale of the CPT test while longer than the AMBT test still provides a projection of expansion levels within a one to two year timeframe. Unfortunately, this may prove insufficient to field testing of materials on a construction schedule but can provide meaningful contributions through state and federal laboratories with alkali silica reaction investigations.

Beyond the conditioning differences of the AMBT and CPT tests, when investigating the influence of fiber reinforcement on ASR it is also worth noting that their standard sample geometries impact the size of fibers which may be considered. Having a smaller cross section, the AMBT test is inefficient in testing the true response of macrofiber reinforcement because the degree of fiber alignment along the longitudinal direction is exaggerated far beyond what would be achievable in a large scale element. In doing so, the fiber contribution to constraining length expansion would be overestimated. Therefore, the experimentation described herein restricts fiber reinforcement evaluation to microfibers with AMBT testing, while CPT testing is conducted on fiber hybridizations like those described in Chapter 2.

Ultimately, there is no better reference source than non-accelerated samples or samples in which the conditional differences between field structures and the samples themselves are kept to a minimum. Long term studies (decade scale), such as those currently ongoing at institutional laboratories in Canada and the US provide data for true long term projections. Though the extended timeframe proves of limited use in impacting decisions that must be made in the here and now, the data collected provides insight into the expansion behavior not captured by accelerated testing.

4.3.2 ASR Mechanical Property Testing Methods

Mechanical property (f'_c , E, flexural toughness) testing is carried out in the same manner as would be conducted for standard non-distressed concrete.

For long term testing (CPT conditioning), strength and elastic modulus values are gathered from 100 mm diameter by 200 mm height standard cylinder samples at the beginning, middle and end of the prism expansion test durations. For evaluation of incurred damage, the middle and end readings are compared to the initial 28 day old values. Tests are performed on a 1330 kN SaTEC hydraulic compression machine with displacements captured by two LVDTs connected to opposing faces of aluminum collars connected to the cylinders through pin supports. Likewise, flexural toughness is tested by 4 point bending tests on samples having identical geometry as the expansion prisms (76 mm square cross sections) using a 225 mm beam span length. Load is applied by a variable load (530 kN maximum capacity) Universal Testing Machine (UTM) to a midpoint deflection greater than the span length divided by 150. Mid-span, mid-height displacement is continuously measured by LVDTs attached to a bending yoke on either side of the flexural sample.

For short term testing (AMBT conditioning), due to storage limitations (both in soaking solution and oven space) strength testing is determined by cube samples having a 50 mm side length. Flexural response was measured of the same samples used for expansion monitoring, with three mortar bars sacrificed from the expansion set for each measurement (initial, intermediate and final). Testing of the 25 mm square cross section mortar bars was carried out on a 110 kN MTS test frame through 4-point bending with a beam span length of 225 mm. Mid-span displacements were continuously measured by a single LVDT in contact with the bottom (tension) face of the mortar bar until either the mid-span deflection exceeded the span length divided by 150 or the load resistance dropped to zero. Elastic modulus of AMBT conditioned samples was not tested directly, though it can be back calculated from the elastic response (flexural stiffness) of the flexural samples but is not included within the scope of this work.

For both types of testing, the conditioning of mechanical property samples is consistent with their expansion counterparts. As such, it is worth noting that the cement hydration is accelerated and not fully representative of the strength of the same mixtures having been cured in a conventional manner. Likewise, the pozzolanic reaction occurring in mixtures containing fly ash must be assumed to have been accelerated by the elevated temperature storage and do not display the early age strength development retardation normally associated with cement replacement.

4.4 Materials

4.4.1 Reactive Aggregate Materials

As the primary point of interest in testing for alkali silica reaction was to identify the impact of fiber reinforcement on expansive concretes, suitable aggregates were chosen based upon exhibiting high reactivity in previously published studies. Selection of reactive aggregate was

also made to include both a coarse and a fine reactive aggregate to include in the study. This allowed for testing of both AMBT and CPT testing of the same aggregate albeit with the need for modification by means of crushing the coarse aggregate for mortar testing. The reactive coarse aggregate of choice is obtained from the Spratt Quarry in Stittsville, Ontario and stockpiled by the Ontario Ministry of Transportation. The reactive fine aggregates chosen were obtained from the Robstown Quarry in Robstown, Texas and manufactured by Wright Materials Inc. and the Pleasanton Quarry in Pleasanton, California and manufactured by Vulcan Materials Company. Herein, these aggregates will commonly be referred to as the “Spratt aggregate”, “Wright aggregate” and “Vulcan aggregate” based upon their quarry and manufacturer. Petrographic analysis of these aggregates has identified them as having sufficient non-crystalline silica formations to be susceptible to alkali silica reaction (Table 4-2).

Table 4-2 Petrographic Classification of Reactive Aggregates

Aggregate	Mineralogy	Deleterious Constituents
Spratt	Dolomitic Limestone	Opal, Chalcedony
Wright	Mixed Quartz/Chert	Volcanic Glass, Opal, Strained Quartz
Vulcan	Graywacke	Volcanic Glass, Strained Quartz

Upon receipt of the aggregates to the testing concrete laboratory of UC Berkeley, the properties relevant to inclusion in the proposed alkali silica expansion testing were established following ASTM testing procedures. These tests included analysis of the specific gravity, the absorption capacity and particle size analysis. The Spratt coarse aggregate was received as 19 mm Maximum Size Aggregate (MSA) particles which required crushing to produce the desired 9 mm MSA gravel for concrete and further crushing to meet the gradation specifications of ASTM C1260 for fine aggregate. Aggregates were washed and crushed using a Massco Crusher and a Type UA Braun Pulverizer when finer particles were desired. For determination of the absorption capacity a representative sample of each aggregate was submerged and allowed to fully saturate over night after which the sample was allowed to air dry with periodic stirring, to achieve a homogenous moisture distribution, until a mini slump test no longer retained its conical shape in accordance with ASTM C128 (2012) chapter 8. From this sample a portion was removed to oven dry at 105 °C and other samples were removed for determination of specific gravity by following both the gravimetric (chapter 9.2) and the volumetric (chapter 9.3) procedures. Oven-dried samples were weighed for moisture loss to determine absorption capacity while pycnometer and Le Chatelier flask readings were compared to determine appropriate specific gravity values (Table 4-3).

Table 4-3 Aggregate Properties Determined by ASTM C127/128 and Fineness Modulus

Coarse Aggregate	Absorption Capacity (%)	Specific Gravity	MSA (mm)
Crushed Spratt Gravel	0.7	2.68	9

Fine Aggregate	Absorption Capacity (%)	Specific Gravity	Fineness Modulus
Crushed Spratt Sand	1.5	2.69	2.9
Wright Sand	0.7	2.62	2.6
Vulcan Sand	1.6	2.66	3.2

Particle size distribution analysis was conducted in accordance with ASTM C136 (2006) upon a standardized sieve tower. Analysis of mass retention upon the various mesh sizes is tabulated and presented graphically as a gradation curve. Fineness modulus is calculated as the summation of cumulative retention rates upon each mesh opening size up to and including the #100 sieve (opening size of 0.15 mm). The determined fineness modulus of Wright Sand, 2.6, is representative of a gradation more heavily weighted towards smaller grain sizes, that would fall just barely under the range associated with ASTM C33 (2013).

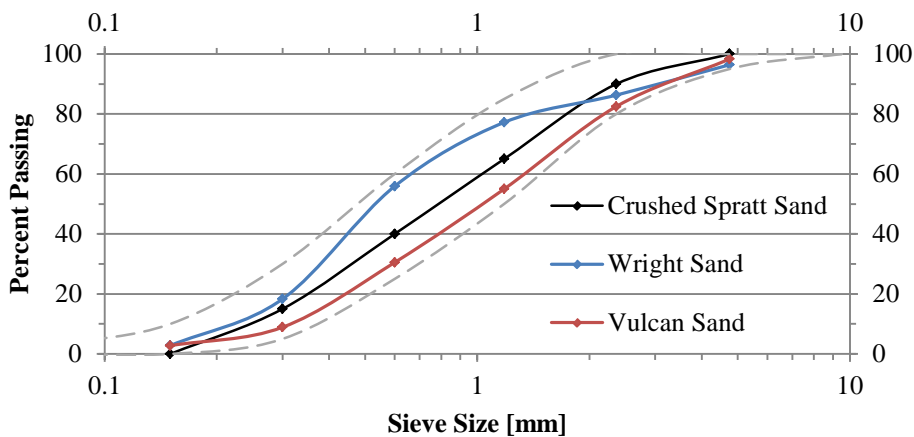


Figure 4-1 Fine Aggregate Gradation with ASTM C33 Limits Shown as Dashed Lines

For Wright aggregate in particular, the retained mass which passes the #30 sieve but is retained on the #50 sieve is in excess of a standard gradation and is compensated for by lacking larger particle proportioning. In comparison, Vulcan Sand, used for general purpose concrete testing in the UC Berkeley concrete laboratory is presented along with the gradation limits imposed by ASTM C33 (Figure 4-1). As evidenced by the gradation curves, the scale on which the Wright aggregate deviates from the desired gradation is still within the bounds of ASTM C33 and as such was determined to be of suitable use for testing. The Crushed Spratt Sand gradation, having been prepared specifically for ASTM C1260 testing, exactly matches the standard gradation.

Petrographic analysis of each reactive aggregate type was performed with a specific focus on identifying the reactive potential at each gradation. Table 4-4 presents the mass percent at a given gradation of each aggregate type which displayed a constituent known to be deleterious and therefore classified as potentially reactive. It is important to realize that the values in Table 4-4 have limited bearing on the actual material that is utilized in concrete without knowing the

gradation of the aggregate placed in concrete, so although 67 percent of the #4 particles in the Wright sand are deleterious there are in actuality few of those particles incorporated into cementitious composites. The physical appearance of the aggregate and its inclusion can be observed in Figure 4-2, comparing the differences in aggregate at the #30 sieve size.

Table 4-4 Aggregate Mass Percent Reactive by Particle Size

	#4 (4.75 mm)	#8 (2.36 mm)	#16 (1.18 mm)	#30 (0.60 mm)	#50 (0.30 mm)	#100 (0.15 mm)
Spratt	-	9.49	8.02	18.38	14.35	32.72
Wright	67.30	74.86	34.86	25.47	22.66	15.85
Vulcan	5.13	2.73	0.71	35.15	25.89	19.79

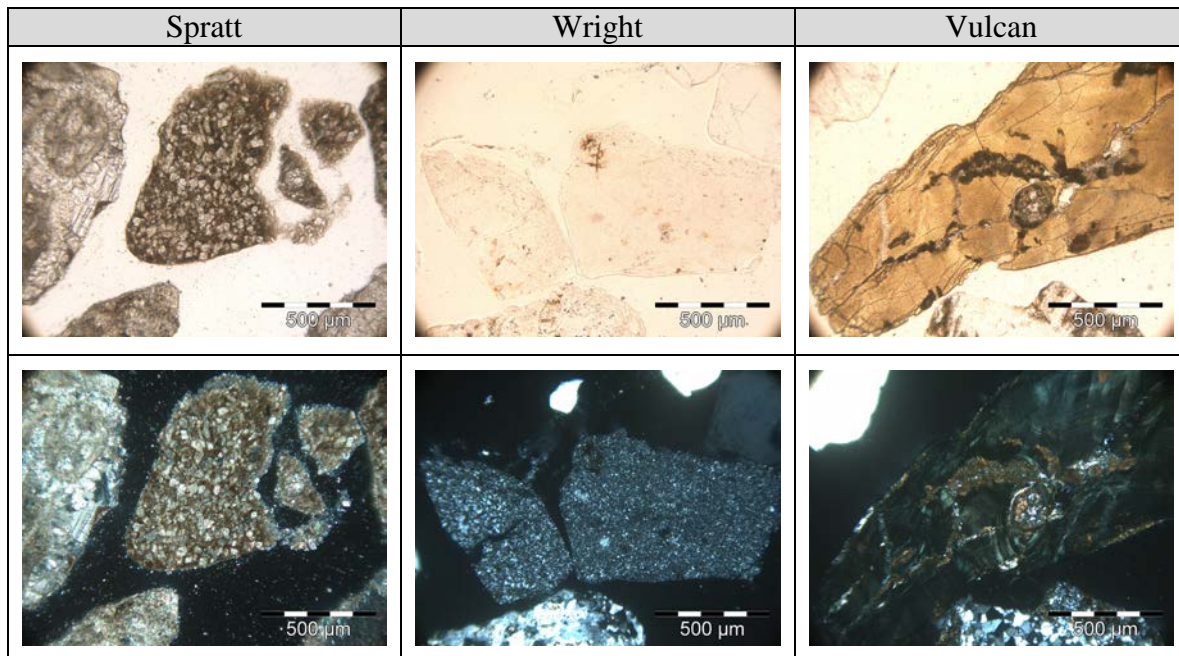


Figure 4-2 Photomicrographs of #30 Aggregate Particles, Plane Polarized (top row) and Cross Polarized Light (bottom row)

For example, though Table 4-4 lists 74.86 percent of all Wright #8 sized particles as being potentially reactive, that particle size comprises only 10.10 percent of the total aggregate mass. Therefore under its natural gradation, the reactive #8 particles in Wright sand account for only 7.56 percent of the total aggregate mass. Similar calculations based upon the manufactured gradation of crushed Spratt and the “as-received” gradations of Wright and Vulcan sands are tabulated in Table 4-5.

Table 4-5 Reactive Mass (Percent of Total Mass) Distribution by Particle Size in Natural Gradation

	#4	#8	#16	#30	#50	#100
Spratt	-	0.95	2.01	4.59	3.59	4.91
Wright	2.42	7.56	3.17	5.42	8.52	2.46
Vulcan	0.09	0.43	0.20	8.61	5.59	1.21

Of particular note, the summation of potentially reactive aggregate masses (summing each row of Table 4-5) is 16, 30 and 16 percent for Spratt, Wright and Vulcan sands respectively. Modifying the gradations to meet the criteria of ASTM C260, the potentially reactive aggregate mass sums would change to 16, 31 and 19 percent for Spratt, Wright and Vulcan sands respectively. Interpretation of these values must be accompanied by an understanding that the reactive component is not necessarily the same for each aggregate type at each particle size and thus total expansion potential is not automatically correlated with summation of potentially reactive aggregate mass.

4.4.2 Cementitious Materials

The matrix within which the aggregates and fiber reinforcement were tested was a composite of portland cement (PC) and for select mixtures Class F fly ash. The chemical composition of each cementitious component was measured by XRF analysis and presented in Table 4-6.

Table 4-6 Chemical Composition of Cementitious Components

	Quickcrete Type I/II P.C.	Lehigh High-Alkali Type I P.C.	Class F Fly Ash
SiO ₂	20.36	18.68	60.40
TiO ₂	0.22	0.23	0.97
Al ₂ O ₃	3.66	5.38	16.80
FeO	3.09	1.89	4.27
MnO	0.06	0.05	0.04
MgO	4.14	2.33	2.19
CaO	61.08	61.61	7.07
Na ₂ O	0.22	0.26	3.33
K ₂ O	0.53	1.28	1.23
P ₂ O ₅	0.08	0.25	0.45
LOI (%)	1.23	2.89	1.47

Of specific interest in comparing the two portland cement types is the total alkali content, Na₂O_{eq}. The commercial Type I/II blend, used when an alternative alkali source is provided as in the case of the AMBT test protocol, has a total alkali content of 0.60 percent equivalent to the limit imposed by ASTM C150. The high alkali Type I cement utilized in ASTM C1293 testing is calculated to have a total alkali content of 1.10 percent. The fly ash has a low (<8 percent) calcium oxide content and relatively high silicon oxide, aluminum oxide and iron oxide contents (sum greater than 70 percent) characterizing it as Class F and well suited for ASR mitigation but does contain 4.14 percent Na₂O_{eq} which would seem counterintuitive for preventing ASR. While the extent to which this Na₂O_{eq} content was soluble was not investigated, conventional assumptions are that the alkali content of fly ash is bound and therefore does not participate in the alkali-silica reaction process.

4.5 Test Procedures

4.5.1 AMBT Testing Procedure

For samples to be tested by the ASTM C1260 procedure, mix proportioning was consistent with 1.00:2.25:0.47 (ratio of cement, fine aggregate, water by mass) in accordance with the

standard. Since no minimum alkali content of the cement is imposed as alkali supply is maintained by the storage solution, Type I/II portland cement was used for all mortar bars. Fiber reinforcement was provided by Nycon polyvinyl alcohol (PVA) microfibers previously described. Fiber volume within the mortar was discounted from the volume allotted to the fine aggregate. While a decrease in aggregate may be suggestive of a decrease in overall reactivity, the comparable amounts of aggregate when using fiber volumes of less than 1 percent is deemed insufficient to account for any change in measured expansion. Indeed, with one volume percent of fibers the mix proportioning only changed to be 1.00:2.21:0.47:0.02 by mass of cement, fine aggregate, water and PVA fiber respectively which is less than a 2 percent change in aggregate content. Fiber reinforcement was limited to the PVA type fibers due to the sample size. Expectations of forced alignment of the steel fibers within molds with a cross section of 2.54 by 2.54 cm would not allow for deterministic evaluation with respect to projecting their efficiency in larger elements in which randomized orientation is typically achieved. Fiber contents of 0.2 and 1.0 percent of total volume were used to study the restrictive ability that fibers might impart on the cementitious matrix surrounding reactive silica sites of the Wright aggregate. Subsequent analysis of PVA microfiber reinforcement focused solely on the influence of 1.0 volume percent with respect to expansion of Spratt, Vulcan and aggregate mixtures. Wright fine aggregate was tested both when re-graded to meet the size specifications of ASTM C1260 and its natural, as-received gradation. Additionally, a single batch of samples was prepared with 50 percent portland cement replacement by fly ash, both as mortar and with 0.2 volume percent fiber reinforcement, for comparison to and in conjunction with conventional mitigation.

Mixing was performed in single batches for each mixture type (unreinforced, 0.2 percent PVA and 1.0 percent PVA) for quantities sufficient to fabricate a minimum of three specimens of dimensions 25.4 mm by 25.4 mm by 285 mm. Each sample was cast with expansion stubs embedded at the center of each end face for use in measuring specimen expansion. The expansion stubs, sold by Humboldt Mfg., were positioned such that the average distance between embedded stub ends was roughly 255 mm (Figure 4-3). For each mixture type a vibration table was utilized to achieve consolidation with the duration of vibration necessary being greater for increasing fiber volume.

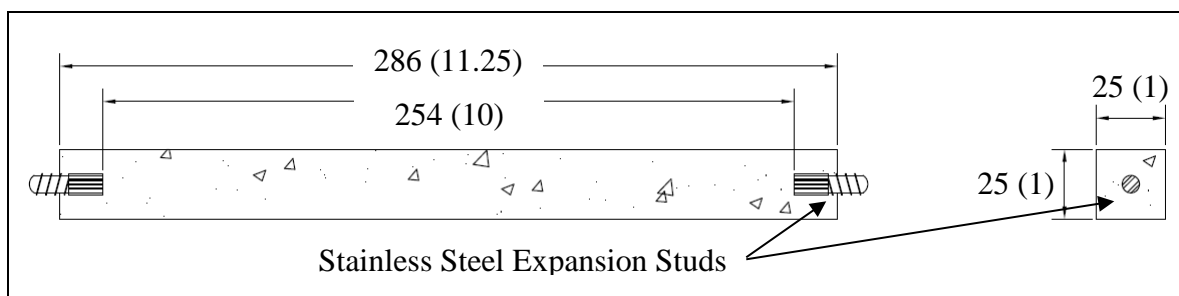


Figure 4-3 Mortar Bar Test Specimen Dimensions, mm (inches)

Following casting, samples were covered and placed within a fog chamber for 24 hours of curing at 23 °C and 98 percent relative humidity. After 24 hours all samples were demolded and placed in a water bath which increased from room temperature up to 80 °C for additional curing. While the standard procedure called for a single 24 hour period of water bath curing, the experimental procedure allowed for 48 hours of water batch curing. This discrepancy is made to achieve a strengthened matrix-fiber interface/bond as was noted by previous researchers (Turanli et al. 2001, Andic et al. 2008) to be a necessary condition for effective fiber restraint. Expansion

samples were removed from the water bath and measured relative to a comparator bar to determine length measurements prior to alkali silica reaction initiation. Subsequent readings of length were compared relative to this initial “zero” reading to determine sample expansion. As soon as each sample was measured they were immersed in preheated 1N sodium hydroxide solution and returned to the heating chamber for a maintained 80 °C environment to instigate accelerated testing. Daily readings of the each sample were conducted for the next 14 days, with expansion determined as the change in length divided by the initial length between the expansion stub ends (255 mm).

For samples fabricated for flexural testing, an initial set of three samples were sacrificed after the water curing for flexural testing and determining a benchmark performance as uncracked samples. At the midway point of accelerated testing (7 days), a second set of three designated bars was removed and tested. Finally at the conclusion of the accelerated regime, those samples remaining were tested for flexural response.

Table 4-7 AMBT Test Parameter Grid¹

	Wright	Spratt	Vulcan
ASTM C1260 gradation (2-day/4-day H ₂ O)	X/-	X/X	-/-
As-received gradation (2-day H ₂ O)	X	-	X
Flexural Testing (pure cement/50% fly ash)	X/X	-/-	-/-

¹Each checked box represents an ASR expansion experiment conducted comparing mortars with and without PVA microfiber reinforcement

4.5.2 CPT Testing Procedure

For samples to be tested by the ASTM C1293 procedure, the Wright fine aggregate and the crushed Spratt coarse aggregate are tested for expansive capability. In the case of testing a reactive fine aggregate, an inert pea gravel source, maximum size aggregate of 9 mm, was used for concrete production. When testing a reactive coarse aggregate, the Vulcan fine aggregate was used for concrete production. Contrary to AMBT samples, in which alkalis levels are elevated by the immersion solution, alkali requirements to generate accelerated levels of expansion in CPT samples are met by using high alkali cement and supplemented by sodium hydroxide. High alkali cement for this study was provided by the Lehigh Cement Company. The Type I portland cement was measured to have a total alkali content of 1.10 percent by X-Ray Fluorescence (XRF) analysis. To achieve the prescribed level of alkali loading (1.25 percent by mass of cement) sodium hydroxide was dissolved into the concrete mixing water to ensure dispersion within the concrete. Fiber reinforcement was provided by a hybrid blend consisting of Nycon PVA fibers and two Bekaert steel fibers. While steel fibers were eliminated due to size restrictions in the mortar bar testing, their use in the concrete prism testing was allowed because the sample dimensions were 76 mm by 76 mm by 285 mm. With steel fibers of length 30 mm and 60 mm, some alignment with the sample faces is expected but internal fiber distribution is expected to remain fairly randomized.

The issue of aggregate proportioning, the ratio between coarse and fine aggregate content, was encountered because of the difference in the mix proportions outlined in ASTM C1293 and

the Hybrid Fiber Reinforced Concrete (HyFRC) proportioning designed to maximize the utility of the included fiber reinforcement without sacrificing concrete workability. Specifically, these differences included an increase in water content (and by result the water/cement ratio) and an increase in the fine aggregate content with a corresponding decrease in the coarse aggregate content. Depending on whether testing for a reactive coarse or reactive fine aggregate, an increase of the reactive silica component per unit volume of concrete might be anticipated to generate a proportional increase in total expansion. However, it is important to point out that while the phenomena of alkali-silica reaction can happen when minimum thresholds of reactive silica, high alkali content and moisture are simultaneously present, the reaction rate and corresponding expansion rate is maximized at carefully balanced conditions. Graphically this can be observed as the “pessimum” effect in which expansion as a function of alkali content or of silica content appears as an inverted parabola. Maximal expansion is achieved in conditions when neither amorphous silica or alkali content are exhausted nor over saturated at which point transport properties of the concrete matrix prove to be a limiting factor.

With respect to fiber reinforcement, resolution of this issue was achieved by testing the early age flexural response of 76 mm by 76 mm by 286 mm prisms having the hybrid fiber blend in aggregate ratios, 1.09:1.00 and 0.49:1.00 (fine to coarse) for HyFRC and ASTM C1293 respectively. Load-deflection responses (Figure 4-4) can be used to gauge whether the high coarse aggregate content adversely affects the ability of fiber reinforcement to produce the characteristic deflection hardening behavior deemed necessary to meet performance objectives.

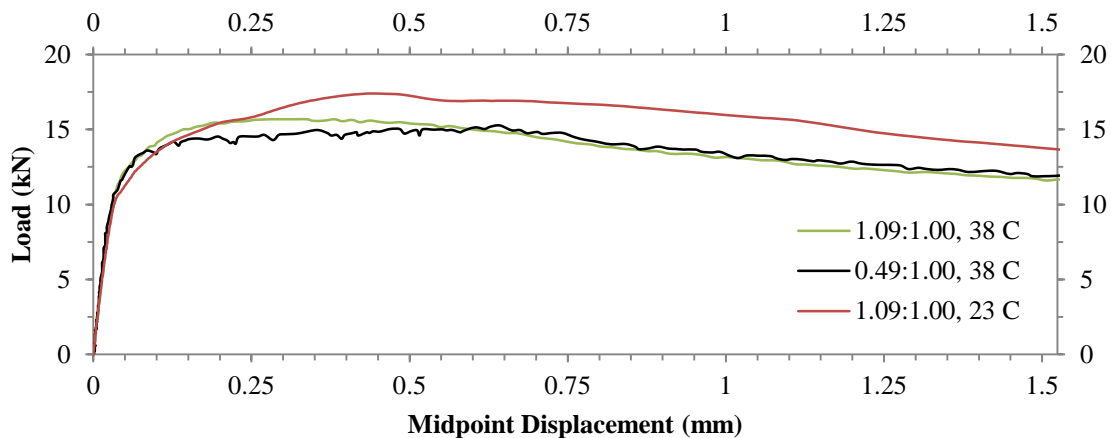


Figure 4-4 Influence of Fine to Coarse Aggregate Content Ratio and Curing Temperature on the Load Deflection Behavior of Hybrid Fiber Reinforced Concrete

Performance between 76 mm square cross section samples having a span length of 225 mm is deemed similar enough regardless of aggregate content ratio (curve “1.09:1.00, 38 C” versus curve “0.49:1.00, 38 C”) that testing proceeded.

Similar to the AMBT parameter investigation, the combined influence of conventional mitigation (SCM addition) with hybrid fiber reinforcement was also included in the project testing protocol. For the CPT test this was done by testing the performance of the Self-Consolidating Hybrid Fiber Reinforced Concrete (SC-HyFRC) mix, having 25 percent fly ash replacement of portland cement and a total fiber volume of 1.5 percent. Because the cementitious content and the aggregate content ratios are further changed in order to achieve self-

consolidating properties a control mix having the same binder content but with no cement substitution is also included. The consequence of fly ash inclusion in this third set of samples with respect to total alkali loading provides an interesting comparison to conventional concrete mixes and should clarify the role of fly ash alkali contribution to ASR reactivity (Table 4-8).

Table 4-8 Alkali and Wright Aggregate Component Content in Fine Aggregate CPT Tests (kg/yd³)

	Alkali Loading (1.25% Cement)	Alkalis in Fly Ash	Reactive Fine Aggregate Content
ASTM C1293 ¹	5.25	0.0	561
HyFRC ¹	5.29	0.0	842
SCC	6.84	0.0	1073
SCC (25% Fly Ash)	4.97	5.59	1073
SC-HyFRC	4.97	5.59	1044

¹Mixes tested with and without hybrid fiber reinforcement

Casting of each concrete mix included 76 mm by 76 mm by 285 mm expansion prisms and 100 mm diameter by 200 mm tall cylinders, with additional prisms cast for intermediate testing of flexural response for the ASTM C1293 mixtures. Each prism designated for expansion includes stainless steel stubs, required for length measurements, embedded within the center face of each end and having an average spacing between stub embedded ends equal to 255 mm (Figure 4-5).

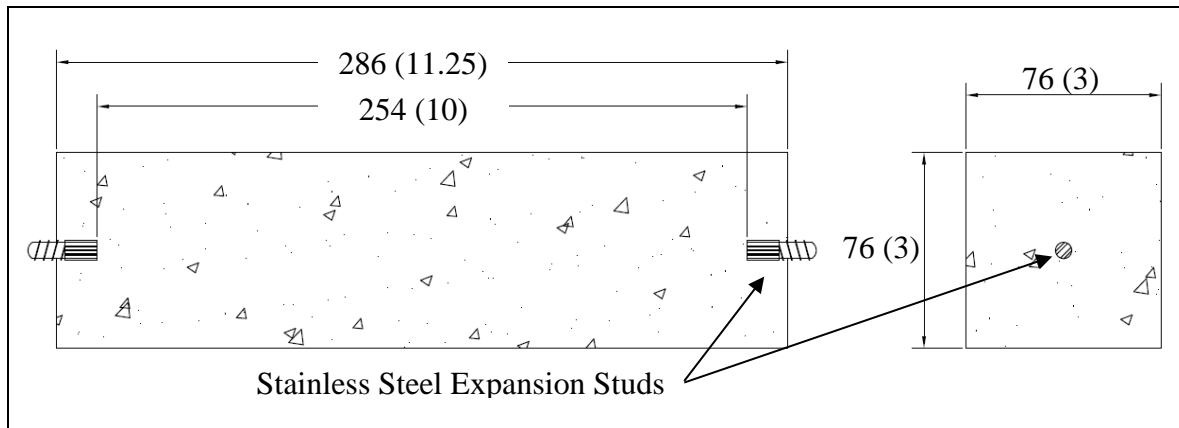


Figure 4-5 Concrete Prism Test Specimen Dimensions, mm (inches)

Samples were stored within a fog room for 24 hours after casting at 23 °C and 96 percent relative humidity. Demolding occurred at 24 hours and the length of each expansion sample was measured in relation to a comparator bar for a “zero” reading. Samples were subsequently transferred to 5 gallon buckets in which samples sit on a platform over 25 mm of water. Each bucket contains strips of felt lining the walls to pull moisture up from the base and normalize the internal storage conditions. Storage containers are sealed and placed in a constant 38 °C environmental chamber. The evening prior to the prescribed dates of measurement, samples are removed from their accelerating environment and returned to the room temperature fog room. By the morning of measurement, samples equilibrate at a consistent temperature to eliminate any

thermal expansion effects and provide a comparative length reading. Expansion is measured as the difference between readings and the zero reading divided by the initial length between expansion stubs.

The companion cylinders and flexural prisms cast to allow for periodic testing of compressive strength and stiffness as a measure of intermediate ASR damage undergo curing and storage conditions consistent with the expansion samples with the exception of not being removed from the 38 °C chamber for monthly expansion measurements. Cylinder testing coincides with the 1 month and final (1 or 2 year) expansion measurements, with an additional set of cylinders available for intermediate testing at the discretion of the tester. In total, 4 discrete scenarios of aggregate type/content and binder constituent/content are investigated (Table 4-9).

Table 4-9 CPT Test Parameter Grid¹

	Wright Sand	Spratt Gravel / Vulcan Sand
ASTM C1293 Mix Proportioning	X	X
HyFRC Mix Proportioning	X	-
SCC Mix Proportioning	X	-

¹Each checked box represents an ASR expansion experiment conducted comparing concrete with and without 1.5 volume percent hybrid fiber reinforcement

4.6 Results

4.6.1 AMBT Results

Performance of materials and mitigation mechanisms in the AMBT test is judged by expansion following 14 days of immersion in 80 °C 1N NaOH. As each of the aggregates under consideration contains deleterious constituents identified by petrographic analysis in addition to previously published performance results (Folliard et al. 2006, Rodgers and McDonald 2011) it is no surprise that all mortars tested exceed the failure threshold of 0.200 percent expansion. For each set of mortar bars belonging to a sample set outlined in the test parameter grid of Table 4-7, the average expansion values are plotted in Figure 4-6 through Figure 4-9 with mixes identified by aggregate initial and either a “-M” or “-F” to denote mortar or fiber reinforced mortar respectively.

In the case of using Wright sand as the reactive aggregate, the restraining influence of 1 percent PVA microfiber reinforcement is readily apparent in Figure 4-6. Regardless of the aggregate gradation (F.M. of 2.6 or 2.9) fiber reinforcement can be observed to decrease expansion by 20 to 30 percent. This level of expansion reduction is significant insofar as it decreases the overall expansion of the mortar containing the “as-received” aggregate from exceeding by a large margin the failure threshold to bringing it nearly within range of being “passable” by this test.

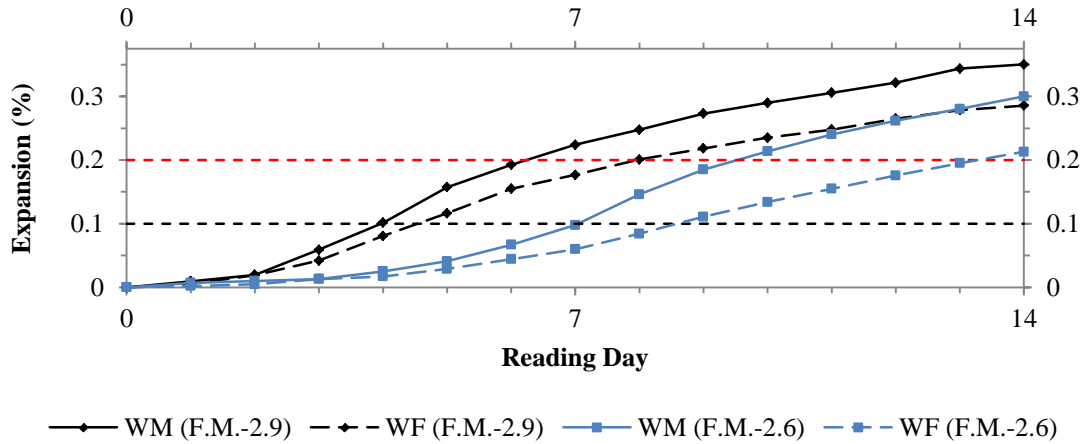


Figure 4-6 ASTM C1260 Expansion Plots of Wright Aggregate (gradations conforming to standard, F.M.-2.9 and as-received, F.M.-2.6)

In the case of using crushed Spratt sand as the reactive aggregate, it is apparent from Figure 4-7 that the addition of 1 percent PVA microfiber reinforcement had little effect. During testing it was theorized that this may have been a result of insufficient bond development between the fibers and cement matrix prior to expansion, due to the perceived earlier/faster expansion characteristics observed with Spratt aggregate versus Wright aggregate, so samples having a lengthened hot water curing period were prepared and tested. Mortar cube (50 mm side length) strengths, listed in Table 4-10, do show cement strengthening during this extended curing, with the stronger/denser matrix effect also being evident in the expansion potential of the mortar bars by reducing 14 day expansion by 30 percent (Figure 4-7).

Table 4-10 Spratt Aggregate Mortar Cube Strength Evolution, (MPa)

	Mortar	Fiber Reinforced Mortar
2 Days 80 °C H ₂ O	37.1	38.8
4 Day 80 °C H ₂ O	40.2	39.5
After 14 Days of ASR	44.5	44.1

The accompanying anticipated fiber bond strengthening did not produce the desired engagement of fiber reinforcement to restrain expansion. Despite ASR expansions greater than 0.200 percent being recorded for mortar bars cured for 4 days, the cube strengths after 14 days of ASR did not provide evidence of accumulated damage relative to the 4 day water cured stage despite the observation of surface cracks. Likely, this is a result of the continued hydration process (strengthening and densification) being greater than the damaging ASR gel swelling in addition to the geometrical differences between cubes and mortar bars which influenced the availability of alkali ions to aggregate particles located near the sample cores. By extending the AMBT testing beyond 14 days, the gel damage effect could be increased to the point that strength loss could be realized. However, to reach such an extreme level of aggregate distress and mortar expansion would have little bearing on encountered field conditions and as such it was not pursued for further investigation.

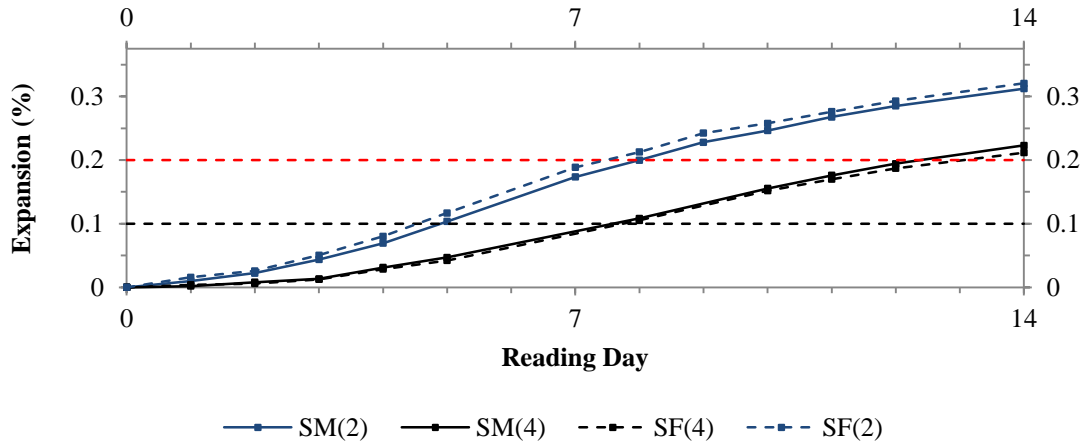


Figure 4-7 ASTM C1260 Expansion Plots of Spratt Aggregate (gradation conforming to standard), with 2 and 4 Day H₂O Curing Steps

In the case of using Vulcan sand as the reactive aggregate, it is apparent that the influence of 1 percent PVA microfiber reinforcement matches the response observed with Wright sand more than crushed Spratt sand. Comparing the 14 day expansion values, shown in Figure 4-8, the fiber reinforcement is responsible for reducing expansion by 17 percent.

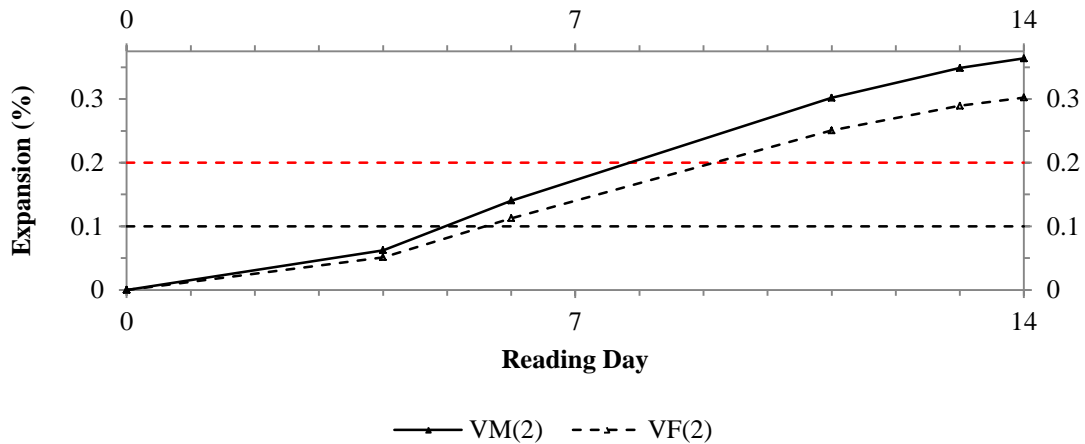


Figure 4-8 ASTM C1260 Expansion Plots of Vulcan Aggregate (gradation conforming to as-received)

Finally, in the case of using 50 percent replacement of portland cement by Class F fly ash, it is apparent from the expansion plots that the level of SCM mitigation is more than required to negate any meaningful expansion encountered with Wright sand (Figure 4-9). In such a mixture, the lack of any expansion prevents engagement and contribution by the fiber reinforcement to act as a mitigation mechanism.

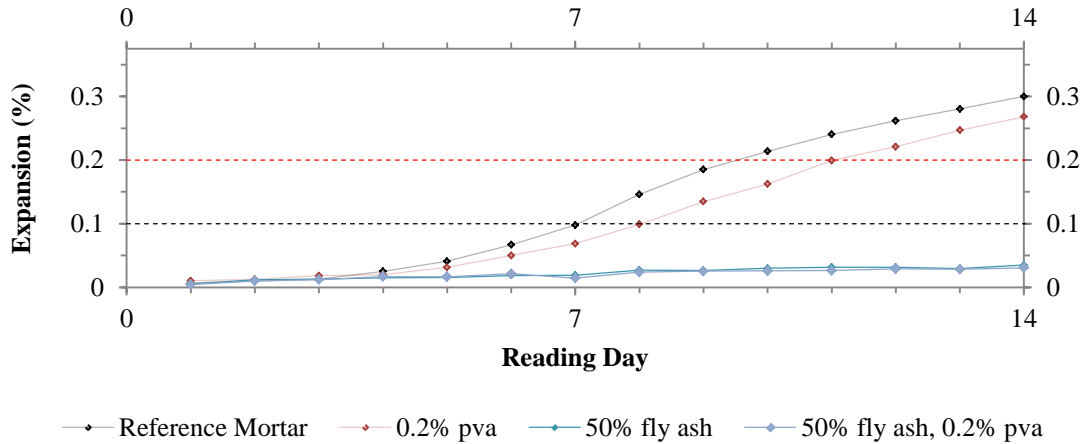


Figure 4-9 ASTM C1260 Expansion Plots of Wright Aggregate, High Volume Fly Ash

Combining the results of all expansion tests having a similar two day water curing step, the reference mortars can be ranked with respect to aggregate type as is done in Table 4-11. Through such a comparison, this issue of relative aggregate reactivity can be highlighted; despite having identical potentially reactive mass components, the overall expansions of Vulcan, 3.2 and Spratt, 2.9 differ by 15 percent, and Wright sand displaying the highest content of reactive materials in petrographic examination generates only a comparable level of expansion as the Spratt aggregate having half the reactive mass.

Table 4-11 Reactivity Ranking of Reference Mortars by Aggregate Type/Fineness Modulus

14 Day Expansion (%)	Aggregate Type, F.M.	Reactive Content ¹ (%)	Fiber Restraint (%)
0.364	Vulcan, 3.2	16	17
0.312	Spratt, 2.9	16	-
0.350	Wright, 2.9	31	19
0.300	Wright, 2.6	30	30

¹From petrographic analysis, Table 4-5

The performance of ASR damaged mortar bars under flexural loading for mixes fabricated with Wright fine aggregate, with and without high volume fly ash replacement and with microfiber reinforcement levels of 0, 0.2 and 1.0 volume percent are shown in Figure 4-10 through Figure 4-14. Of the pure portland cement mortar mixtures, it can be seen that unlike with compressive strength cubes, 14 days of accelerated ASR damage does degrade the mechanical properties of the samples. Maximal flexural strengths in all samples are recorded after the 2 day water curing regime and prior to any ASR activity. A stiffness reduction is likewise noted to occur in agreement with ASR expansion, which is consistent with internal cracks lessening the amount of material within the constant moment region of the beam which can behave in an elastic manner.

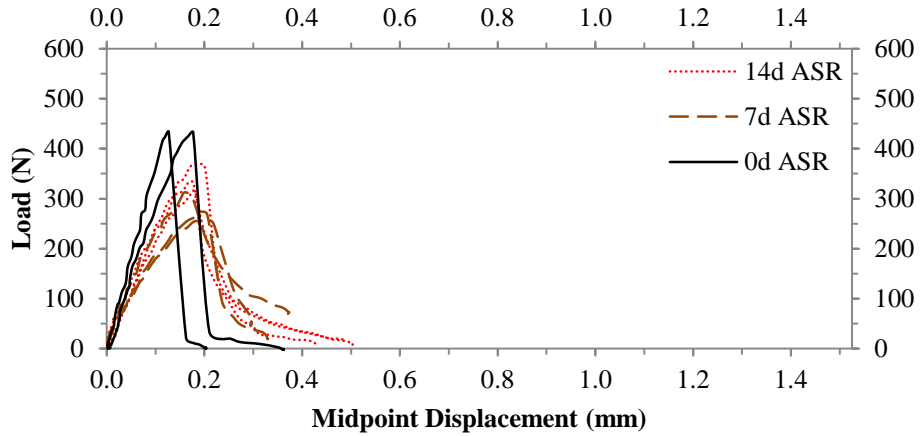


Figure 4-10 Flexural Response of Wright Aggregate ASR Mortar Bars

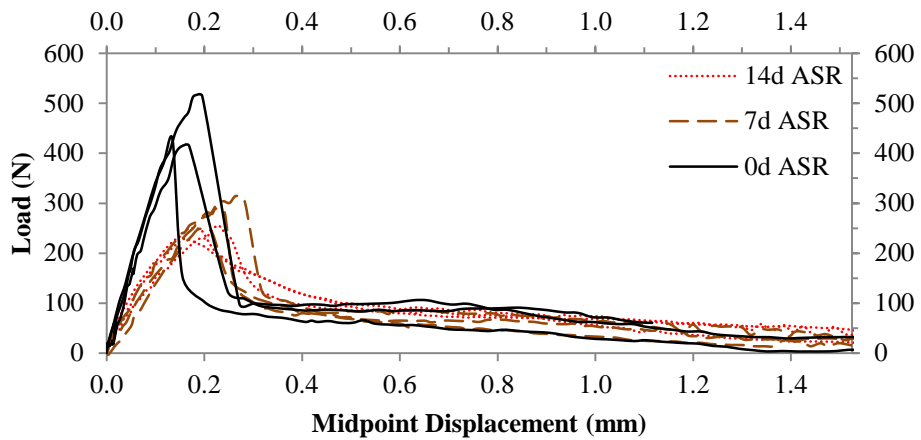


Figure 4-11 Flexural Response of Wright Aggregate ASR Mortar Bars, 0.2 Percent PVA Microfiber Reinforcement

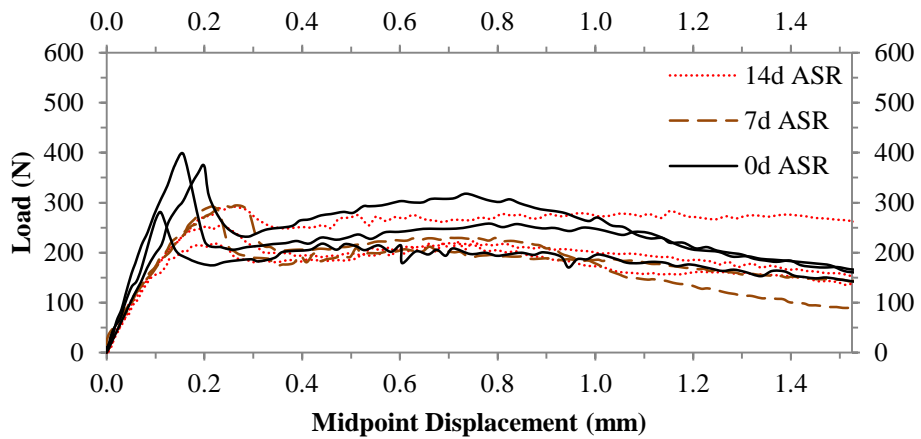


Figure 4-12 Flexural Response of Wright Aggregate ASR Mortar Bars, 1.0 Percent PVA Microfiber Reinforcement

Residual flexural strength afforded by fiber reinforcement was not impacted by ASR, implying that for the case of Wright sand there was little degradation in the pull-out resistance of the fibers. It seems likely in these samples that the activation of PVA microfibers to withstand ASR expansion/cracking initiated within the aggregate particles acts to limit the propagation of cracks through the cement matrix but has a less prominent role in changing the initiation of cracks. As the peak flexural strength of these non-deflection hardening composites is dictated by the response of a quasi-brittle mortar, the presence of such cracks is then responsible for the consistent drop in peak load observed for all three sample sets. Additionally, if the crack propagation restriction afforded by fiber reinforcement can be thought of as a preloading of the fiber to cement matrix bond, the remaining fiber capacity towards enhancing the elastic deformation performance prior to fiber slippage is reduced but the fiber still retains its frictional pull-out resistance which controls the large-displacement residual flexural strength parameter. Flexural response of high volume fly ash mortar mixtures were substantially similar at intermediate and completed stages of the sodium hydroxide soaking which is in agreement with the lack of damage inferred through the mortar bar expansion behavior.

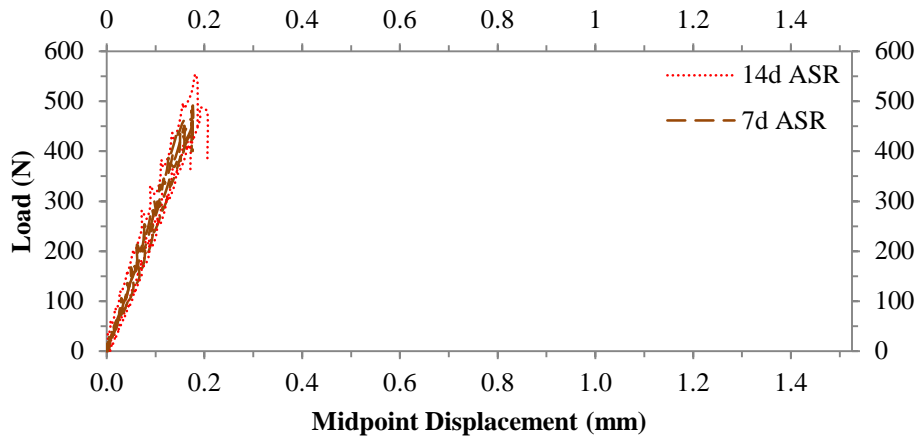


Figure 4-13 Flexural Response of Wright Aggregate, High Volume Fly Ash ASR Mortar Bars (from Hay 2014)

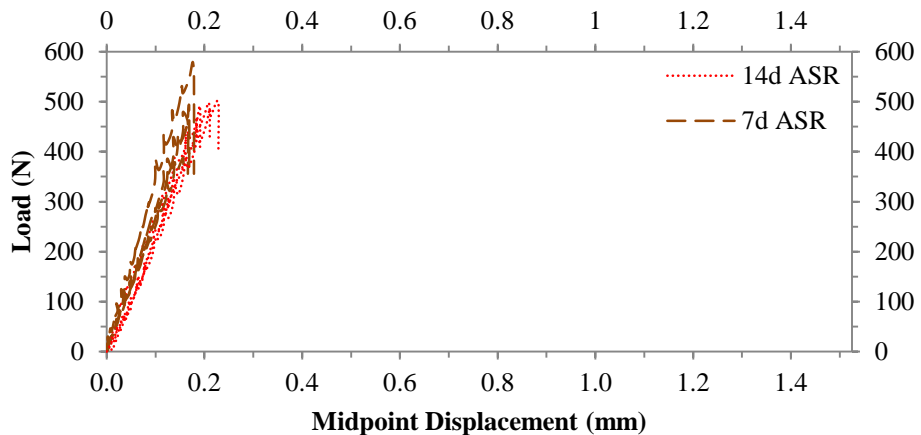


Figure 4-14 Flexural Response of Wright Aggregate, High Volume Fly Ash ASR Mortar Bars, 0.2 Percent PVA Microfiber Reinforcement (from Hay 2014)

The lack of continued strengthening encountered by both pure fly ash mortar and fiber reinforced fly ash mortar samples along with the brittleness experienced by the microfiber reinforced samples present difficulties in explaining. With respect to strengthening, it is possible that 80 °C sodium hydroxide soaking was sufficient to rapidly accelerate the pozzolanic process to fully complete within 7 days, such that no additional fly ash was available for continued reaction between 7 and 14 days but such a scenario seems unlikely. With respect to the brittleness of the 0.2 volume percent PVA microfiber reinforced samples, the lack of contribution to strength or any residual load capacity (relative to Figure 4-11) seems to imply that no bond was created between the fly ash-cement matrix and the fibers, though this would be contrary to the perceived action of the fly ash being fully reacted. An explanation for this contradictory action of fiber reinforced high volume fly ash mixes was experimentally uncovered by Wang and Li (2007) in which it was noted that at high fly ash contents, the polymer fiber surfaces were being coated by fly ash carbon constituents that lessened bond capacity development. The effect was noted to be strongly correlated with high volume SCM replacement, such that when later testing concrete mixes with a combined effect of 25 percent fly ash replacement and the inclusion of hooked end steel fibers the bond (both frictional and by mechanical anchorage) was not impacted by fly ash and was sufficient to develop the desired material toughening behavior.

4.6.2 CPT Results

Performance of materials and mitigation mechanisms tested by the CPT is judged by expansion following 1 to 2 years of storage at 38 °C, over water in sealed containers. Deviating from the standard measurement protocol of ASTM C1293, samples were typically measured for length change on a monthly basis. Failure of the CPT test is dictated by exhibiting an expansion exceeding 0.040 percent. This value is markedly lower than the threshold of the AMBT test due to the reduction in temperature but also the limitation in total alkalis available for participation in the reaction. The value of 0.040 percent expansion also correlates well with the expansion at which cracks are typically observed at the surface of the prism samples. This effectively ties performance criteria (retention of mechanical properties and concrete durability) to the perceived susceptibility of an aggregate and potential mitigating mechanism to ASR. For each set of concrete mixtures outlined in the test parameter grid of Table 4-9, the average expansion values are plotted in Figure 4-15 through Figure 4-20.

In the case of HyFRC testing with the reactive aggregate source being provided by Wright fine aggregate, the influence of fiber reinforcement can be observed. As depicted in Figure 4-15, the hybrid fiber reinforcement appears to be activated once expansion reaches a value of 0.010 percent, after which the expansion rate is slowed until being eliminated at 0.025 percent expansion. In contrast the conventional concrete reference is observed to continue expanding until reaching and slightly surpassing the failure threshold of 0.040 percent expansion.

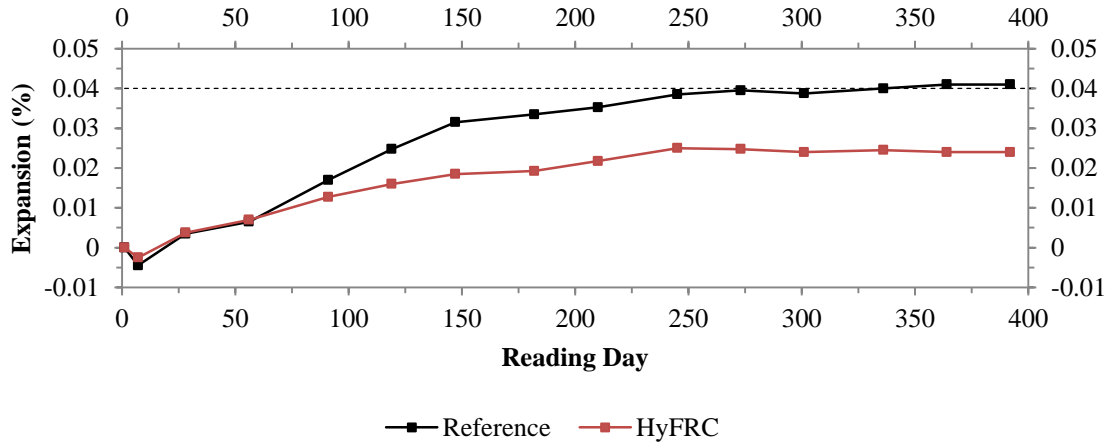


Figure 4-15 ASTM C1293 Expansion Plot of HyFRC Containing Wright Fine Aggregate

As anticipated, evidence of cracking was first observed on the surface of the control prisms at the measurements taken on day 245 at which point the average expansion of the reference concrete samples is 0.039 percent. The mechanical properties (compression strength, f_c , and elastic modulus, E) of the two mixes were measured at 28 days, 147 days and 364 days corresponding to no differentiation, achieving the “maximum” differentiation, and sustained differentiation states of relative expansion. The average of three cylinder test results is shown in Table 4-12, which clearly demonstrate a positive correlation between CPT expansion and concrete deterioration.

Table 4-12 Mechanical Properties of ASR Damaged HyFRC Containing Wright Fine Aggregate (Percent Change from 28 Day Result)

Sample Age	Expansion (%)	f_c (MPa)	E (GPa)
Reference Concrete			
28 Days	0.004	35.0	31.4
147 Days	0.032	38.4 (9.7)	29.3 (-6.5)
364 Days	0.041	39.0 (11.4)	22.9 (-26.9)
HyFRC			
28 Days	0.004	33.2	26.8
147 Days	0.019	35.6 (7.4)	27.5 (2.9)
364 Days	0.024	43.7 (31.6)	22.5 (-16.0)

It is interesting to note that despite the level of expansion achieved by the reference concrete in addition to the observation of surface cracks, the strength values over the course of ASR testing did not decrease. This is attributed to continued hydration and will be discussed further in relation to the other mixes tested. While the addition of fiber reinforcement and accompanying entrapped air is responsible for the lower initial (28 day) value of elastic modulus, the observed deterioration over time would appear to be a better indicator of incurred ASR damage as is reported in the literature.

Having displayed the potential of hybrid fiber reinforcement in the mixture proportions of HyFRC, the use of the same hybrid suite of fibers was evaluated in mixture proportions consistent with ASTM C1293. It can be seen from Figure 4-16 that the expected level of

expansion was not achieved. Even when lengthening the storage time to 500 days the expansion prisms of this project were not able produce a result in agreement with the 0.210 percent expansion reported by Folliard et al. (2006) which utilized the same aggregate and mixture proportions. The concrete surfaces of the expansion prisms remain defect free as would be expected by the low magnitude of expansion.

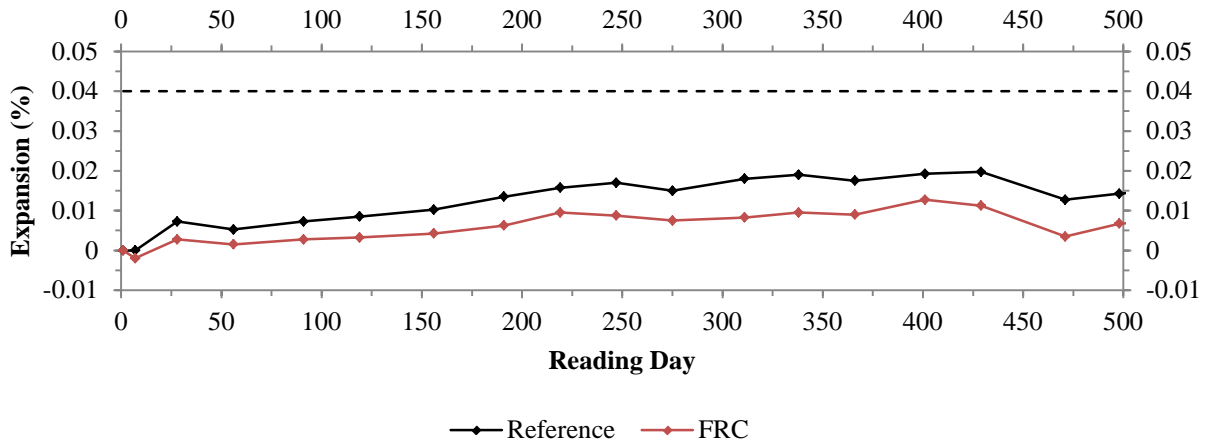


Figure 4-16 ASTM C1293 Expansion Plot of FRC Containing Wright Fine Aggregate

Unexpectedly, the cylinder samples and prisms not utilized for expansion measurements fabricated from the same batch of concrete discussed above and stored under the same conditions did display signs of distress. This discrepancy is displayed in Figure 4-17.

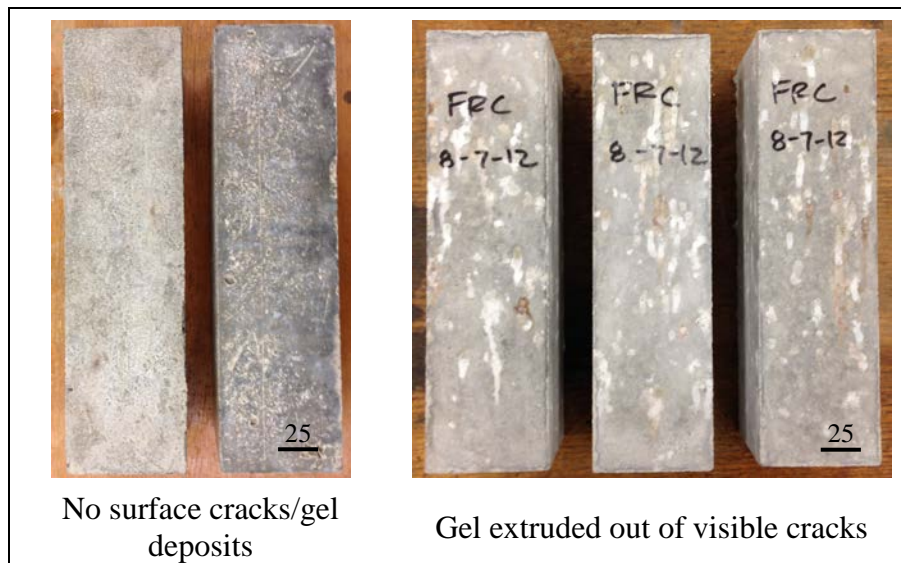


Figure 4-17 ASR Distress Inconsistencies Between Expansion Prisms (left) and Flexural Test Prisms (right) Having Wright Fine Aggregate, mm

Unfortunately, there were no initial length measurements taken of the flexural test prisms to which the damaged state could be compared so an exact measure of “true” expansion cannot be

known. In Table 4-13 describing the mechanical property degradation occurring over a period of 500 days, the values of expansion given are representative of Figure 4-16.

Table 4-13 Mechanical Properties of ASR Damaged FRC Containing Wright Fine Aggregate
(Percent Change from 28 Day Result)

Sample Age	Expansion (%)	f'_c (MPa)	E (GPa)
Reference Concrete			
28 Days	0.007	38.6	31.1
500 Days	0.017	51.3 (32.7)	20.5 (-34.1)
Fiber Reinforced Concrete			
28 Days	0.003	40.7	28.5
500 Days	0.009	61.2 (52.8)	22.7 (-20.3)

The values of stiffness reduction are consistent with those established in the HyFRC mixture, which compliments the theory that the “true” expansion was greater than recorded. Nevertheless, flexural testing of the fiber reinforced concrete mix (shown in Figure 4-18) performed at 28 and 500 days of storage implies that the damage producing elastic modulus changes is not impactful on fiber toughening of concrete. It is worth noting however that though the compressive strength increased by 50 percent over the same period of time, a similar increase in cracking load was not observed. This is attributed localized weakening due to ASR damage based on the observation that flexural cracks developed through locations of distress (as evidenced by carbonated gel deposition) on the tensile face.

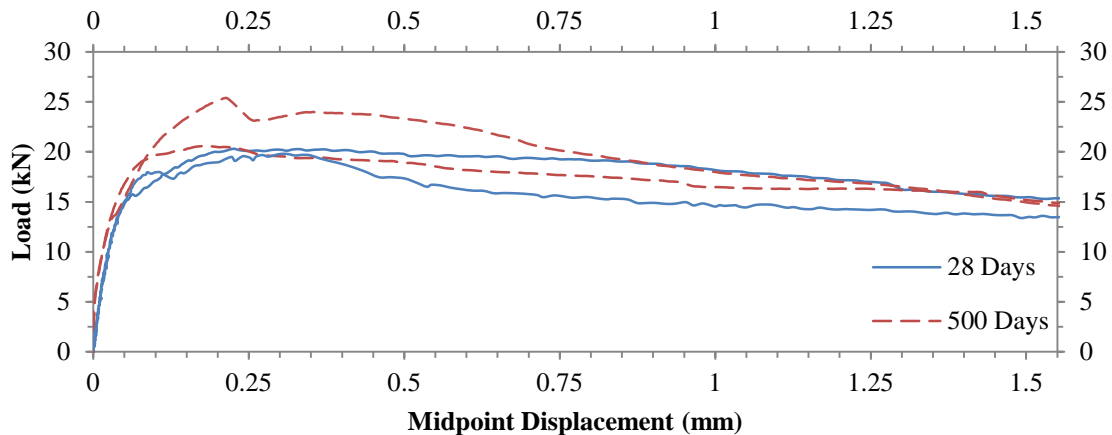


Figure 4-18 Load Deflection Response of ASR Damage FRC Containing Wright Fine Aggregate

The final variation of the examination of fiber reinforcement restraint of ASR damage caused by the inclusion of Wright fine aggregate utilized the SC-HyFRC mixture. As the SC-HyFRC mix contains a 25 percent replacement of portland cement by Class F fly ash, two reference mixtures we prepared to decouple the mitigation afforded by fly ash and the mitigation afforded by hybrid fiber reinforcement. As previously mentioned, this produced one reference mixture, “SCC (0% Fly Ash)”, which contained a portland cement content well outside the range typically tested with ASTM C1293. It was unknown how this difference coupled with the high content of fine aggregate would participate in relation to the “pessimism” effect. Following 2 years of

conditioning at 38 °C, due to the inclusion of fly ash, it is apparent that Class F fly ash at a replacement level of 25 percent is sufficient to mitigate the high level of ASR expansion that otherwise occurs (comparing “SCC (0% Fly Ash)” and “SCC (25% Fly Ash)” in Figure 4-19). The hybrid fiber reinforcement included in “SC-HyFRC (25% Fly Ash)” does not appear to participate in controlling the expansion due to lack of induced cracking.

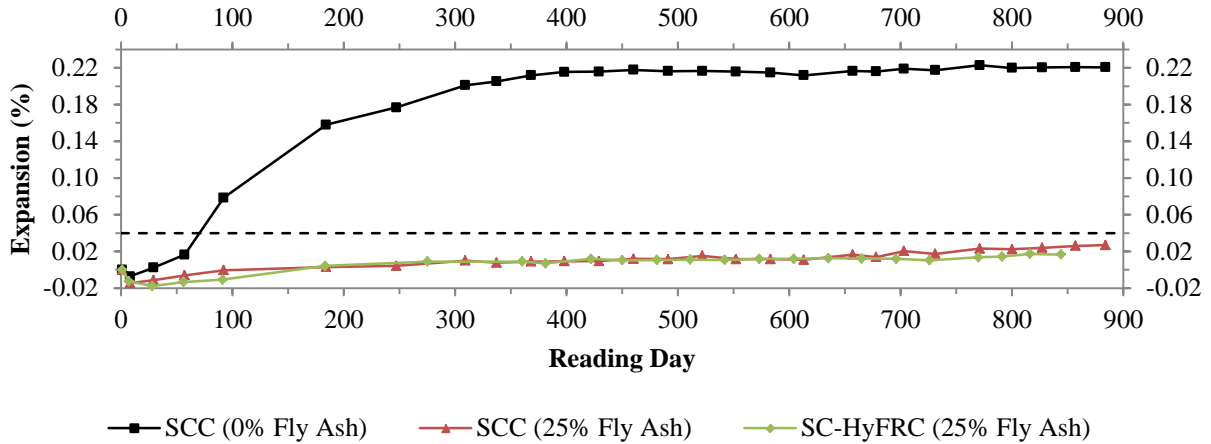


Figure 4-19 ASTM C1293 Expansion Plot of SC-HyFRC Containing Wright Fine Aggregate

With the SCC (0% Fly Ash) experiencing the highest level of expansion, 0.216 percent at one year, it is not surprising that it likewise suffers the greatest loss of mechanical properties (Table 4-14) yet recorded as part of this investigation. As an aside, it is interesting to note that the one year expansion closely matches the value reported by Folliard et al. (2006) of 0.210 which would seem to imply there is little pessimum effect displayed despite having a 30 percent increase in cement and a 79 percent increase in fine aggregate. The potential benefit gained by including hybrid fiber reinforcement is illuminated when comparing degradation of mechanical properties that occurs over the course of the ASR process. Despite displaying equivalent values of expansion, the growth and retention of strength and elastic modulus is improved by the presence of fibers.

Table 4-14 Mechanical Properties of ASR Damaged SC-HyFRC Containing Wright Fine Aggregate (Percent Change from 28 Day Result)

Sample Age	Expansion (%)	f_c (MPa)	E (GPa)
SCC (0% Fly Ash)			
28 Days	0.002	46.4	27.8
365 Days	0.216	35.0 (-24.7)	15.5 (-44.3)
730 Days	0.221	N/A	N/A
SCC (25% Fly Ash)			
28 Days	-0.011	49.8	31.6
365 Days	0.012	53.4 (7.3)	30.1 (-4.7)
730 Days	0.027	N/A	N/A
SC-HyFRC (25% Fly Ash)			
28 Days	-0.018	43.9	30.4
365 Days	0.011	54.3 (23.7)	32.0 (5.6)

730 Days	0.017	49.5 (12.8)	29.3 (-3.6)
----------	-------	-------------	-------------

The final scenario of CPT tests included within this investigation focuses on the application of the hybrid fiber reinforced constraint to concrete mixtures in which the coarse aggregates are the reactive component. This was accomplished by fabricating samples of fiber reinforced concrete having the mixture proportions defined by ASTM C1293 utilizing Spratt coarse aggregate. Such a mixture was found by Folliard et al. (2006) to exhibit an expansion of 0.204 percent at one year which makes it a suitable candidate from which to gauge the restraint of fiber reinforcement. Preliminary results are displayed in Figure 4-20 with the expansions having passed the critical threshold value within the initial 3 months of testing. This coincided with observation of surface cracks on all samples, with the map cracking more established on the Reference concrete prisms than on the FRC prisms. Though the expansion of the FRC mixture has displayed cracking and surpasses the failure criteria it is still worth noting that a significant reduction in expansion is achieved in addition to a lower expansion rate being expressed at the most recent measurement.

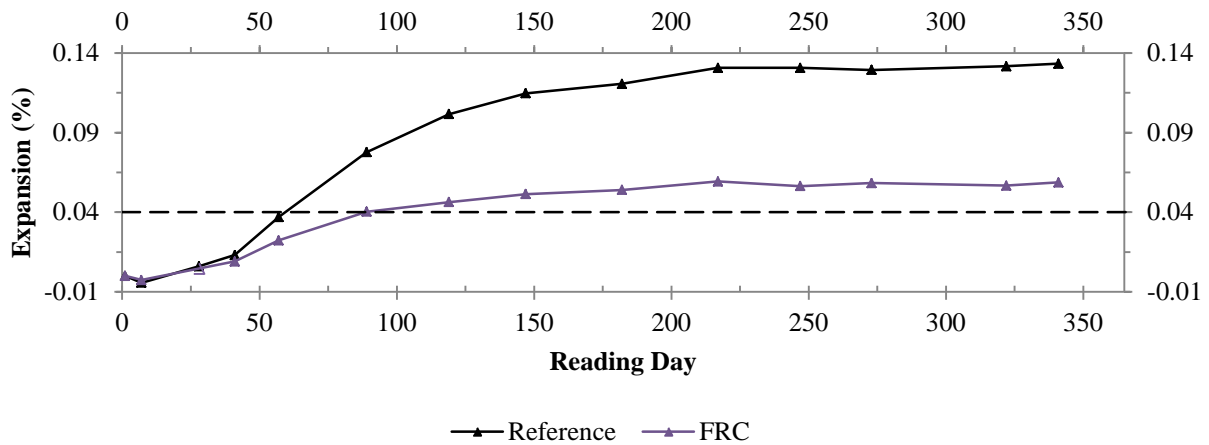


Figure 4-20 ASTM C1293 Expansion Plot of FRC Containing Spratt Coarse Aggregate

An intermediate measure of mechanical property degradation was carried out for both the Reference and FRC mixtures containing Spratt coarse aggregate with the results tabulated in Table 4-15. It is counterintuitive that concrete displaying the cracking and expansion of the reference could experience an increase in strength between 28 and 182 days based on the reduction seen in the SCC (0% Fly Ash) mixture of the previous sample set but it is difficult to come to a conclusion based on the sparse data set.

Table 4-15 Mechanical Properties of ASR Damaged FRC Containing Spratt Coarse Aggregate (Percent Change from 28 Day Result)

Sample Age	Expansion (%)	f_c (MPa)	E (GPa)
Reference Concrete			
28 Days	0.006	45.9	30.6
182 Days	0.121	52.7 (14.9)	21.0 (-31.4)
Fiber Reinforced Concrete			
28 Days	0.005	51.1	29.5

182 Days	0.054	61.2 (19.6)	23.8 (-19.4)
----------	-------	-------------	--------------

The relative gage of elastic modulus being a better indicator of damage appears to hold true for the mixture involving reactive coarse aggregate.

4.7 Discussion

4.7.1 AMBT Discussion

Microfiber reinforcement in the form of PVA fibers has been shown to be effective in delaying the onset of high reactivity rates in the presence of Wright and Vulcan fine aggregates. Restraint is achieved by minimizing the internal microcracking and limiting the availability of reactants to reaction sites, regardless of low or high volume dosages. Higher dosages appear increasingly effective at limiting the maximum reactivity of ASR. This can be attributed to the reduction in cracking which may be 1) preventing optimization of reaction kinetics by limiting egress of gel from the sand particles or 2) limiting exposure of new silica grains which would otherwise be integrated in the internal crack pattern. Analysis of the internal structure of mortars containing Wright and Vulcan fine aggregate by microscopy offered clear identification of the deleterious nature of ASR (Figure 4-21).

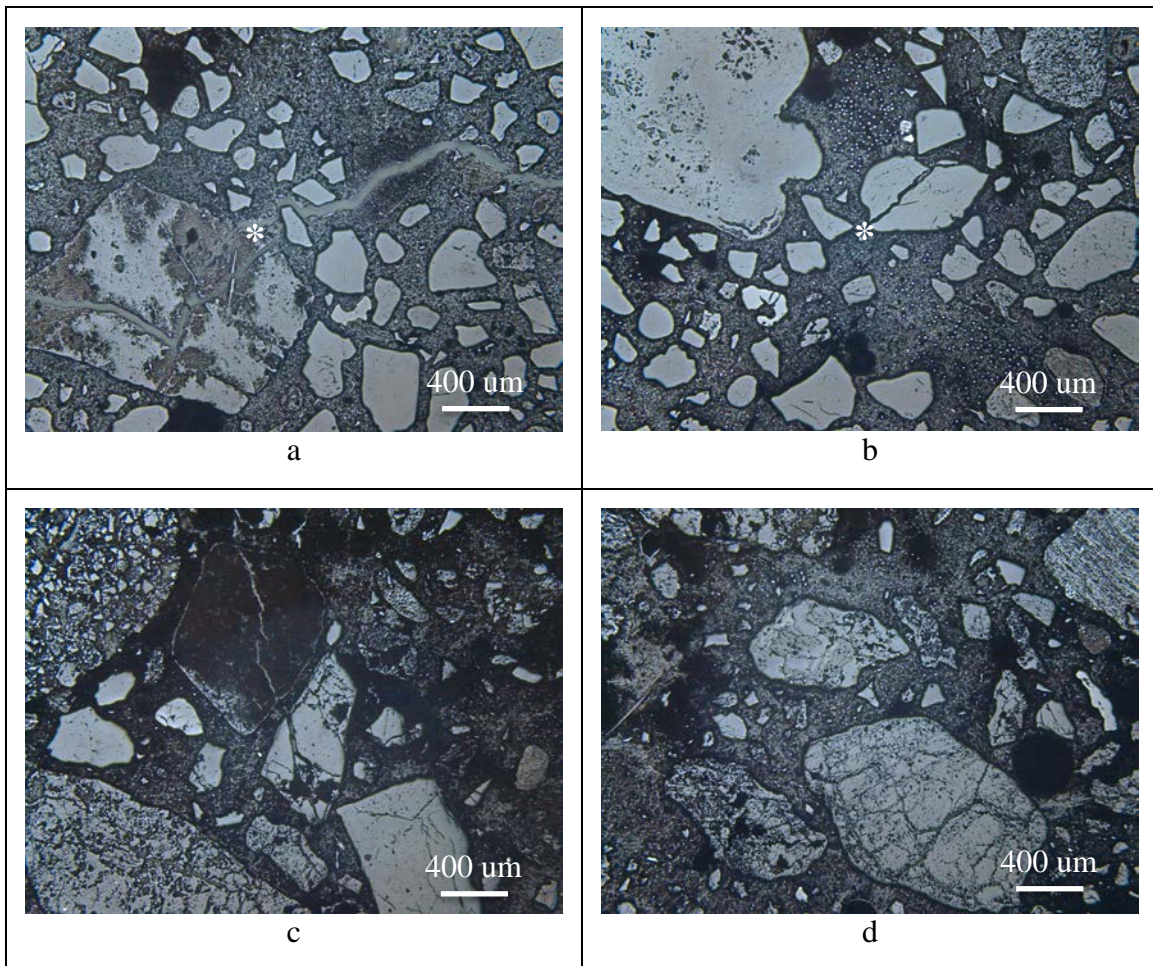


Figure 4-21 Internal Microstructure of; a) Wright Mortar, b) Wright Microfiber Reinforced Mortar, c) Vulcan Mortar, d) Vulcan Microfiber Reinforced Mortar. Spots for Later EDX Analysis Highlighted

Uniformly it is noted that in the cases of microfiber reinforcement, propagation of ASR cracks formed within aggregate particles and extending into the cement matrix was more limited. Additionally, crack severity in the Wright mortar specimens was anecdotally observed to be greater than their microfiber reinforced counterparts. Such observations are consistent with the additional cracking resistance expected by the inclusion of fiber reinforcement. Remnants of ASR remaining in the cracks (at spots indicated on Figure 4-21a and Figure 4-21b) were determined by Energy Dispersive X-Ray Spectrometry (EDX) to have sodium, silica, calcium ratios described in Table 4-16. The reduced level of sodium found within cracks in microfiber reinforced samples is believed to be consistent with a less mobile gel product. The higher relative calcium content within microfiber reinforced mortar is inferred to be due to alkali recycling as the gel interacts with the cement paste. Being both less mobile and possibly less in volume, the gel produced can undergo alkali recycling with the surrounding available calcium to a greater extent before it is extruded further from the reaction site. While a greater degree of alkali recycling may be an issue of concern by implying a greater availability of alkali ions to promote further ASR deterioration, this potentially “delayed expansion” was not experimentally witnessed with the late-stage expansion of fiber reinforced samples showing no quantitative increase over their reference counterparts. Similarly in all CPT tests, the late-stage expansion was largely observed to plateau and imply a stable and conclusive restriction of the expansion process.

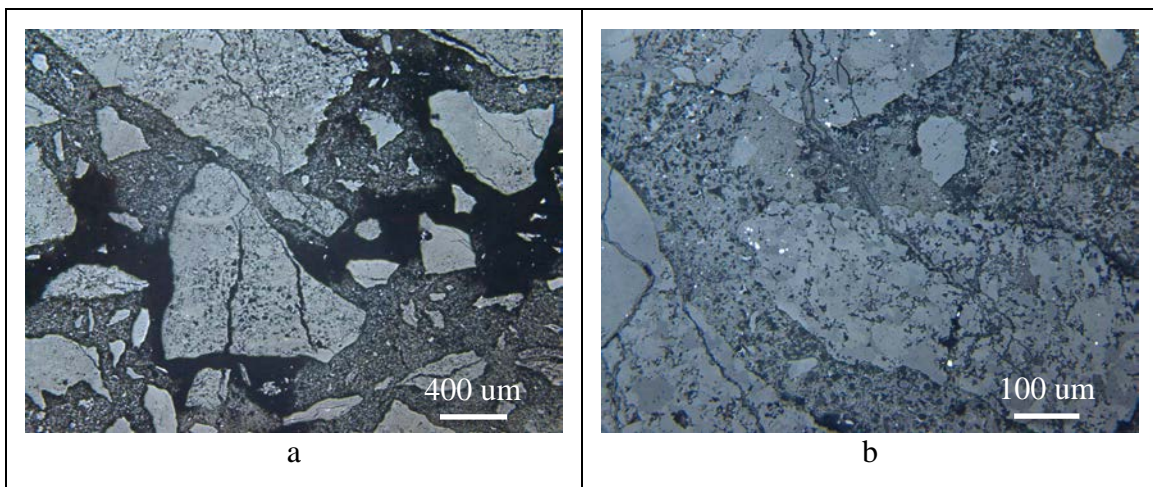
Table 4-16 Sodium, Silica, Calcium Molar Ratio from EDX Spot Analysis of Crack Deposits

Spot Analysis	Wright Mortar	Wright Microfiber Reinforced Mortar
Within Aggregate	2.6 : 57.2 : 1.0	0.1 : 12.2 : 1.0
At Interface	0.2 : 1.6 : 1.0	0.2 : 1.7 : 1.0
Within Paste	0.4 : 2.1 : 1.0	0.1 : 0.5 : 1.0

Flexural responses of mortar bar samples having been removed from the testing process at three distinct schedules indicate that higher levels of fiber reinforcement may be required to generate quantitative improvements to residual flexural strength and stiffness following exposure to ASR. Additionally, such testing reveals that even when using a conservative value (0.10 percent) to limit allowable expansion the microstructural damage contained within the mortar matrix at and prior to such a limit is enough to cause substantial losses in mechanical properties. In mortar mixtures which control ASR expansion through conventional methods, such as fly ash substitution, the presence of microfiber reinforcement neither improves nor decreases response to the accelerated testing regime. However, when comparing the relative decreases in strength and stiffness at intermediate and complete levels of ASR testing absent the inclusion of fly ash, universal trends cannot be established. Within the Wright Reference Mortar, 1 week of testing (0.10 percent expansion) produced flexural strength and flexural stiffness decreases of 34 and 44 percent respectively, yet after 2 weeks of testing (0.30 percent expansion) the flexural strength and stiffness loss reverted to be only 20 and 31 percent respectively. Somehow, whether by means of continued hydration of cement, crack healing or crack filling, the additional

microcracking associated with the continued expansion was overcome. In contrast, when examining the load-displacement response of fiber reinforced bars there is no “recovery” evident between the one and two week testing points. In the 0.2 percent PVA mixture, 1 week reductions are reported as 37 and 55 percent for strength and stiffness, while 2 week reductions are reported as 46 and 53 for strength and stiffness relative to their unreacted companions. In the 1.0 percent PVA mixture, 1 week reductions are reported as 20 and 42 percent for strength and stiffness, while 2 week reductions are reported as 27 and 37 for strength and stiffness relative to their unreacted companions. Interestingly, the reduction in performance criteria of strength and stiffness at 1 week for both mixes occurs prior to the samples exceeding the conservative expansion threshold of 0.10 percent, signifying that the magnitude of internal microcracking and strain would be of an “acceptable” level. Consistency between sample sets proved difficult to achieve, with the average strength and stiffness of mixes incorporating 1.0 percent PVA fibers following the water curing 20 and 28 less respectively than the mixes having either 0 or 0.2 percent PVA fiber which were largely similar. This discrepancy is accounted for in the casting of samples, particularly with respect to the consolidation of mortar mixes containing high dosages of polymer fibers without the aid of workability enhancers such as superplasticizer. Though not conducted, it is expected that an air content analysis of the 1.0 PVA mix would reveal considerably higher entrapped air which can be liable for the decreased strength and stiffness. Consequently, the role of entrapped air with regard to increasing sample porosity is likely coupled with the action of fiber reinforcement in producing the observed expansion behavior. While 1.0 percent of PVA fiber reinforcement was insufficient to provide for stable crack propagation, shown by sudden and substantial drops in the response curve at the first peaks, it is interesting to note the effectiveness of the fiber reinforcement in carrying residual loads. Despite carrying the stress induced through restricting expansion by 30 percent, residual fiber capacity allows samples to carry load equivalent to their non ASR damaged companions at large displacements (greater than 1.5 mm).

The Spratt fine aggregate proved unrestrainable by PVA microfiber reinforcement under the conditions of ASTM C1260. This was confirmed to be unrelated to mortar strength or fiber bond development by increasing the curing time. Under magnification (Figure 4-22), the PVA microfiber reinforcement can be observed to be in close proximity to the formed ASR cracks which eliminates fiber dispersion as a source of inconsistency.



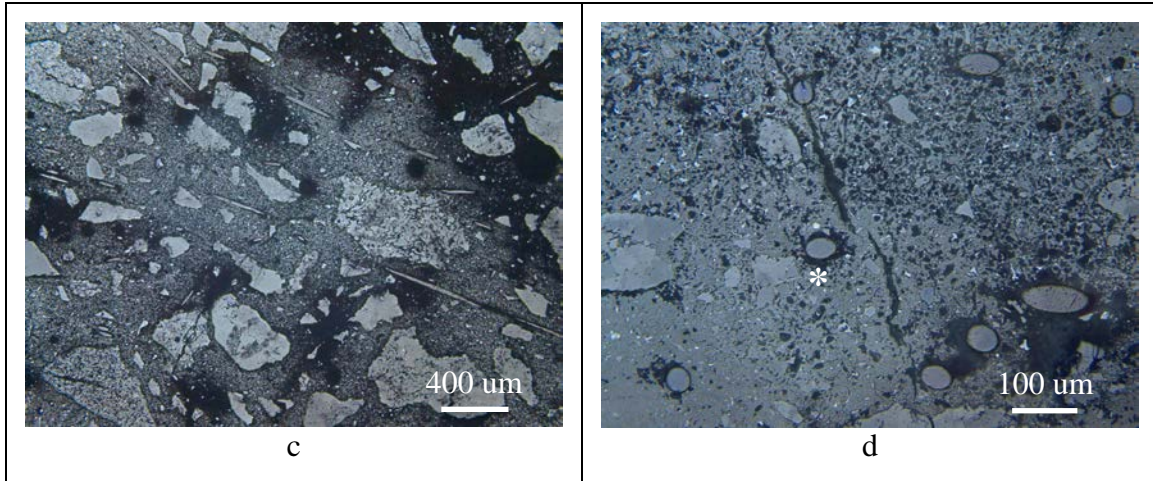


Figure 4-22 Internal Microstructure of Spratt Mortar (a,b) and Spratt Microfiber Reinforced Mortar (c,d), At 25X Magnification (a,c) and 100X Magnification (b,d)

At higher magnification a distinct feature of darkening of the cement paste surrounding the surface of the fibers was noted which had not been observed in either the Wright or Vulcan mixtures. EDX spot analysis (Table 4-17) of this feature identified it to have a composition rich in calcium and poor in silica and sodium. By comparison, the fibers in Wright mortar have an interfacial product rich in calcium and silica (presumably including calcium silicate hydrate and calcium hydroxide, principal hydration products of portland cement).

Table 4-17 Calcium, Silica, Sodium Content from EDX Spot Analysis of Fiber Interfacial Product

Mass, %	In Spratt Microfiber Reinforced Mortar	In Wright Microfiber Reinforced Mortar
Ca-Oxide	66.8	39.8
Si-Oxide	1.6	14.0
Na-Oxide	0.0	1.3

Fiber restraint performance is attributed to this sheathing of a calcium rich product with the assumption that bond development, regardless of curing time, would be challenged without direct contact between the fiber and calcium silicate hydrate. It is theorized that this layer of presumably limestone powder having been loosely adhered to the aggregate particles was released during the mixing process and preferentially collected on the surface of the PVA fibers in a manner similar to the high volume fly ash bonding issue encountered previously.

4.7.2 CPT Discussion

Hybrid fiber reinforcement has been shown to provide restraint of ASR in concrete in which the reactive mineral is contained in either the fine or the coarse aggregate. As the only mitigation mechanism present, it is found to be particularly effective by reducing the expansion of a concrete mixture displaying low reactivity (Wright fine aggregate Ref/HyFRC) by 40 percent after one year in addition to reducing the expansion of a concrete mixture displaying high reactivity (Spratt coarse aggregate Ref/FRC) by 55 percent after six months. Such reductions are consistent with the reduction in cracking observed on the surface of the concrete prisms. For both

mixtures, the concrete mechanical properties of compression strength and elastic modulus are likewise observed to be better retained with the presence of fiber reinforcement.

Further addressing the different levels of expansion reduction occurring within the Wright Ref/HyFRC and Spratt Ref/FRC, it is worthwhile to break down the expansion time history into representative segments. Within both mixture, and largely all other mixtures, the initial expansion (≤ 0.01 percent) is largely controlled by expansion occurring within the aggregate particles themselves prior to cracks extending into the cement matrix. During such time both mixtures expand at the same rate as their reference counterpart because the fibers have not yet been engaged. From this level of expansion onward, cracking is initiated in the cement matrix and the fibers (presumably microfibers first) act to restrain the production/swelling of ASR gel. At some undetermined point between 0.01 and 0.04 percent expansion the steel macrofibers begin to participate with an increasing contribution beyond 0.04 percent expansion. One aspect not previously discussed is that in no case of aggregate type were steel fibers found to have undergone plastic deformation of their hooked ends or fracture. Seemingly this means that all of the steel fibers participating in restraining expansion were still anchored and providing closure stresses without reaching the yield stress of steel. This also implies that they still had additional capacity such that they would provide more closure stress under higher expansion force. Such may be the reason that the expansion reduction in non-fly ash mitigated mixtures was greatest for the most severely expanding reference mixtures. Conversely, it is also probable that the utilization of Spratt as a coarse aggregate particle in the CPT test provided more heterogeneous regions of higher expansion while Wright as a fine aggregate particle provided more homogenous expansivity. Such a scenario may allow for better stress distribution into a macrofiber from a localized source of expansion rather than providing a distribution of microcracks along the length of the fiber which might otherwise inhibit the transfer of force through interface bond until greater levels of overall expansion activate the mechanical hooked anchorage. Such a scenario would be similar in theory to a discussion of bond in composite tension behavior and whether localized deformation-induced strain hardening provided for greater overall resistance than bond-degraded steel acting in tension. From the tension stiffening results of Chapter 2 it is apparent that a greater tensile strength can be achieved when resisting the breakdown of interfacial bond at the expense of overall ductility suggesting that macrofibers might be expected to perform better under the heterogeneous local expansion case.

The Class F fly ash employed in the SCC type prism tests at a replacement level of 25 percent is seen to be extremely effective at combating the expansion behavior of a high cement/high reactive aggregate content mixture, suppressing map cracking formation that would be evident otherwise. The presence of hybrid fiber reinforcement (in SC-HyFRC) does not change the expansion properties of the concrete prisms within the first year however it is observed to provide better retention of mechanical properties, principally elastic modulus. This improvement is attributed to better control of microcracking presumably brought about by discrete formations of ASR gel having low expansivity. Subsequent expansion appears to indicate that the combined effect of fly ash mitigation and hybrid fiber reinforcement can provide a suitable expansion deterrent with the magnitude of expansion reduced by approximately one third at two years, albeit still below the level of expansion that would signify concrete mixture failure of the CPT test. Such results would indicate that at the very least the inclusion of fiber reinforcement can be an effective safety net and should fly ash later prove unsuccessful in multi decade studies the presence of fibers will be able to maintain concrete durability properties.

In one set of samples, Wright fine aggregate Ref/FRC, an observation of inconsistency between expansion prisms and flexural testing prisms after 500 days of storage was made. The flexural testing prisms displaying signs of ASR distress while the expansion prisms did not. This issue remains unresolved due to the identical material and geometric parameters they shared. The one area where a perceived difference may be able to account for their differing behavior is in storage conditioning. While the flexural prisms remained in place, over water, in sealed containers for the duration of time between demolding and final testing, the expansion prisms were removed for one day per month to perform length change measurements. This day of difference involved removing the samples from their containers and placing them in the 23 °C fog room. It is possible, though seems unlikely, that during this short period of storage that enough condensation formed on the samples to leach alkalis out of the concrete. Alkali leaching, being a criticism of the storage conditions of ASTM C1293 (Thomas 2011) does have a direct effect on the magnitude of expansion reached by the concrete prism tests as there is no source of alkalis to replace the quantity lost as is the case with sodium hydroxide solution immersion in ASTM C1260. Irrespective of causation, interpretation of the expansion of this mixture is made with the expectation that the true expansion is greater than was recorded. It must be stated that the normalization process of expansion prisms for one night prior to length measurements was standard for all of the mixes investigated, such that if alkali leaching was to blame for the Wright fine aggregate Ref/FRC mixture it likewise influenced the expansions recorded for Wright fine aggregate Ref/HyFRC, Wright fine aggregate Ref/SCC/SC-HyFRC and Spratt coarse aggregate Ref/FRC. However, the extent of alkali leaching is likely not uniform between different sample sets due to differences in concrete porosity, having different water to cement ratios, and the presence of cracking.

The Spratt coarse aggregate samples, having the shortest elapsed time of monitoring, display the greatest reduction of expansion attributed to hybrid fiber reinforcement of the entire project. That expansion reduction is achieved by hybrid fiber reinforcement at the concrete prism scale but not by microfiber reinforcement at the mortar bar scale. The use of hooked end steel fibers in CPT testing generates a mechanical anchorage across developed cracks and does not solely rely upon interface bonding which is strongly impacted by potential sheathing from microscopic constituents (fly ash and/or limestone powder). Similar to the other ASR damaged concrete studied, the mechanical properties were better retained in the presence of the hybrid fiber reinforcement.

From a practical sense, establishing a numerical relationship between compression strength development and elastic modulus development with respect to ASR expansion would be most useful for applications of structural health monitoring and evaluation. Indeed some researchers (Swamy and Al-Asali 1988, Jones and Clark 1998, Marzouk and Langdon 2003, Multon et al. 2005) have reported well defined relationships between expansion and reduced properties for singular mixture designs. Attempting to find such a relationship with the small but diverse data set acquired during this project (Figure 4-23) however yields only the conclusion that strong correlations do not exist for concrete mixtures of differing proportions and aggregate type. Making direct comparisons to the values of Multon et al. (2005) it is very interesting to note that their strength values never show a decrease regardless of exhibiting expansion states in excess of those encountered in this project which makes the most comparable sample (Wright – “SCC (0% Fly Ash)”) look like an outlier. The Multon data set does show a decrease in elastic modulus with increasing expansion but to a much lesser degree than experienced with the Wright and Spratt aggregates of this project. From this presentation of data the most striking result is that

there appears to be a limit to elastic modulus loss somewhere in the range of 20 percent that can be achieved with the inclusion of hybrid fiber reinforcement whereas without such reinforcement the losses are regularly in the 30 percent or higher range.

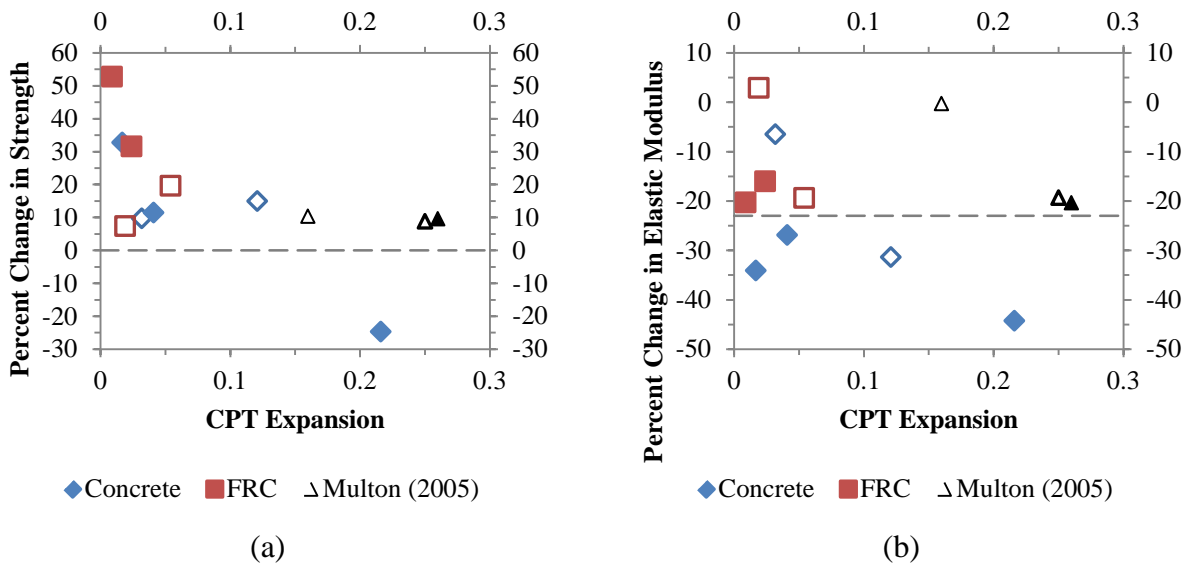


Figure 4-23 Comparison of a) Compression Strength and b) Elastic Modulus Development as a Function of ASR Expansion Level (with Multon et al. (2005) Results for Reference), Hollow Markers Representing 6 Month Data and Full Markers representing 1 Year Data

4.8 Conclusions

Hybrid fiber reinforcement within the context of fiber volumes utilized in this test program does appear to provide an effective restraint of alkali silica induced expansion damage under a variety of moderate and highly expansive mix proportions. While it is critical to note that some level of microcracking/damage must be accepted in order to engage the fiber reinforcement, the subsequent capacity of fiber to limit damage to a state in which macrocracking is suppressed and mechanical properties are largely retained provides significant benefits to both future concrete durability and ductility.

Specific to the different types of aggregates and materials utilized, it would appear the limestone powder created during the crushing process of limestone aggregates can collect preferentially around PVA fibers and greater limit their bonding capacity to the surrounding cement matrix in a manner similar to high volume fly ash. Under both conditions, in order to ensure adequate fiber to matrix bond development to provide crack resistant composite features, it is important to consider fiber geometries that are not solely dependent on interface friction to generate crack closure stresses. In the hybrid fiber reinforcement utilized in SC-HyFRC and HyFRC this entails the use of hooked end fibers in which a mechanical anchorage is developed and requires plasticity of the material to be mechanically pulled-out.

Relative to conventional pozzolanic admixture mitigation mechanisms, in both AMBT and CPT testing the incorporation of 50 percent and 25 percent of Class F fly ash is shown to be superior with respect to limiting expansion relative to the levels of fiber reinforcement under investigation. However, the same results appear to indicate that the mitigation provided by Class F fly ash is not suppressing all of the internal cracking which results in gradual loss of concrete mechanical properties. In contrast, fiber reinforcement is experimentally shown to provide a

better mitigation mechanism towards the goal of retaining mechanical properties. In totality, the utilization of both mitigation methods likely provides for the optimum response.

Finally, in addressing the applicability of the different test methods to providing a gauge of effectiveness of the fiber reinforcement mitigation method, based on geometrical considerations the larger, slower ASTM C1293 test would be considered superior. The reasoning behind this conclusion being primarily due to the ability to test both different aggregates and fibers with much less scaling irregularity involved. In the long term, the applicability of fiber reinforcement as a mitigation method should be evaluated on a decade scale test of an outdoor exposure element to completely eliminate all issues of scaling and variable leaching that have been encountered herein.

5 Concluding Remarks

Self-consolidating concrete features have been successfully adapted to HyFRC producing the high performance material Self-Consolidating Hybrid Fiber Reinforced Concrete. The resulting composite displays enhanced load carrying capacity in tension and flexure due to crack propagation resistance with ductility enhancement afforded in compression due to internal confinement effects. Simultaneously, the presence of fibers offers the concrete composite greater durability than conventional concrete when tested for reinforcement corrosion or alkali-silica reaction. The intrinsic crack resistance is capable of restricting the cracking that otherwise allows for a greater influx of potential reactants and a greater rate of damage accumulation. It is suggested that the material, having been tested under many different load conditions, is well suited for construction of bridge column elements in which compression, tension, flexure, environmental deterioration are all expected components of service exposure. Experimental testing of a scaled bridge column reveals a damage resistant element that; 1) delays spalling to higher strain levels than would be expected in conventional concrete, 2) contributes to carrying base shear despite having half of the conventional transverse reinforcement and 3) sustains a representative vertical load demand out to a drift ratio of 11 percent which is well in excess of anticipated demands.

While the combination of flexural loading/cracking as it relates to reinforcement corrosion initiation was experimentally investigated, many other relationships between the types of mechanically induced damage and environmentally induced damage under investigation can be extrapolated. For example, the spalling resistance of SC-HyFRC noted in the internal confinement testing preserves the cover concrete out to farther axial displacements than experienced by non-fiber reinforced concrete. In doing so, the cover concrete is still able to provide a barrier to the ingress of chloride ions and mitigate corrosion under intermediate loads. For reinforced concrete elements that develop corrosion induced splitting cracks like those experienced by the non-fiber reinforced beams subjected to corrosion, if subjected to tension in a manner similar to the direct tension test, the preexisting splitting crack will eliminate any initial stiffening effect the concrete may be able to provide prior to cracking due to the debonding of the steel reinforcement. In both cases, the damage associated with one mechanism (either mechanical or environmental) strongly inhibits the composite response to the other mechanism and conversely resisting damage by one mechanism assists in resisting the damage of the other mechanism.

An extreme case of this concept and how it has the potential to impact service life expectancy is addressed in relation to the bilinear model of Tuutti (1982). Having already presented the top graph in Figure 3-1, it is now more obvious that the initiation phase enhancement is a function of limiting mechanically induced changes in permeability while the propagation phase enhancement is a function of resisting the crack formation directly attributable to the environmental deterioration. However, we can also extend this bilinear model to more severe states of damage such as that brought about by an earthquake (Figure 5-1 bottom). While the damage incurred during seismic action may produce irreparable damage in a conventional column that would necessitate the end of effective service life, the improved performance of the SC-HyFRC material as exhibited in experimental testing may limit the damage to repairable levels. Even if internal damage exists that limits the original initiation enhancement, the propagation phase enhancement remains providing an even more drastic difference in extending the service life over a conventional counterpart.

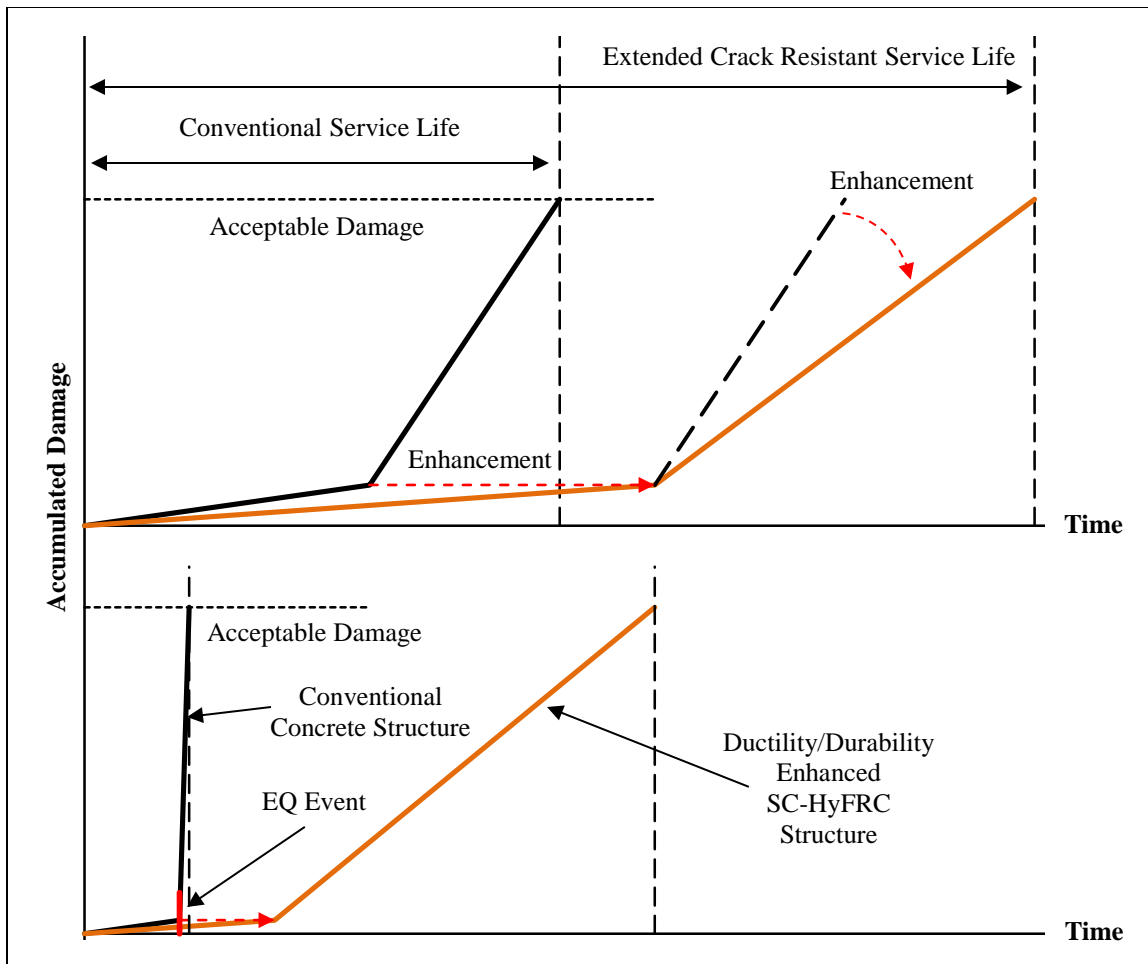


Figure 5-1 Projected Influence of Crack Resistance on the Service Life Expectancy as Related to Durability Mechanisms (top), Projected Influence of Earthquake Events Upon the Service Life Expectancy as Related to Durability Mechanisms (bottom)

In this sense, the mechanical performance benefits enhance the durability performance benefits of SC-HyFRC and vice versa. This synergistic relationship allows for significant advantages in meeting the load demands incurred over an entire service lifespan.

With respect to the application of the SC-HyFRC material to combatting other expansive type environmental deterioration mechanisms only limited information is available. In freeze-thaw studies, the hybrid matrix is seen to be effective at preventing matrix cracking under very low cycle counts (< 5) but fails to suspend cumulative cracking under additional cycle (~15). At large cycle counts (> 200), hybrid fiber reinforcement is reported effective at holding the constitutive materials together by resisting scaling and spalling but significant internal cracking is induced as measured by resonant dynamic modulus testing (Debatin 2008). Under similar cycling, polymer microfiber only reinforcement performs similar to the hybrid fiber mixtures while steel macrofiber only reinforcement is unable to resist the cracking or mass loss. Such results suggest that the scale of macrofibers is too large relative to the scale at which damage is developed and that perhaps smaller micro or even nanofiber reinforcement is necessary to better target the expansion of ice in concrete pores. While not addressed in this research, the concept of nanofiber reinforcement via carbon nanotubes or other materials would seem like a natural

evolution of fiber reinforcement targeting cracks as they develop at an even earlier stage. However as much as microfibers decrease the workability of current concrete mixes, it would be expected that the high surface area of nanofibers would require even more mixture changes to retain enough workability for placement and compaction.

Largely the issue of workability appears to remain a principal obstacle in the adoption of fiber reinforced concrete by the construction industry. Adaptations such as the one undertaken in this project to generate a self-consolidating mixture would appear to provide a bridge to using conventional construction technology to produce a superior product. Yet, while a great deal of literature exists describing the potential benefits of fiber reinforced concrete over conventional concrete breaking the inertia of the construction industry and its mentality to resist change has proven difficult. Test cases of fiber reinforced concrete by state Department of Transportations in California, Michigan and Oregon among others and at the Turner Fairbank Highway Research Center as an arm of the Federal Highway Administration provide an opportunity to get exposure to the construction field which will hopefully lead to citable stories of success that can be used to further the deployment of high performance fiber reinforced concrete into the nation's infrastructure.

References

- ACI Committee 222 (2001) Protection of Metals in Concrete Against Corrosion (ACI 222R-01). American Concrete Institute, Farmington Hills, MI, 41 pp.
- Ahmed, T., Burley, E., Rigden, S., Abu-Tair, A.I. (2003) The effect of alkali reactivity on the mechanical properties of concrete. *Construction and Building Materials*. 17(2):123-144.
- Akcay B., Tasdemir M.A. (2012) Mechanical behavior and fibre dispersion of hybrid steel fibre reinforced self-compacting concrete. *Construction and Building Materials* 28(1):287-293.
- Al-Sulaimani G.J., Kaleemullah M., Basunbul I. A., Rasheeduzzafar. (1990) Influence of corrosion and cracking on bond behavior and strength of reinforced concrete members. *ACI Structural Journal*, 87(2):220-231.
- Andic, O., Yardimci, M.Y., Ramyar, K. (2008) Performance of carbon, polyvinyl alcohol and steel based microfibers on alkali-silica reaction expansion. *Construction and Building Materials*. 22(7):1527-1531.
- Andrade C., Alonso M.C., Gonzalez J.A. (1990) An Initial Effort to Use the Corrosion Rate Measurements for Estimating Rebar Durability, Corrosion Rates of Steel in Concrete Eds; Berke N.S., Chaker V., Whiting D. American Society for Testing and Materials Special Technical Publication 1065:29-37.
- Andrade C. and Alonso C. (1996) Corrosion rate monitoring in the laboratory and on-site. *Construction and Building Materials* 10(5):315-328.
- ASTM Standard C33, 2013, "Standard Specification for Concrete Aggregates," ASTM International, West Conshohocken, PA, 2013.
- ASTM Standard C39, 2014, "Standard test method for compressive strength of cylindrical concrete specimens," ASTM International, West Conshohocken, PA, 2014.
- ASTM Standard C127, 2012, "Standard Test Method for Density, Relative Density (Specific Gravity) and Absorption of Coarse Aggregate," ASTM International, West Conshohocken, PA, 2012.
- ASTM Standard C128, 2012, "Standard Test Method for Density, Relative Density (Specific Gravity) and Absorption of Fine Aggregate," ASTM International, West Conshohocken, PA, 2012.
- ASTM Standard C136, 2006, "Standard Test Method for Sieve Analysis of Fine and Coarse Aggregate," ASTM International, West Conshohocken, PA, 2006.
- ASTM Standard C150, 2012, "Standard Specification for Portland Cement," ASTM International, West Conshohocken, PA, 2012.
- ASTM Standard C876, 2009, "Standard Test Method for Corrosion Potentials of Uncoated Reinforcing Steel in Concrete," ASTM International, West Conshohocken, PA, 2009.
- ASTM Standard C1152, 2004, "Standard Test Method for Acid-Soluble Chloride in Mortar and Concrete," ASTM International, West Conshohocken, PA, 2004.
- ASTM Standard C1260, 2007, "Standard Test Method for Potential Alkali Reactivity of Aggregates (Mortar-bar Method)," ASTM International, West Conshohocken, PA, 2007.
- ASTM Standard C1293, 2008, "Standard Test Method for Determination of Length Change of Concrete Due to Alkali-Silica Reaction," ASTM International, West Conshohocken, PA, 2008.
- ASTM Standard C1609, 2012, "Standard test method for flexural performance of fiber reinforced concrete (using beam with third-point loading)," ASTM International, West Conshohocken, PA, 2012.

- ASTM Standard C1611, 2014, "Standard test method for slump flow of self-consolidating concrete," ASTM International, West Conshohocken, PA, 2014.
- ASTM Standard C1621, 2009, "Standard test method for passing ability of self-consolidating concrete by J-ring," ASTM International, West Conshohocken, PA, 2009.
- ASTM Standard G59, 2009, "Standard Test Method for Conducting Potentiodynamic Polarization Resistance Measurements." ASTM International, West Conshohocken, PA, 2009.
- ASTM Standard G109, 2013, "Standard Test Method for Determining Effects of Chemical Admixtures on Corrosion of Embedded Steel Reinforcement in Concrete Exposed to Chloride Environments." ASTM International, West Conshohocken, PA, 2013.
- Austin S.A., Lyons R., Ing M.J. (2004) Electrochemical behavior of steel-reinforced concrete during accelerated corrosion testing. *Corrosion* 60(2):203-212.
- Balouch S.U., Forth J.P., Granju J.L. (2010) Surface corrosion of steel fibre reinforced concrete. *Cement and Concrete Research* 40(3):410-414.
- Banthia N., Gupta R. (2004) Hybrid fiber reinforced concrete (HyFRC): fiber synergy in high strength matrices. *Materials and Structures* 37(10):707-716.
- Blunt J. (2008) The effect of fiber reinforcement on the corrosion controlled degradation of reinforced concrete flexure elements (Doctoral dissertation). University of California, Berkeley. Berkeley, CA
- Blunt J., Ostertag C.P. (2009) Deflection hardening and workability of hybrid fiber composites. *ACI Materials Journal* 106(3):265-272.
- Bouzoubaa N., Lachemi M. (2001) Self-compacting concrete incorporating high volumes of class F fly ash, preliminary results. *Cement and Concrete Research* 31(3):413-420.
- Broomfield J.P. (2006) *Corrosion of Steel in Concrete: Understanding, Investigation and Repair* (2nd ed.). New York, NY: Taylor and Francis.
- Burgher, B., Thibonnier, A., Folliard, K.J., Ley, T., Thomas, M.D.A. (2008) Investigation of the internal stresses caused by delayed ettringite formation in concrete (Report No. FHWA/TX-09/0-5218-1). Austin, TX: Texas Department of Transportation.
- Cady P.D., Gannon E.J. (1993) Condition evaluation of concrete bridges relative to reinforcement corrosion, Strategic Highway Research Program S-330. National Academy of Sciences, Washington DC, 124 pp.
- Care S., Raharinaivo A. (2007) Influence of impressed current on the initiation of damage in reinforced mortar due to corrosion of embedded steel. *Cement and Concrete Research* 37(12):1598-1612.
- Debatin, J. (2008) Freeze-Thaw Testing of Fiber Reinforced Concrete (CEE 199 Report). University of California, Berkeley. Berkeley, CA
- Dent Glasser, L.S., Kataoka, N. (1981) The chemistry of alkali-aggregate reaction. *Cement and Concrete Research*. 11(1):1-9.
- Djerbi A., Bonnet S., Khelidj A., Baroghel-bouny V. (2008) Influence of transverse crack on chloride diffusion into concrete. *Cement and Concrete Research* 38(6):877-883.
- Drimalas, T., Folliard, K.J. (2014) Assessing Alkali-Silica Reactivity in the Field Based on Outdoor Exposure Tests. Presentation at the Corvallis Workshops: Innovative Characterization Tools to Assess Performance of Cement-Based Materials, Oregon State University, Corvallis OR, 15-18 July.
- Duchesne, J., Berube, M.A. (1994) The effectiveness of supplementary cementing materials in suppressing expansion due to ASR: Another look at the reaction mechanisms part 1: Concrete expansion and portlandite depletion. *Cement and Concrete Research*. 24(1):73-82.

- Dunstan, E.R. (1981) The effect of fly ash on concrete alkali-aggregate reaction. *Cement, Concrete and Aggregates*. 3(2):101-104.
- El Maaddawy T.A., Soudki K.A. (2003) Effectiveness of impressed current technique to simulate corrosion of steel reinforcement in concrete. *ASCE Journal of Materials in Civil Engineering* 15(1):41-47.
- Folliard, K.J., Barborak, B., Drimalas, T., Du, L., Garber, S., Ideker, J., Ley, T., Williams, S., Juenger, M., Fournier, B., Thomas, M.D.A. (2006) Preventing ASR/DEF in New Concrete: Final Report (Report No. FHWA/TX-06/0-4085-5). Austin, TX: Texas Department of Transportation.
- Francois R., Arliguie G. (1999) Effect of microcracking and cracking on the development of corrosion in reinforced concrete members. *Magazine of Concrete Research* 51(2):143-150.
- Ghods P., Isgor O.B., McRae G.A., Li J., Gu G.P. (2011) Microscopic investigation of mill scale and its proposed effect on the variability of chloride-induced depassivation of carbon steel rebar. *Corrosion Science* 53(3):946-954.
- Glasser, F.P. (1992) Chemistry of the Alkali-Aggregate Reaction. In R.N. Swamy (Ed.) *The Alkali-Silica Reaction in Concrete* (pp. 30-52). Bishopbriggs, Glasgow: Blackie and Son Limited.
- Gonzalez J.A., Andrade C., Alonso C., Feliu S. (1995) Comparison of rates of general corrosion and maximum pitting penetration of concrete embedded steel reinforcement. *Cement and Concrete Research*, 25(2):257-264.
- Goto Y. (1971) Cracks formed in concrete around deformed tension bars. *ACI Journal Proceedings* 68(4):244-251.
- Granju J.L., Balouch S.U. (2005) Corrosion of steel fibre reinforced concrete from the cracks. *Cement and Concrete Research* 35(3):572-577.
- Grubb J.A., Blunt J., Ostertag C.P., Devine T.M. (2007) Effect of steel microfibers on corrosion of steel reinforcing bars. *Cement and Concrete Research* 37(7):1115-1126.
- Grunewald S., Walraven J. (2001) Parameter-study on the influence of steel fibers and coarse aggregate content on the fresh properties of self-compacting concrete. *Cement and Concrete Research* 31(12):1793-1798.
- Haddad, R.H., Smadi, M.M. (2004) Role of fibers in controlling unrestrained expansion and arresting cracking in portland cement concrete undergoing alkali-silica reaction. *Cement and Concrete Research*. 34(1):103-108.
- Halmen C., Trejo D. (2012) Accelerating standard test method for assessing corrosion of steel in concrete. *ACI Materials Journal* 109(4):421-430.
- Hay R. (2014) Unpublished data.
- Hernandez-Cruz, D., Hargis, C.W., Bae, S., Itty, P.A., Meral, C., Dominowski, J., Radler, M.K., Kilcoyne, D.A., Monterio, P.J.M. (2014) Multiscale characterization of chemical-mechanical interactions between polymer fibers and cementitious matrix. *Cement and Concrete Composites*. 48:9-18.
- Jaffer S.J., Hansson C.M. (2008) The influence of cracks on chloride-induced corrosion of steel in ordinary portland cement and high performance concretes subjected to different loading conditions. *Corrosion Science* 50(12):3343-3365.
- Jones, A.E.K., Clark, L.A. (1996) The effects of restraint on ASR expansion of reinforced concrete. *Magazine of Concrete Research*. 48(174):1-13.
- Jones, A.E.K., Clark, L.A. (1998) The effects of ASR on the properties of concrete and the implications for assessment. *Engineering Structures*. 20(9):785-791.

- Ketchum M., Chang V., Shantz T. (2004) Influence of Design Ground Motion Level on Highway Bridge Costs. PEER Report 6D01. Pacific Earthquake Engineering Research Center, University of California, Berkeley, CA.
- Khayat K.H. (1999) Workability, testing, and performance of self-consolidating concrete. *ACI Materials Journal* 96(3):346-353.
- Kobayashi K., Iizuka T., Kurachi H., Rokugo K. (2010) Corrosion protection performance of High Performance Fiber Reinforced Cement Composites as a repair material. *Cement and Concrete Composites* 32(6):411-420.
- Koch G.H., Brongers M, Thompson N.G, Virmani Y.P., Payer J.H. (2001) Corrosion costs and preventive strategies in the United States, Report FHWA-RD-01-156. Office of Infrastructure Research and Development, McLean, VA, 773 pp.
- Kosa K., Naaman A.E. (1990) Corrosion of Steel Fiber Reinforced Concrete. *ACI Materials Journal* 87(1):27-37.
- Kurita M., Nomura T. (1998) Highly-flowable steel fiber-reinforced concrete containing fly ash. In V.M. Malhotra (Ed.) *ACI Special Publication* 178:159-175.
- Laio W.C., Chao S.H., Park S.Y., Naaman A. (2006) Self-consolidating high performance fiber reinforced concrete (SCHPFRC) - Preliminary Investigation. University of Michigan: Report No. UMCEE 06-02.
- Lawler J.S., Zampini D., Shah S.P. (2002) Permeability of cracked hybrid fiber-reinforced mortar under load. *ACI Materials Journal* 99(4):379-385.
- Lepech M., Li V. C. (2009) Water permeability of engineered cementitious composites. *Cement and Concrete Composites* 31(10):744-753.
- Lesnicki, K., Kim, J., Kurtis, K., Jacobs, L. (2013) Assessment of alkali-silica reaction damage through quantification of concrete nonlinearity. *Materials and Structures*. 46(3):497-509.
- Marzouk, H., Langdon, S. (2003) The effect of alkali-aggregate reactivity on the mechanical properties of high and normal strength concrete. *Cement and Concrete Composites*. 25(4):549-556.
- Mangat P.S., Gurusamy K. (1988) Corrosion Resistance of Steel Fibers in Concrete under Marine Conditions. *Cement and Concrete Research* 18(1):44-54.
- Malherio R., Meira G., Lima M., Perazzo N. (2011) Influence of mortar rendering on chloride penetration into concrete structures. *Cement and Concrete Composites* 33(2):233-239.
- Mehta P.K., Monteiro P.J.M. (2013) *Concrete: Microstructure, Properties, and Materials* (4th ed.). New York, NY: McGraw-Hill Professional.
- Miyazato S., and Hiraishi Y. (2005) Transport Properties and Steel Corrosion in Ductile Fiber Reinforced Cement Composites. *Proceedings of the Eleventh International Conference on Fracture*, Turin, Italy.
- Mobasher B., Li C.Y. (1996) Mechanical properties of hybrid cement-based composites. *ACI Materials Journal* 93(3):284-292.
- Mohammed, T.U., Hamada, H., Yamaji, T. (2003) Alkali-silica reaction-induced strains over concrete surface and steel bars in concrete. *ACI Materials Journal*. 100(2):133-142.
- Moreno D., Trono W., Jen G., Ostertag C.P., Billington S. (2014) Tension stiffening in reinforced high performance fiber reinforced cement-based composites. *Cement and Concrete Composites*, Vol. 50, pp.36-46.
- Multon, S., Seignol, J.F., Toutlemonde, F. (2005) Structural behavior of concrete beams affected by alkali-silica reaction. *ACI Materials Journal*. 102(2):67-76.

- Nagataki S., Fujiwara H. (1995) Self-compacting property of highly flowable concrete. In V.M. Malhotra (Ed.) ACI Special Publication 154:301-314.
- Nehdi M., Ladanchuk J.D. (2004) Fiber synergy in fiber-reinforced self-consolidating concrete. *ACI Materials Journal* 101(6):508-517.
- Nyugen W., Trono W., Ostertag C.P., Panagiotou M. (2014) Unpublished Manuscript.
- Okamura H., Ouchi M. (1999) Self-compacting concrete, development, present use and future. In A. Skarendahl, O. Petersson (Eds.) *Self-Compacting Concrete RILEM Symposium*. (pp. 3-14) Stockholm, Sweden.
- Ostertag, C.P., Yi, C.K., Monteiro, P.J.M. (2007) Effect of confinement on properties and characteristics of alkali-silica reaction gel. *ACI Materials Journal*. 104(3):276-282.
- Ozawa K., Maekawa K., Kunishima M., Okamura H. (1989) Performance of concrete based on the durability design of concrete structures. *Proceedings of the Second East Asia-Pacific Conference on Structural Engineering and Construction* (pp. 445-450) Chiang Mai, Thailand.
- Pleau, R., Berube, M.A., Pigeon, M., Fournier, B., and Raphael, S. (1989) Mechanical behavior of concrete affected by ASR. In K. Okada, S. Nishibayashi, M. Kawamura (Eds.) *Proceedings of the Eighth International Conference on Alkali-Aggregate Reaction in Concrete* (pp. 721-726). Kyoto, Japan.
- Poupard O., L'Hostis V., Catinaud S., Petre-Lazar I. (2006) Corrosion damage diagnosis of a reinforced concrete beam after 40 years natural exposure in marine environment. *Cement and Concrete Research* 36(3):504-520.
- Rapoport J., Aldea C.M., Shah S., Ankenman B., Karr A. (2002) Permeability of Cracked Steel Fiber-Reinforced Concrete. *Journal of Materials in Civil Engineering* 14(4):355-358.
- Reinhardt H.-W., Jooss M. (2003) Permeability and self-healing of cracked concrete as a function of temperature and crack width. *Cement and Concrete Research* 33(7):981-985.
- Rodgers, C., MacDonald, C.A. (2011) The geology, properties and field performance of alkali-aggregate reactive Spratt, Sudbury, and Pittsburg aggregate distributed by the Ontario Ministry of Transportation. Unpublished Manuscript.
- Rossi P. (1997) High performance multimodal fiber reinforced cement composites (HPMFRCC): The LCPC experience. *ACI Materials Journal* 94(6):473-483.
- Sahmaran M., Li V.C., Andrade C. (2008) Corrosion Resistance Performance of Steel-Reinforced Engineered Cementitious Composite Beams. *ACI Materials Journal* 105(3):243-250.
- Sahmaran M., Yaman I.O. (2008) Influence of transverse crack width on reinforcement corrosion initiation and propagation in mortar beams. *Canadian Journal of Civil Engineering* 35(3):236-245.
- Sahmaran M., Yurtseven A., Yaman I.O. (2005) Workability of hybrid fiber reinforced self-compacting concrete. *Building and Environment* 40(12):1672-1677.
- Samaha H.R., Hover K.C. (1992) Influence of microcracking on the mass transport properties of concrete. *ACI Materials Journal* 89(4):416-424.
- Schiessl P., Raupach M. (1997) Laboratory studies and calculation on the influence of crack width on chloride-induced corrosion of steel in concrete. *ACI Materials Journal* 94(1):56-61.
- Shehata, M.H., Thomas, M.D.A. (2000) The effect of fly ash composition on the expansion of concrete due to alkali-silica reaction. *Cement and Concrete Research*. 30(7):1063-1072.
- Stanton, T.E. (1940) Expansion of concrete through reaction between cement and aggregate. *American Society of Civil Engineers – Proceedings*. 66(10):1781 -1811.

- Stern M. and Geary A.L. (1957) Electrochemical Polarization. *Journal of the Electrochemical Society* 104(1):56-63.
- Swamy, R.N., Al-Asali, M.M. (1988) Engineering properties of concrete affected by alkali-silica reaction. *ACI Materials Journal*. 85(5):367-374.
- Swenson, E.G., Gillott, J.E. (1964) Alkali-carbonate rock reaction. *Highway Research Board* 45:21-40.
- Thomas M.D.A. (2011) The effect of supplementary cementing materials on alkali-silica reaction: A review. *Cement and Concrete Research*. 41(12):1224-1231.
- Thomas M.D.A., Fournier B., Folliard K.J. (2013) Alkali-Aggregate Reactivity (AAR) Facts Book. FHWA Report HIF-13-019. Office of Pavement Technology, Federal Highway Administration. Washington DC.
- Trono W., Jen G., Ostertag C.P., Panagiotou M. (2013) Seismic Response of a Rocking Post-tensioned HyFRC Bridge Column. Paper presented at the 10th International Conference on Urban Earthquake Engineering, Tokyo Institute of Technology, Tokyo, 1-3 March.
- Turanli L., Shomglin K., Ostertag C.P., Monteiro, P.J.M. (2001) Reduction in alkali-silica expansion due to steel microfibers. *Cement and Concrete Research*. 31(5):825-827.
- Tuutti K. (1982) Corrosion of steel in concrete (Doctoral Thesis). Swedish Cement and Concrete Institute, Stockholm, 469 pp.
- van Oss H.G. (2013) Mineral Commodity Summary. Retrieved from <http://minerals.usgs.gov>.
- Vidal T., Castel A., Francois R. (2004) Analyzing crack width to predict corrosion in reinforced concrete. *Cement and Concrete Research* 34(1):165-174.
- Walton P.L., Majumdar A.J. (1975) Cement based composites with mixtures of different types of fibres. *Composites* 6(5):209-216.
- Wang K., Jansen D.C., Shah S.P. (1997) Permeability study of cracked concrete. *Cement and Concrete Research* 27(3):381-393.
- Wang, S., Li, V.C. (2007) Engineered cementitious composites with high-volume fly ash. *ACI Materials Journal*. 104(3):233-241.
- Yazici, H. (2012) The effect of steel micro-fibers on ASR expansion and mechanical properties of mortars. *Construction and Building Materials*. 30:607-615.
- Yi, C.K., Ostertag, C.P. (2005) Mechanical approach in mitigating alkali-silica reaction. *Cement and Concrete Research*. 35(1):67-75.

Appendix A

Chemical Admixture Grid of Select Trial Mixes

Dosage		Superplasticizer (mL/100 kg binder)						
		≤ 400	660	790	880	970	1100	1170
Viscosity Modifying Admixture (mL/100 kg binder)	≤ 400	SCC,T2 T6		T3,T9				
	530					T10		
	660			T4				T1
	790	T7						
	880							T11
	1320		T26	T36	T43			T12
	2200	T33	T15,T16 T30,T34	T35,T40	T14,T27 T50	T52		T13
	2600		T18,T21 T32	T29,T48	T45			
	3300					T26		
	4400		T22		T20		T19.	

Key: red – paste segregation, orange – insufficient fiber mobility, green – non-segregating flow

All mixes to the right of the grey shading lacked sufficient paste viscosity, mixes to the left of the tan shading lacked sufficient fluidity. Please note that mix variables such as fiber and aggregate contents are not shown in this format. At later stages of development many mixes clustered in a range of VMA dosages of 1320-2600 mL/100 kg binder and superplasticizer dosages of 660-880 mL/100 kg binder with not all shown in the grid.

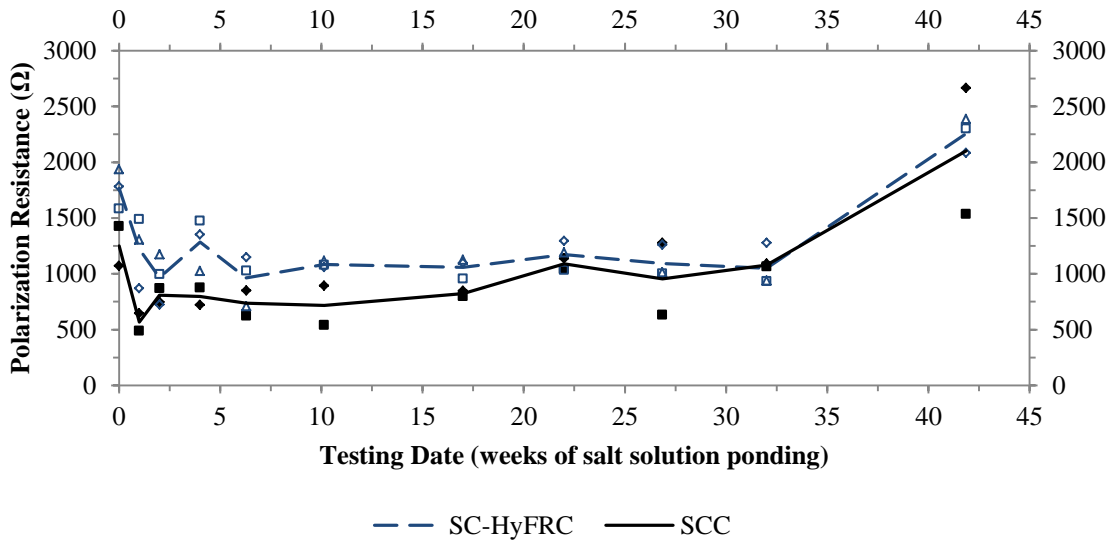
Appendix B

Corrosion Investigation Concrete Mixes (kg/m³)

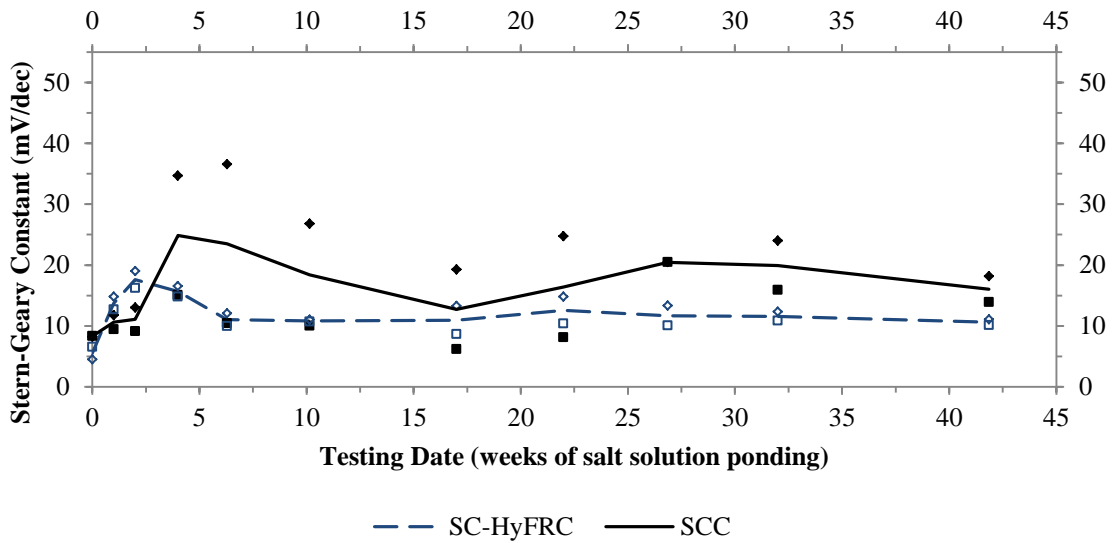
Designation	SCC ¹	SC-HyFRC ¹
Cement	397	397
Fly Ash	131	131
Water	237	237
Fine Aggregate	1006	1044
Coarse Aggregate	497	418
PVA Fiber	-	2.6
Steel Fiber	-	102
Sodium Chloride ²	26	26

¹Chemical admixtures (Superplasticizer and Viscosity Modifier) added to achieve flowability

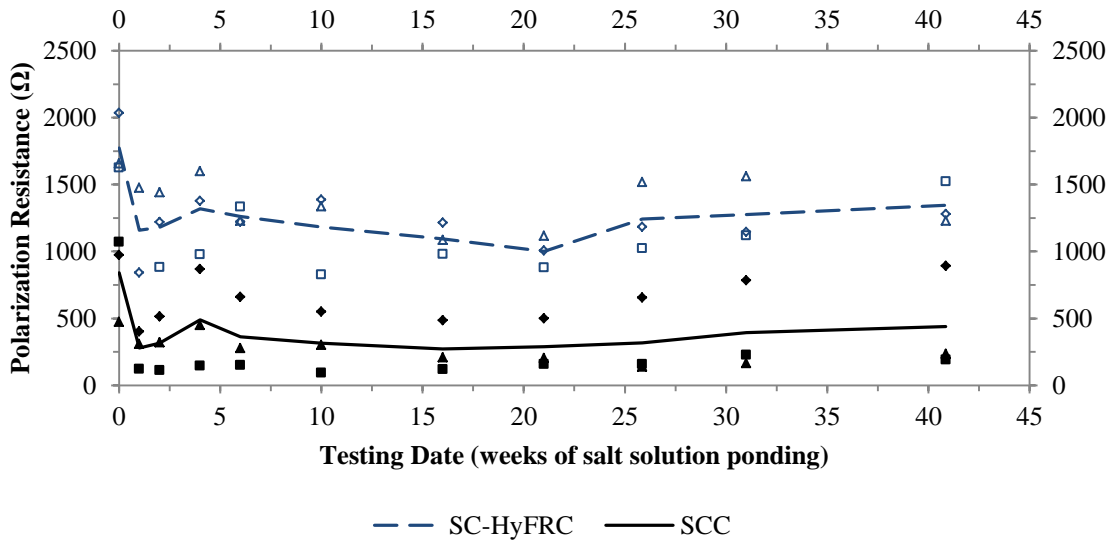
²Salt added for propagation test mixes, to reach a Cl⁻ content of 4 wt. percent cement



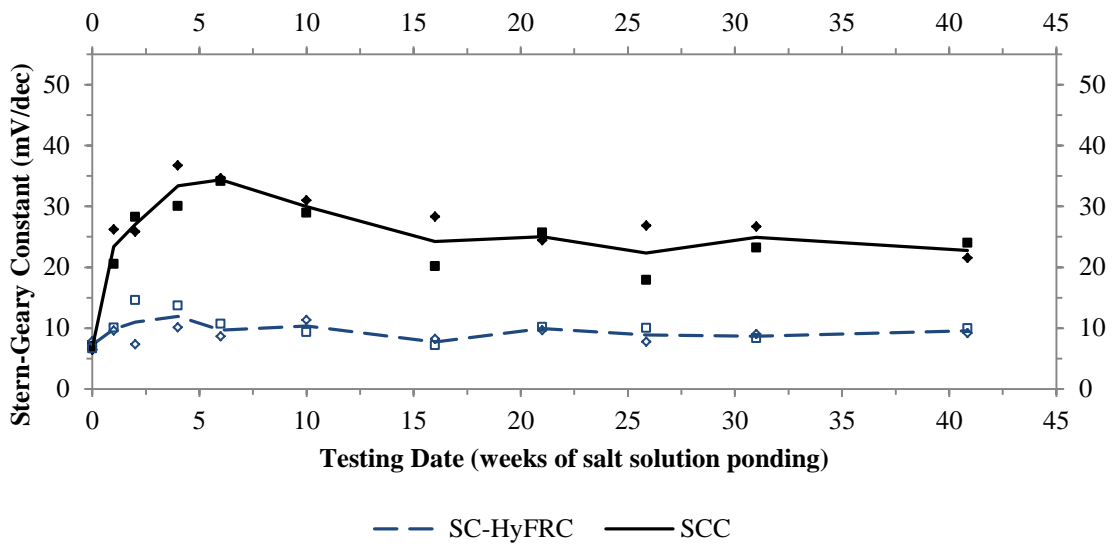
Linear Polarization Resistance Time History of Unloaded Initiation Test Beams



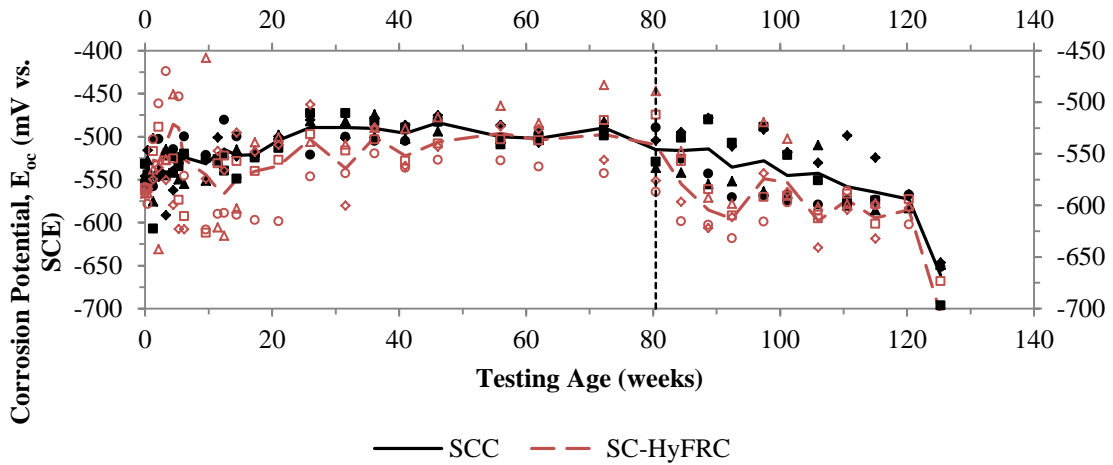
Tafel Scan Time History of Unloaded Initiation Test Beams



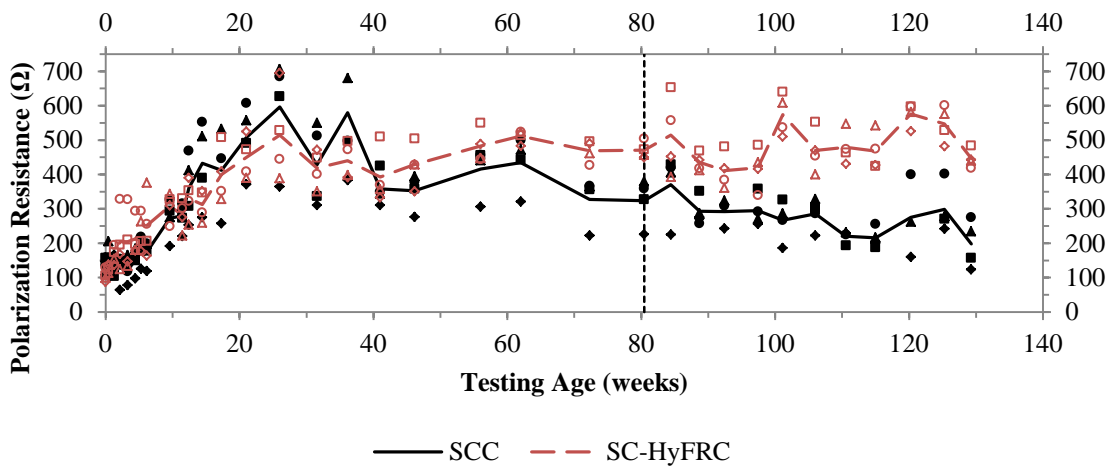
Linear Polarization Resistance Time History of Preloaded Initiation Test Beams



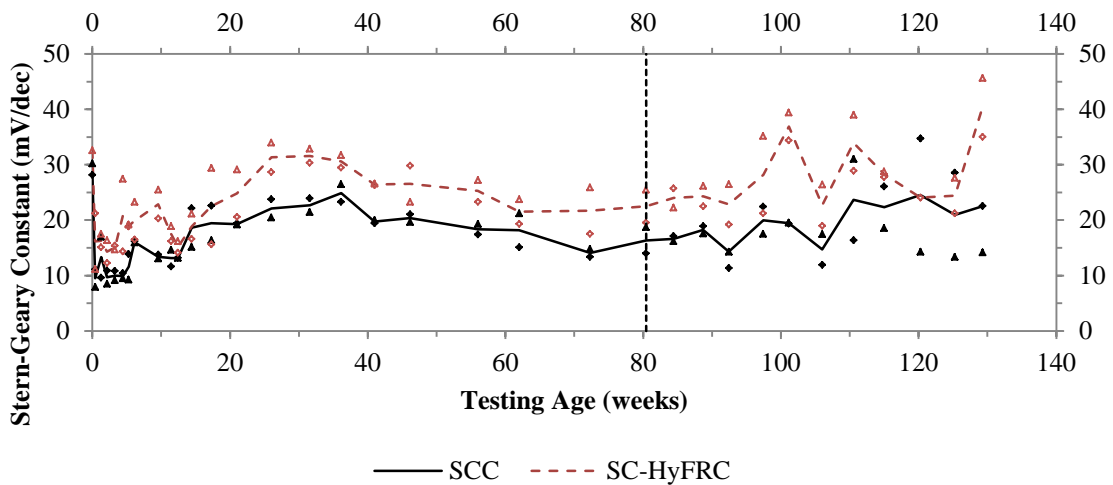
Tafel Scan Time History of Preloaded Initiation Test Beams



Corrosion Potential Time History of Conventional Propagation Test Cylinders



Linear Polarization Resistance Time History of Conventional Propagation Test Cylinders





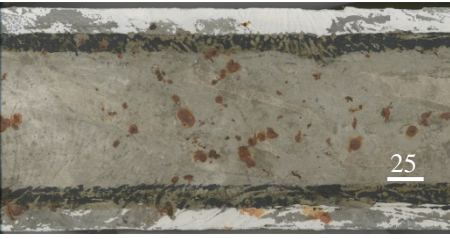
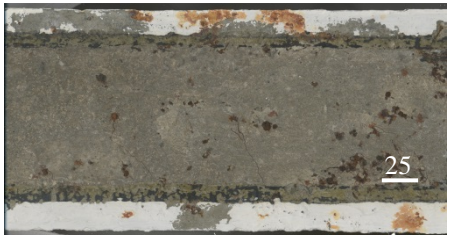


Tafel Scan Time History of Conventional Propagation Test Cylinders

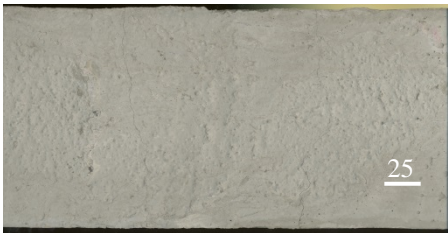

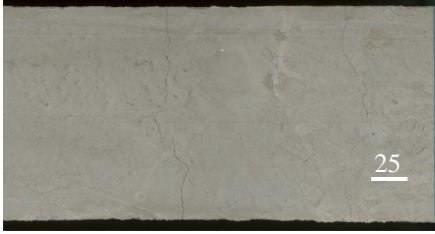

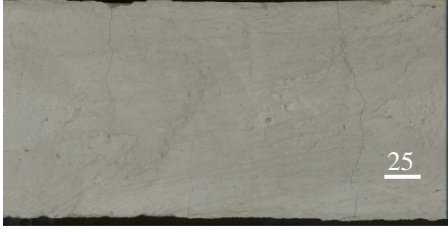

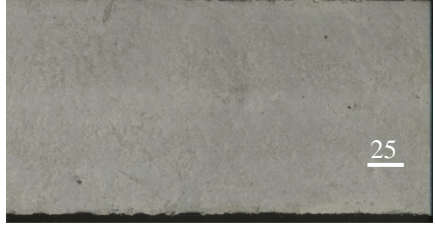
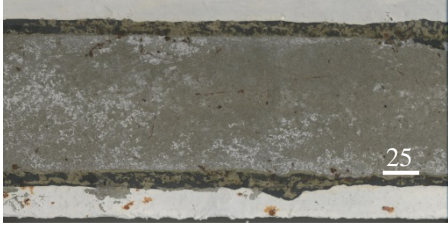




Electrochemical Measurement Comparison of Final Ponding Values with Testing
Termination Values of SCC and SC-HyFRC Beams

Beam Designation	SCC, Unloaded			SCC, Preloaded			SC-HyFRC, Unloaded			SC-HyFRC, Preloaded		
	A	Y	Z	M	Q	P	AA	AB	U	I	X	T
#3 Bar, Ponding E_{corr} (mV vs. SCE)	-150	-280	-150	-380	-430	-480	-200	-120	-420	-290	-140	-140
#3 Bar, Final E_{corr} (mV vs. SCE)	-320	-470	-500	-520	-480	-480	-470	-460	-510	-470	-450	-450
#3 Bar, Ponding i_{corr} ($\mu\text{A}/\text{cm}^2$)	0.1	1.1	-	0.2	0.7	-	0.1	0.1	-	0.1	0.1	-
#3 Bar, Final i_{corr} ($\mu\text{A}/\text{cm}^2$)	0.1	6.8	2.1	5.9	9.5	9.0	0.6	0.2	0.7	0.6	0.3	0.5
#6 Bar, Final E_{corr} (mV vs. SCE)	-90	-130	-490	-500	-410	-480	-400	-100	-40	-150	-460	-160
#6 Bar, Final i_{corr} ($\mu\text{A}/\text{cm}^2$) ¹	-	-	7.8	58.6	2.3	5.0	-	-	-	-	-	-

¹#6 Bar Final i_{corr} values only measured for samples showing evidence of splitting crack damage

At Termination of Corrosion Testing	
SCC-A	
SCC-Y	
SCC-Z	
SC-HyFRC-AA	
SC-HyFRC-AB	
SC-HyFRC-U	

Surface Scans of Ponding Faces of Unloaded SCC and SC-HyFRC Beams, mm

	Immediately Following Cyclic Loading	At Termination of Corrosion Testing
SCC-M		
SCC-P		
SCC-Q		
SC-HyFRC-I		
SC-HyFRC-T		
SC-HyFRC-X		

Surface Scans of Tensile/Ponding Faces of Preloaded SCC and SC-HyFRC Beams, mm

							
Z - #3	Z - #6	P - #3	P - #6	AB - #3	AB - #6	I - #3	I - #6

Extracted Bars from Corrosion Initiation Beam Tests

Appendix C

AMBT Mortar Mixes (kg/m³)

Designation	Cement	Fly Ash	Water	Fine Aggregate	PVA Fiber
Wright Mortar	606	-	285	1363	-
Wright, 0.2% PVA	606	-	285	1358	2.6
Wright, 1.0% PVA	606	-	285	1337	13
Wright, Fly Ash Mortar	295	295	277	1327	-
Wright, Fly Ash, 0.2% PVA	295	295	277	1321	2.6
Spratt Mortar	616	-	289	1385	-
Spratt, 1.0% PVA	616	-	289	1358	13
Vulcan Mortar	612	-	288	1377	-
Vulcan, 1.0% PVA	612	-	288	1350	13

All mortar mixes proportioned to have water:cement:aggregate weight ratios of 0.47:1.00:2.24 per ASTM C1260. Fiber inclusion is balanced by a decrease in equivalent volume of aggregate.

CPT Concrete Mixes (kg/m³)

Designation	Cement	Fly Ash	Water	Coarse Aggregate	Fine Aggregate	Steel Fiber, 60mm/30mm	PVA Fiber
Wright Reference Concrete ¹	423	-	228	814	842	-/-	-
Wright, HyFRC ¹	423	-	228	775	842	63/39	2.6
Wright Reference Concrete ²	420	-	189	1155	561	-/-	-
Wright FRC ²	420	-	189	1115	561	63/39	2.6
Spratt Reference Concrete ²	420	-	189	1088	641	-/-	-
Spratt FRC ²	420	-	189	1047	641	63/39	2.6
Wright, SCC, 0% Fly Ash ¹	548	-	246	500	1003	-/-	-
Wright, SCC, 25% Fly Ash ¹	397	131	237	497	1006	-/-	-
Wright, SC-HyFRC, 25% Fly Ash ¹	397	131	237	418	1044	-/103	2.6

All mixes are supplemented with NaOH to bring alkali loading to 1.25 weight percent of cement content

¹Cement, coarse and fine aggregate contents as required for desired fiber reinforced concrete workability level

²Cement, coarse and fine aggregate contents as specified by ASTM C1293